

DISSERTATION

# Exceptional points in lasers

Ausgeführt zum Zwecke der Erlangung des akademischen Grades

**Doktor der technischen Wissenschaften**

eingereicht von

**Dipl.-Ing. Matthias Liertzer**

Matrikelnummer 0425333

Bäuerlegasse 9/37, 1030 Wien

an der

Fakultät für Physik der Technischen Universität Wien

Betreuung:

Univ. Prof. Dipl.-Ing. Dr.techn. Stefan Rotter,

Institut für theoretische Physik – E136

Diese Dissertation haben begutachtet:

---

(Prof. Dr. Stefan Rotter)

---

(Prof. Dr. Jan Wiersig)

Wien, 15.10.2015

---

(Dipl.-Ing. Matthias Liertzer)



TECHNISCHE  
UNIVERSITÄT  
WIEN  
Vienna University of Technology

DISSERTATION

# Exceptional points in lasers

submitted in partial fulfillment of the requirements for the degree of

**Doktor der technischen Wissenschaften**

by

**Dipl.-Ing. Matthias Liertzer**

Registration Number 0425333  
Bäuerlegasse 9/37, 1030 Wien

to the Faculty of Physics  
at the Vienna University of Technology

Advisor:  
Univ. Prof. Dipl.-Ing. Dr.techn. Stefan Rotter  
Institute of Theoretical Physics – E136

The dissertation has been reviewed by:

---

(Prof. Dr. Stefan Rotter)

---

(Prof. Dr. Jan Wiersig)

Wien, 15.10.2015

---

(Dipl.-Ing. Matthias Liertzer)

# Erklärung zur Verfassung der Arbeit

Dipl.-Ing. Matthias Liertzer  
Bäuerlegasse 9/37, 1030 Wien

Hiermit erkläre ich, dass ich diese Arbeit selbständig verfasst habe, dass ich die verwendeten Quellen und Hilfsmittel vollständig angegeben habe und dass ich die Stellen der Arbeit - einschließlich Tabellen, Karten und Abbildungen -, die anderen Werken oder dem Internet im Wortlaut oder dem Sinn nach entnommen sind, auf jeden Fall unter Angabe der Quelle als Entlehnung kenntlich gemacht habe.

---

(Ort, Datum)

---

(Unterschrift Dipl.-Ing. Matthias  
Liertzer)

# Kurzfassung

Aufgrund der Fortschritte auf dem Gebiet der Miniaturisierung von optischen Elementen, ist es möglich Laser mit Abmessungen im Bereich hunderter Nanometer bis zu mehreren Mikrometern herzustellen, welche kohärentes Licht unterschiedlichster Wellenlänge emittieren können. Diese werden als Mikrolaser bezeichnet. Die Laserresonatoren sind nicht beschränkt auf einfache Geometrien wie zum Beispiel die eines Fabry-Perot Resonators, sondern können komplizierte Formen annehmen. Mittlerweile ist nicht nur die Form der Laserkavitäten ein wichtiges Element für das Design der Lasereigenschaften: Auch der Einsatz von absorbierenden Materialien innerhalb der Kavität kann neben den verstärkenden Materialien dazu verwendet werden um ein spezielles Laserverhalten zu induzieren.

Wie wir im Rahmen dieser Dissertation zeigen, können solche nicht-Hermiteschen Systeme sogenannte Ausnahmepunkte ("Exceptional Points") aufweisen. Exceptional Points können in Mikrolasern mit einem hier vorgestellten Pumpschema induziert werden und bewirken, dass der Laser ein ungewöhnliches und kontraintuitives Verhalten aufweist.

Um sowohl Mikrolaser mit kompliziert geformten Resonatoren, als auch Resonatoren mit verstärkenden, beziehungsweise absorbierenden Materialien simulieren zu können, modellieren wir diese Systeme mit der "Steady-state ab initio laser" Theorie (SALT), welche die zeitunabhängigen stationären Lösungen der Maxwell-Bloch Gleichungen beschreibt. Hierfür haben wir einen gut skalierbaren und effizienten Löser auf Grundlage der Finiten Elemente Methode entwickelt, um die nichtlinearen und nicht-Hermiteschen partiellen Diffe-

rentialgleichungen der SALT zu lösen. Weiters haben wir den Anwendungsbereich der SALT auf Resonatoren erweitert welche entartete und leicht nicht-entartete Eigenmoden aufweisen. Diese Systeme konnte die bisherige Theorie bis dato nicht eindeutig beschreiben.

Wir wenden diesen neuartigen Löser auf ein Lasersystem mit Exceptional Points an, um deren Auswirkungen auf das Laserverhalten zu verstehen. Das Hauptergebnis dieser Arbeit ist ein kontraintuitiver Anstieg der Leistung des Lasers trotz einer Erhöhung der Absorption im Lasersystem nach Passieren des Exceptional Points. Weiters zeigen wir, dass bei Mikrolasern die bereits bekannte Linienverbreiterung in der Nähe des Exceptional Points nur eingeschränkt messbar sein kann, da das System für Halbleiterlaser instabil wird.

Nachdem ursprünglich veröffentlichten theoretischen Ergebnissen zur Behandlung von Exceptional Points in Lasern, haben wir mit zwei experimentellen Gruppen zusammengearbeitet, die die theoretischen Ergebnisse experimentell verifiziert haben. Sowohl am Institut für Photonik der TU Wien, als auch an der Washington University in St. Louis, wurden unsere theoretischen Vorhersagen mittlerweile in zwei völlig unabhängigen Experimenten nachgewiesen. Beide dieser experimentellen Realisierungen werden kurz beschrieben und mit den theoretischen Beschreibungen verglichen.

# Abstract

Recent advances in fabrication techniques have given rise to a great variety of novel and very small laser systems ranging from nano-scale devices to microlasers operating in different wavelength regimes. The cavities of these lasers are not limited to the standard Fabry-Perot type, but can be fabricated in complex shapes. In addition to these complex geometries a further design element has recently been brought forward: The concept of deliberately using both gain and loss in a laser system. As we will show in this thesis, such non-Hermitian systems can easily be tuned to exhibit so-called exceptional points at which the system generally features very uncommon and counter-intuitive lasing behavior. In particular, we present a pump-protocol that allows to conveniently observe such an atypical phenomenon in a so-called “photonic molecule laser”.

In order to simulate both the complicated geometries of these microlasers as well as their gain/loss distribution, we model these systems using the steady-state ab-initio laser theory (SALT), which is a steady-state approach to solve the Maxwell-Bloch equations. For this we have developed a new scalable and efficient solver based on the finite element technique to tackle these nonlinear non-Hermitian partial differential equations. Furthermore we have extended SALT to broaden the range of its applicability to resonators with degenerate or slightly non-degenerate modes, for which a rigorous treatment so far has been missing.

We apply this solver to investigate the influence of exceptional points on the characteristics of the laser output. The key result of this work is a counter-intuitive loss-induced enhancement of the laser output power when passing

an exceptional point. Close to the exceptional point we show that the laser linewidth is enhanced by orders of magnitude and the laser becomes unstable.

After the original theoretical proposal for studying exceptional points in lasers we provided theoretical support to two experimental groups at the Photonics institute at TU Wien, as well as at the Washington University in St. Louis, which resulted in two independent experimental verifications of our theoretical predictions. Both experimental realizations are reviewed and compared to the theoretical descriptions.

# Contents

<b>1</b>	<b>Introduction</b>	<b>3</b>
1.1	Structure of the Dissertation . . . . .	5
<b>2</b>	<b>Exceptional Points</b>	<b>6</b>
2.1	Mathematical definition . . . . .	6
2.2	Physical interpretation . . . . .	8
2.3	Coupled mode theory for optical resonators . . . . .	9
2.3.1	Maxwell's equation . . . . .	11
<b>3</b>	<b>Steady-state ab-initio laser theory</b>	<b>15</b>
3.1	Maxwell-Bloch equations . . . . .	15
3.1.1	SALT units . . . . .	16
3.2	Ansatz and approximations . . . . .	17
3.3	SALT equations . . . . .	19
3.4	Modal output power . . . . .	20
3.5	Solution strategy . . . . .	21
3.5.1	Finding the number of active laser modes $N$ . . . . .	21
3.5.2	Solving the SALT equation . . . . .	23
3.5.3	Example: slab cavity laser . . . . .	24
3.6	Numerical implementation . . . . .	26
3.6.1	Review: constant-flux state approach . . . . .	26
3.6.2	Perfectly matched layer . . . . .	28
3.7	Finite element discretization of SALT . . . . .	29
3.7.1	Solving the SALT equation (3.15) . . . . .	30



3.7.2	Solving the nonlinear eigenvalue problem of Eq. (3.19) . . .	31
<b>4</b>	<b>Study of exceptional points in coupled cavity lasers with SALT</b>	<b>34</b>
4.1	Two coupled cavities in 1D . . . . .	34
4.2	Photonic molecule . . . . .	41
4.3	Distributed feedback laser . . . . .	43
4.4	Open questions . . . . .	46
<b>5</b>	<b>Linear stability analysis in SALT and its application for near-degenerate modes</b>	<b>48</b>
5.1	Linear stability . . . . .	49
5.2	SALT for degenerate and near-degenerate modes . . . . .	53
5.3	Discussion . . . . .	60
5.4	Application: Photonic molecule laser . . . . .	61
5.5	SALT beyond the stationary inversion approximation . . . . .	64
<b>6</b>	<b>Exceptional points above the laser threshold</b>	<b>67</b>
6.1	Linewidth calculation in SALT . . . . .	68
6.2	Stability close to an exceptional point . . . . .	70
6.3	Laser linewidth close to an EP . . . . .	73
<b>7</b>	<b>EPs in transmission experiments and chirality</b>	<b>74</b>
7.1	EPs in coupled microdisks . . . . .	75
7.1.1	TCMT model . . . . .	76
7.1.2	Numerics . . . . .	77
7.1.3	Discussion . . . . .	78
7.2	Chirality . . . . .	79
7.2.1	TCMT model . . . . .	81
7.2.2	Numerical results . . . . .	84
7.2.3	Discussion . . . . .	86
<b>8</b>	<b>Experimental observations of exceptional points in a laser</b>	<b>89</b>
8.1	EP in coupled THz quantum cascade lasers . . . . .	90

<i>CONTENTS</i>	viii
8.2 EP in silica whispering-gallery-mode resonators . . . . .	94
<b>9 Conclusion and Outlook</b>	<b>97</b>
<b>Bibliography</b>	<b>99</b>

# Acknowledgements

This thesis would not have been possible without the support and help of many people. First and foremost I would like to thank my PhD supervisor Stefan Rotter for entrusting me to being the first PhD student in his group. Despite his numerous tasks of building up the group, teaching students the foundations of quantum mechanics, attracting funding and starting a family, he was always available when I needed advice. His enthusiasm for physics and his constant quest for presenting complex physical phenomena as straightforwardly as possible have been truly inspiring and hopefully shaped my own way of presenting my research.

I would like to thank Dmitry Krimer and Stephan Burkhardt both for being great office colleagues and for their collaboration on dealing with degenerate and near-degenerate modes in SALT. Without their work on the linear stability analysis this project would not have been possible. Similarly, I thank Sofie Esterhazy for our successful collaboration on developing a more scalable approach to solving the SALT equations.

I'm indebted to our experimental collaborators who took on the challenge to verify our theoretical predictions of the appearance of exceptional points in lasers. Martin Brandstetter and Christoph Deutsch performed the corresponding experiments at TU Wien in the group of Karl Unterrainer and did a remarkable job of realizing the reversal of the pump dependence in quantum cascade lasers. I want to thank Bo Peng and Sahin Özdemir as well, who independently verified the EP in Silica resonators in the group of Lan Yang at the Washington University in St. Louis.

Special thanks also go to Hakan Türeci who gave me the opportunity to be a visiting student in his research group during the summer of 2014.

Last but not least I want to thank my family, my friends and especially my girl friend Stefanie Wolf. I wouldn't have made it without you.

## Introduction

Early laser theory typically treated laser resonators by assuming a closed cavity [1]. This approximation has the advantage that the Maxwell-operator is Hermitian and hence the eigenmodes of a resonator are orthogonal to each other. However, such a simple treatment of the boundary conditions does not correctly capture the openness of the laser and its concomitant non-Hermitian nature. The most dramatic effect of such non-Hermitian contributions arises at so-called exceptional points (EPs) also known as “non-Hermitian degeneracies”. In contrast to a degeneracy point of a closed Hermitian systems where two or more eigenfrequencies become identical and the degenerate eigenmodes can always be constructed to be orthogonal to each other, at an EP not only two or more eigenfrequencies become the same, but the corresponding eigenmodes coalesce as well. As a consequence such non-Hermitian systems can feature non-trivial behavior in the vicinity of an EP [2]. This has recently lead to a number of experiments and theoretical studies on the topic of EPs [3–14]. In particular, research on parity-time (PT) symmetric systems for which the EPs occur at real eigenfrequencies have been a driving factor behind recent progress [15]. In practical realizations of such PT-symmetric systems, coupled resonators or waveguides with balanced gain and loss were used, where the EP can be induced by tuning the values of the coupling and gain/loss-strength, respectively [16]. Here,

it was shown that when steering a system through an EP by parametric variation of one of these parameters the system can radically change its behavior. The central topic of this thesis is to investigate, whether such a scenario can also be observed in lasers, how it can be conveniently induced and in which way it manifests itself in the experiment.

In order to correctly model EPs in lasers we need to correctly model the non-Hermiticity of the problem which is both due to the amplification of light within the system as well as due to the openness of the system. For this we use semiclassical laser theory, where the electric field of the system is treated classically and the interaction of the field with an amplifying medium described as an ensemble of two-level atoms is treated quantum mechanically. The fundamental equations of this theory are given by the time-dependent Maxwell-Bloch equations which describe the dynamics of the electric field, the polarization and the inversion density of the laser. Since we are primarily interested in the steady-state operation of a laser we use the steady-state ab-initio laser theory (SALT) [17–19]. SALT provides an efficient method for determining the time-independent solutions of the Maxwell-Bloch equations.

Using this formalism we study in particular the appearance of exceptional points in coupled laser systems. For this we extend SALT by developing a more efficient solution method which is no longer based on the concept of constant flux states [17, 18], but solves the nonlinear set of partial differential equations directly on top of a finite element framework. Furthermore, we extend SALT such that it can be applied to resonators featuring degenerate or near-degenerate modes. We study the appearance of exceptional points both below as well as above the laser threshold. Whereas in the first case the system naturally does not lase at the EP, in the latter case, we determine the stability and the linewidth of the laser at the EP.

## 1.1 Structure of the Dissertation

In chapter 2 we are going to introduce the concept of exceptional points with a simple  $2 \times 2$  toy model and show how this directly corresponds to a two-mode approximation of coupled-mode theory with two coupled cavities. In order to be able to rigorously describe the steady-state lasing of such a coupled system we introduce the steady-state ab-initio laser theory (SALT) in chapter 3. There, we give a short overview on its derivation and involved approximations to the case of multi-mode lasing. Furthermore, we introduce a novel method for efficiently solving SALT without relying on a basis expansion in terms of constant flux states. In chapter 4, we apply SALT to the case of an exceptional point occurring below the laser threshold. We consider both a 1D toy model, as well as a realistic 2D setup based on coupled microdisk lasers. One deficiency of SALT is that the two active near-degenerate modes, which occur in this setup could originally not be described in the context of SALT. Hence, in chapter 5 we show how SALT can be extended to cover this case by noting that nonlinear self-interactions of the modes lead to the formation of hybridized modes. For proving the stability of these solutions we introduce a linear stability analysis for SALT. As a last step we apply this new formalism to the near-degenerate modes of the coupled microdisk lasers of the previous chapter. In chapter 6 we investigate steady-state lasing in the vicinity of exceptional points above the laser threshold and its influence on both the stability as well as on the linewidth of the laser. In chapter 7 we discuss theoretically how exceptional points can be studied in whispering-gallery-mode resonators by coupling fiber-tapers to the system. In chapter 8 we review two experimental verifications of the predicted EP-induced laser shutdown and revival.

# Exceptional Points

## 2.1 Mathematical definition

Exceptional points are specific points in the parameter space of a non-Hermitian matrix or, in general, an operator where not only two or more of its eigenvalues become identical in a branch-cut singularity, but also the corresponding eigenvectors or eigenfunctions coalesce [20–22]. This is in contrast to a degeneracy point of a Hermitian matrix at which only the degenerate eigenvalues become the same, but the corresponding eigenvectors may still be chosen such as to remain orthogonal to each other.

In more mathematical terms, at an EP the geometric multiplicity is no longer equal to the algebraic multiplicity and as a consequence the matrix is no longer diagonalizable. However, it can be brought into a Jordan Normal form. The matrix is said to become *defective* and the eigenvalue is a defective eigenvalue [23,24].

The occurrence of an EP of a parametrized matrix can already be demonstrated with a simple 2x2 matrix, such as

$$H = \begin{pmatrix} \omega_1 - i\kappa_1 & \gamma \\ \gamma^* & \omega_2 - i\kappa_2 \end{pmatrix}, \quad (2.1)$$



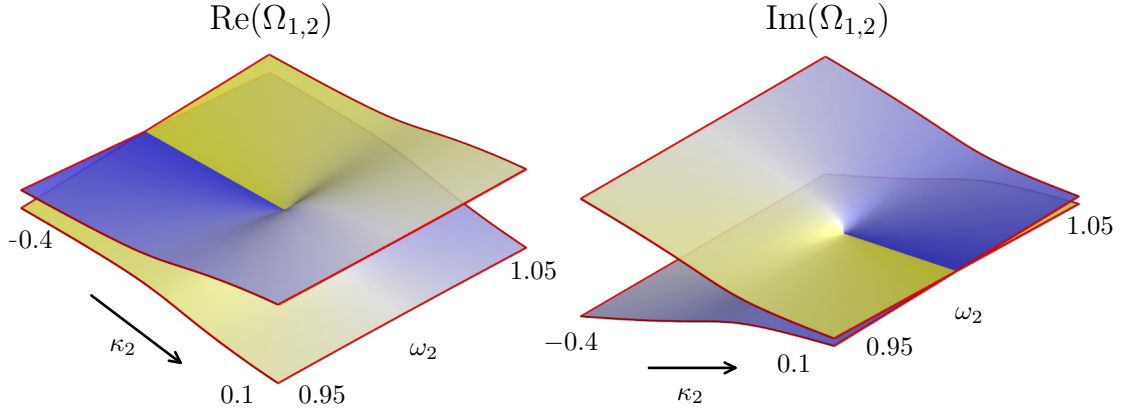


**Figure 2.1:** Dependence of the complex eigenvalues  $\Omega_{1,2}$  on the parameters  $\omega_2$  and  $\kappa_2$ . The real and imaginary part of  $\Omega_{1,2}$  are shown in the left and right panel respectively. The parameters for  $\omega_1$ ,  $\kappa_1$ , and  $\gamma$  are given by 1.0,  $-0.1$ , and  $0.15$ , respectively. The EP is reached when  $\omega_2 = 1.0$  and  $\kappa_2 = 0.2$ .

which has the following eigenvalues

$$\Omega_{1,2} = \frac{1}{2} (\omega_1 - i\kappa_1 + \omega_2 - i\kappa_2 \pm D) \quad (2.2)$$

with the discriminant

$$D = \sqrt{(\omega_1 - i\kappa_1 - (\omega_2 - i\kappa_2))^2 + 4|\gamma|^2}. \quad (2.3)$$

The (non-normalized) eigenvectors are given by

$$\mathbf{u}_{1,2} = \begin{pmatrix} \omega_1 - i\kappa_1 - (\omega_2 - i\kappa_2) \pm D \\ 2\gamma^* \end{pmatrix}. \quad (2.4)$$

The EP occurs when the discriminant (2.3) vanishes, which, for example, is the case when  $\omega_1 = \omega_2$  and  $\kappa_1 - \kappa_2 = 2|\gamma|$ . At this point the eigenvectors (2.4) become collinear and the eigenspace of  $H$  collapses. In general a variation of at least two parameters of the matrix is necessary in order to reach an EP [25]. In Fig. 2.1, the real and imaginary part of the eigenvalue sheets,  $\Omega_{1,2}$ , are shown under variation of the parameters  $\omega_2$  and  $\kappa_2$  with the EP located directly at the center of the two plots. Note, the strong dependence of  $\Omega_{1,2}$  on the parameters

$\omega_2$  and  $\kappa_2$ . In fact the derivative of  $\Omega_{1,2}$  with respect to any of the parameters becomes infinite at the EP.

The eigenvalue sheets around an EP display the typical structure of two intersecting Riemann surfaces that are connected to each other via the EP. As a consequence when tracking an eigenstate around the EP one does not come back to the original eigenstate that one started from, but instead to the second eigenstate and the eigenstates interchange. When going around the EP twice, the original eigenstate is recovered albeit with an additional phase of  $\pi$ . Only by going around the EP four times the original eigenstate is restored [26,27]. In a truly time-dependent encircling of the EP additional corrections to this picture appear [28–31].

## 2.2 Physical interpretation

In general, one can interpret the toy Hamiltonian of Eq. (2.1) as the interaction between two coupled resonator modes. Here,  $\omega_1$  and  $\omega_2$  represent the eigenfrequencies of these modes, which are coupled to each other with a complex coupling strength of  $\gamma$  and which decay or grow, depending on the sign, at a rate of  $\kappa_1$  or  $\kappa_2$ , respectively.

The physical manifestation of the presence of EPs has been studied in a multitude of systems over the past years [2]. The first experimental studies that explored EPs were performed in microwave cavities [27,32,33], where EPs have not only been observed, but also their properties with respect to encircling the EP have been studied [26]. EPs have been investigated in coupled electronic systems [34–36], chaotic optical microcavities [11], in an open composite quantum systems of a high-Q cavity and a single atom [37]. Furthermore, EPs have been suggested for highly accurate optical-sensing applications [9].

As discussed in the introduction, an interesting class of systems which prominently features EPs and which has given rise to a significant amount of research in recent years is the class of parity-time ( $\mathcal{PT}$ ) symmetric systems [16,38]. Here, the EP is associated with a  $\mathcal{PT}$ -symmetry breaking transition. This can

already be easily demonstrated with the toy Hamiltonian of Eq. (2.1) where  $\mathcal{PT}$ -symmetry implies that  $H$  should be invariant under exchange of the two modes and complex conjugation. This symmetry condition is realized for  $\omega_1 = \omega_2 = \omega$ , and  $\kappa_1 = -\kappa_2 = \kappa$ . For  $\kappa < |\gamma|$ , the eigenstates are  $\mathcal{PT}$ -symmetric. The corresponding eigenvalues of the system are real. For  $\kappa > |\gamma|$ , the eigenstates are no longer  $\mathcal{PT}$ -symmetric and the eigenvalues become complex. The EP at  $\kappa = |\gamma|$ , at which both eigenstates coalesce thus constitutes the symmetry breaking point of the system.

Experimentally the  $\mathcal{PT}$ -symmetry breaking transition at an EP has first been demonstrated in optics [16]. Here, for a system of coupled wave guides the  $\mathcal{PT}$ -symmetry condition needs to be fulfilled by the index of refraction whose real (imaginary) part needs to feature an even (odd) symmetry with respect to the symmetry axis [39]. Since then the concept of  $\mathcal{PT}$ -symmetry in optics has been widely extended: Leaving the realm of strict mapping to the Schrödinger equation,  $\mathcal{PT}$ -symmetric laser absorbers have been suggested which act both as a laser and as a coherent perfect absorber at the lasing threshold [40, 41].  $\mathcal{PT}$ -symmetry has since then been investigated in (passive) whispering gallery microcavities [42, 43] and as a source of single mode lasing in active  $\mathcal{PT}$ -symmetric microring lasers [44, 45]. However, already one of the first works on the subject showed that strict  $\mathcal{PT}$ -symmetry is not necessary for observing an EP with an associated symmetry breaking [46].

## 2.3 Coupled mode theory for optical resonators

In this thesis we will investigate the influence of EPs on optical resonators without necessarily enforcing  $\mathcal{PT}$ -symmetry. In this context we can already interpret the  $2 \times 2$  matrix toy model of Eq. (2.1) as a coupled mode theory description of two coupled one-dimensional resonators as shown in Fig. 2.3. Here,  $\omega_{1,2}$  correspond to the resonance frequencies of two individual resonators and  $2\kappa_{1,2}$  to the corresponding decay rates. The parameter  $\gamma$  defines the coupling strength between the two resonators. The coupling leads to the formation of two super-

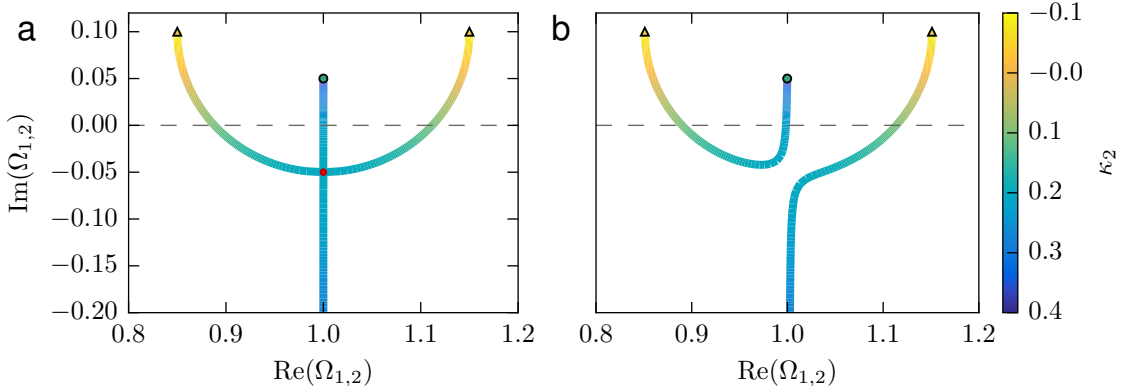


**Figure 2.2:** Movement of the complex eigenfrequencies  $\Omega_{1,2}$  of matrix  $H$  in dependence of a variation of the decay/growth rate  $\kappa_2$  of resonator 2. The rest of the parameters are the same as given in Fig. 2.1. (a) Here,  $\omega_1 = \omega_2 = 1$  and the EP is reached exactly for  $\kappa_2 = -0.2$ . (b) Here, we set  $\omega_2 = 1.02 \neq \omega_1$  and no longer reach the EP exactly, however, the overall behavior of the system remains the same.

modes of the system with complex frequencies  $\Omega_{1,2}$ .

As one typically does not have full access to both easily control the resonance frequency as well as the decay rate of a single resonator, we first study on how only a variation of the decay rate  $\kappa_2$  influences the complex frequencies  $\Omega_{1,2}$ . In case that both resonators feature the same individual frequency  $\omega_1 = \omega_2$  we observe that the EP can still be reached exactly (see Fig. 2.2a). At this point it is suitable to discuss the exact choice of parameters we have made for this calculation: The first resonator is fixed with a “growth rate” of  $\kappa_2 = -0.1$ , i.e., the mode of the isolated resonator in this linear model would grow exponentially. In reality this exponential growth would saturate through spatial hole burning and the system would lase at a real frequency close to  $\omega_1$  (see chapter 3). The laser threshold of the system is given by  $\text{Im}(\Omega_{1,2}) = 0$  and is displayed in Figs. 2.2a as a black dashed line. When the second resonator with a strongly decaying mode of  $\kappa_2 = 0.4$  is coupled to the first resonator, the system keeps lasing as the resonators are only weakly coupled (the green dot in Fig. 2.2a is above the real axis). When decreasing the decay rate  $\kappa_2$  of the second resonator the resonance  $\Omega_1$  is pulled below the real axis and the system stops lasing as the

coupling between the two resonators is increased. At  $\kappa_2 = 0.2$  an EP is reached where both supermode frequencies  $\Omega_{1,2}$  are the same, indicated by a red dot in Fig. 2.2. When further decreasing the loss  $\kappa_2$ , the real parts of the complex frequencies  $\Omega_{1,2}$  split and their decay rates given by  $\text{Im}(\Omega_{1,2})$  become the same. At  $\kappa_2 = 0.1$  the system reaches the laser threshold and the system starts lasing at the corresponding frequencies  $\Omega_{1,2}$ .

Note, that although the overall loss in the system as determined by  $\kappa_{1,2}$  was continuously decreased, at first the laser shut off and only with a further strong decrease of the loss started lasing again. This is in contrast to common sense which suggests that a decrease of loss or additional gain should lead to an increase of the laser power output. This counterintuitive phenomenon does not rely on the exact encounter of an EP, but is also present when the EP is not reached exactly: In Fig. 2.2b it is assumed that the two individual resonances of the individual resonators are not exactly the same but feature a slight resonance frequency mismatch, i.e. ,  $\omega_2 = 1.02 \neq \omega_1$ . Although the EP is not reached exactly, the overall behavior of the system remains the same, i.e. , with a decrease of the overall loss in the system the coupled modes stop lasing and only recover when the gain given by  $-\kappa_1$  compensates the losses of  $\kappa_2$ . Note, that the death of the laser and later recovery is typical for an EP in the system. Interestingly, loss-induced lasing has already been demonstrated for DFB lasers, which were engineered such that the loss was only added at the nodes of an existing mode in the system which effectively promotes this single mode over all other modes of the system [47,48]. These earlier studies did, however, not make a connection to EPs as we will show in Sec. 4.3.

### 2.3.1 Maxwell's equation

The coupled mode theory as described in the previous section is typically a good model for understanding the effect of an EP on the complex eigenfrequencies of the coupled resonator system. However, in order to apply coupled mode theory to an actual setup of coupled cavities one first needs to obtain the single cavity frequencies  $\omega_1 + i\kappa_1$  and the coupling rate  $\gamma$ . For this we solve the



**Figure 2.3:** Two coupled 1D resonators.

harmonic Maxwell equation for the eigenmodes,  $\mathbf{E}_\mu(\mathbf{x})$ , of the electric field and corresponding (complex) eigenfrequencies,  $\bar{\omega}_\mu$ ,

$$(\vec{\nabla} \times \vec{\nabla} \times - \epsilon_c \bar{\omega}_\mu^2) \vec{E}_\mu(\mathbf{x}) = 0. \quad (2.5)$$

Note, that we set  $c = 1$  in this thesis such that the wave number  $k_\mu$  and the eigenfrequency  $\omega_\mu$  can be used interchangeably. Furthermore, complex frequencies,  $\bar{\omega}_\mu$ , will be denoted with overbars throughout this thesis. In one dimension and for TM-polarized fields in two dimensions Eq. (2.5) reduces to the scalar Helmholtz equation

$$(\nabla^2 + \epsilon_c \bar{\omega}_\mu^2) E_\mu(\mathbf{x}) = 0. \quad (2.6)$$

We solve Eq. (2.6) for the eigenfrequencies  $\bar{\omega}_\mu$  with outgoing boundary conditions (Sommerfeld radiation condition)

$$\lim_{r \rightarrow \infty} r^{\frac{d-1}{2}} \left( \frac{\partial E_\mu}{\partial r} - i\omega_\mu E_\mu \right) = 0, \quad (2.7)$$

where  $d$  is the spatial dimension. The vectorial variant of these boundary conditions, which need to be applied for Eq. (2.5) is the Silver-Müller radiation condition [49],

$$\lim_{r \rightarrow \infty} r [(\nabla \times E_\mu) \times \hat{\mathbf{x}} - i\omega_\mu E_\mu] = 0, \quad (2.8)$$

where  $\hat{\mathbf{x}} = \mathbf{x}/|\mathbf{x}|$ .

We verify that the Helmholtz Eq. (2.6) for a one-dimensional toy system of two coupled cavities as displayed in Fig. 2.3 indeed shows the same behavior as demonstrated by the results from coupled mode theory. Since the Maxwell equations are scale-invariant we provide all dimensions of the system in terms of a length scale  $\tilde{L}$ . Correspondingly, the frequencies will be given in dimensionless units in terms of  $1/\tilde{L}$ , since we set  $c = 1$ . The toy model, which we are

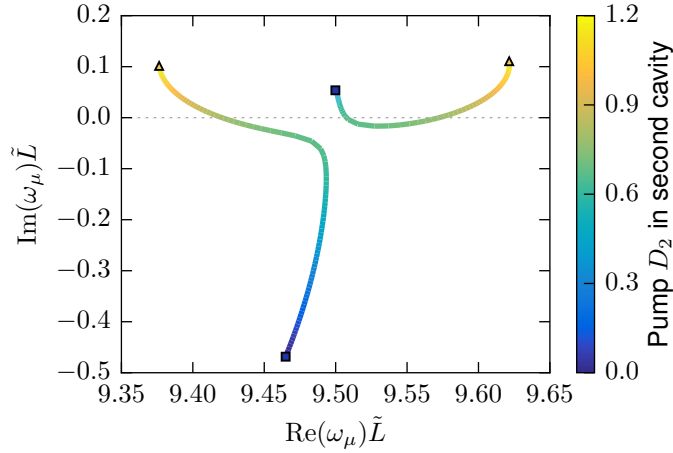


**Figure 2.4:** Dependence of the two resonances of frequency  $\omega_\mu$  near  $\omega_a = 10$  on the pump applied to the two-coupled cavity system of Fig. 2.3 with dimension as described in the text. The shutdown effect as demonstrated with the results from coupled mode theory (see Fig. 2.2) is present.

also going to use in the following chapters when applying semiclassical laser theory, consists of two one-dimensional cavities of length  $\tilde{L}$  and an index of refraction of  $n = 3.0 + 0.13i$  of the passive (unpumped) system surrounded by air, where  $n = 1$ . A gap of  $0.1\tilde{L}$  separates the two cavities. Here, we simply model the pump via a change of the imaginary part of the permittivity

$$\varepsilon(x) = n^2(x) + i(D_1 + D_2), \quad (2.9)$$

where  $D_1$ , and  $D_2$  correspond to the pump applied to cavity 1 and 2, respectively. Similar to Fig. 2.2 we assume that cavity 1 is pumped such that the isolated cavity would be above threshold and choose  $D_1 = 1.2$ . The pump in the second cavity,  $D_2$  is scanned from 0 to 1.2. In Fig. 2.4, we demonstrate that the EP induced shutdown of the laser is achieved in a pump range of  $D_2$  from 0.67 to 0.792.

Note, that although these initial results already provide a good understanding of the laser shutdown effect caused by the EP, the simple models presented here are still only very rough models of a laser. For example, they feature exponentially “growing” resonances with complex frequencies with an imaginary

part larger than 0 and they do not capture the full nonlinearity of the laser. Hence, they cannot correctly predict the output power of a laser. Furthermore, a flat gain curve is assumed and no modal interactions are taken into account. To remedy these limitations we will introduce the steady-state ab-initio laser theory in the next chapter.



## Steady-state ab-initio laser theory

In this chapter we are going to review the semiclassical laser theory in order to rigorously simulate the loss-induced suppression and revival of lasing due to the occurrence of an EP. For this we first introduce the Maxwell-Bloch equations as the basis for formulating the steady-state ab-initio laser theory (SALT). Next, we give a short outline on how to derive SALT and go into detail on the required assumptions and approximations needed for describing steady-state multi-mode lasing.

In the second part we will present an efficient strategy for solving the nonlinear SALT equations. For this we have developed a novel and efficient numerical scheme for solving the resulting non-Hermitian nonlinear SALT equations directly on top of a finite element discretization without the need of introducing a so-called constant-flux basis.

### 3.1 Maxwell-Bloch equations

The foundations of semiclassical laser theory are the Maxwell-Bloch equations, which have independently been derived by Arecchi and Bonifacio [50,51]. Here, the electric field is described classically via Maxwell's equations and the gain material is modeled as an ensemble of identical two-level atoms with a level

spacing of  $\hbar\omega_a$ . These two-level atoms are pumped via an external source  $D_0(\mathbf{x})$ , which leads to a population inversion  $D(\mathbf{x}, t)$  of the two level atoms. The interaction of the electric field and the ensemble of two-level atoms is treated quantum mechanically [1]. The resulting Maxwell-Bloch equations (in SALT units) are given by

$$\nabla \times \nabla \times \mathbf{E} + \frac{1}{c^2} \varepsilon_c \ddot{\mathbf{E}} = -\frac{1}{c^2} \ddot{\mathbf{P}} \quad (3.1a)$$

$$\dot{\mathbf{P}} = -(i\omega_a + \gamma_\perp) \mathbf{P} - i\gamma_\perp \mathbf{E} D \quad (3.1b)$$

$$\dot{D} = \gamma_\parallel \left[ D_0 - D + \frac{i}{2} (\mathbf{E} \cdot \mathbf{P}^* - \mathbf{P} \cdot \mathbf{E}^*) \right], \quad (3.1c)$$

where  $\mathbf{E}(\mathbf{x}, t)$ ,  $\mathbf{P}(\mathbf{x}, t)$ , and  $D(\mathbf{x}, t)$  correspond to the electric field, the polarization, and the inversion, respectively. The passive permittivity of the system is given by  $\varepsilon_c$ .  $\gamma_\perp$  and  $\gamma_\parallel$  are the relaxation rates of the polarization and inversion.  $D_0(\mathbf{x})$  denotes the external pump applied to the system. Note, that in Eq. (3.1c) the rotating wave approximation has already been applied. In addition to Eq. (3.1a), the electric field,  $\mathbf{E}$ , needs to satisfy outgoing boundary conditions (see section 2.3.1).

### 3.1.1 SALT units

Equations (3.1) are given in SALT units, however, one can easily retrieve the SI units by transforming  $\mathbf{E}$ ,  $\mathbf{P}$ , and  $D$  as follows

$$\mathbf{E}_{\text{SI}} = \frac{2g}{\hbar\sqrt{\gamma_\parallel\gamma_\perp}} \mathbf{E} = e_{\text{SI}} \mathbf{E} \quad (3.2)$$

$$\mathbf{P}_{\text{SI}} = \frac{2g}{\hbar\varepsilon_0\sqrt{\gamma_\parallel\gamma_\perp}} \mathbf{P} = p_{\text{SI}} \mathbf{P} \quad (3.3)$$

$$D_{\text{SI}} = \frac{g^2}{\hbar\gamma_\perp\varepsilon_0} D = d_{\text{SI}} D, \quad (3.4)$$

where  $g$  is the transition dipole moment of the two-level system.

## 3.2 Ansatz and approximations

The coupled system of nonlinear, non-Hermitian, and time-dependent equations (3.1) can in general only be integrated numerically. Such calculations are, however, computationally very demanding, even with the power of today's computers [52–54]. However, often one is not interested in the full laser dynamics as described by the Maxwell-Bloch equations, but only in the steady-state lasing behavior. For this case, the electric field is primarily composed of a superposition of modes with discrete frequencies  $\omega_\mu$ . Hence, under the assumption that the polarization follows the electric field instantaneously, we can make the following ansatz for the electric field and the polarization

$$\begin{aligned}\mathbf{E}(\mathbf{x}, t) &= \sum_{\mu=1}^N \mathbf{E}_\mu(\mathbf{x}) e^{-i\omega_\mu t} \\ \mathbf{P}(\mathbf{x}, t) &= \sum_{\mu=1}^N \mathbf{P}_\mu(\mathbf{x}) e^{-i\omega_\mu t},\end{aligned}\tag{3.5}$$

where both the real frequencies  $\omega_\mu$ , as well as the actual number of lasing modes  $N$  are yet to be determined. Inserting this ansatz into Eq. (3.1b) one immediately notices that a simple solution only exists when the inversion  $D(\mathbf{x}, t)$  does not depend on time. However, when inserting ansatz (3.5) into the MWB equation for the inversion, Eq. (3.1c), we get

$$\dot{D} = \gamma_{\parallel} \left[ D_0 - D + \frac{i}{2} \sum_{\mu=1}^N \sum_{\nu=1}^N (\mathbf{E}_\mu \cdot \mathbf{P}_\nu^* e^{-i(\omega_\mu - \omega_\nu)t} - \text{c.c.}) \right],\tag{3.6}$$

which shows that the inversion can only be approximately independent of time when the beating terms of the electric field and the polarization are neglected. In order to estimate when this is allowed in the long-term limit, i.e., for  $t \rightarrow \infty$ , we make the following ansatz for the inversion

$$D(\mathbf{x}, t) = \tilde{D}(\mathbf{x}, t) e^{-\gamma_{\parallel} t},\tag{3.7}$$

which we insert into Eq. (3.6) and integrate over time yielding

$$\begin{aligned} \tilde{D}(\mathbf{x}, t) = & \tilde{D}(\mathbf{x}, 0) + \gamma_{\parallel} D_0(\mathbf{x}) \int_0^t d\tau e^{\gamma_{\parallel} \tau} + \\ & + \frac{i\gamma_{\parallel}}{2} \sum_{\mu, \nu} [\mathbf{E}_{\mu} \cdot \mathbf{P}_{\nu}^* \int_0^t d\tau e^{-i(\omega_{\mu} - \omega_{\nu})\tau + \gamma_{\parallel} \tau} - c.c.]. \end{aligned} \quad (3.8)$$

By evaluating the integrals and inserting the resulting  $\tilde{D}(\mathbf{x}, t)$  back into Eq. (3.7) we get

$$\begin{aligned} D(\mathbf{x}, t) = & \tilde{D}(\mathbf{x}, 0)e^{-\gamma_{\parallel} t} + D_0(\mathbf{x})[1 - e^{-\gamma_{\parallel} t}] \\ & + \frac{i\gamma_{\parallel}}{2} \left[ \sum_{\mu, \nu} \mathbf{E}_{\mu} \cdot \mathbf{P}_{\nu}^* \frac{e^{-i(\omega_{\mu} - \omega_{\nu})t} - e^{-\gamma_{\parallel} t}}{\gamma_{\parallel} - i(\omega_{\mu} - \omega_{\nu})} - c.c. \right]. \end{aligned} \quad (3.9)$$

From here we can obtain the long-term limit of the inversion  $D(\mathbf{x}, t)$  by taking the limit  $t \rightarrow \infty$ ,

$$D(\mathbf{x}, t) \stackrel{t \rightarrow \infty}{\cong} D_0(\mathbf{x}) - \frac{1}{2} \left[ \sum_{\mu, \nu} \mathbf{E}_{\mu} \cdot \mathbf{P}_{\nu}^* \frac{\gamma_{\parallel}}{\omega_{\mu} - \omega_{\nu} + i\gamma_{\parallel}} e^{-i(\omega_{\mu} - \omega_{\nu})t} + c.c. \right]. \quad (3.10)$$

From this solution we can estimate that the beating terms with  $\mu \neq \nu$  can only be neglected if  $\gamma_{\parallel} \ll |\omega_{\mu} - \omega_{\nu}|$ . Under the assumption that all modes  $\mathbf{E}_{\mu}$  feature a roughly similar intensity one can extend this criterion even further to  $\gamma_{\parallel} \ll \min(|\omega_{\mu} - \omega_{\nu}|)/N$  since the sum contains  $N(N - 1)$  beating terms and  $N$  stationary terms. When these criteria are fulfilled one can simplify the Maxwell-Bloch equation for the inversion under the stationary inversion approximation (SIA), i.e.,  $\dot{D} = 0$ , to

$$D(\mathbf{x}, t) \underset{\text{SIA}}{\approx} D_0(\mathbf{x}) + \frac{i}{2} \left[ \sum_{\mu} \mathbf{E}_{\mu} \cdot \mathbf{P}_{\mu}^* - c.c. \right] \quad (3.11)$$

Note, that for single-mode lasing there are no beating terms and this approximation is in fact exact. For the case that the mode beating cannot be ignored entirely, one can extend SALT to include the beating terms while only disregarding further sidebands of the laser as we will show in Sec. 5.5.

### 3.3 SALT equations

When the SIA holds we can obtain the modal polarization  $\mathbf{P}_\mu$  from Eq. (3.1b) as,

$$\mathbf{P}_\mu = \Gamma_\mu \mathbf{E}_\mu D, \quad (3.12)$$

where

$$\Gamma_\mu = \frac{\gamma_\perp}{\omega_\mu - \omega_a + i\gamma_\perp}. \quad (3.13)$$

Inserting this expression for  $\mathbf{P}_\mu$  back into (3.11) the expression for the inversion can be simplified to

$$D(\mathbf{x}) = \frac{D_0(\mathbf{x})}{1 + \sum_{\mu=1}^N |\Gamma_\mu \mathbf{E}_\mu|^2}. \quad (3.14)$$

Substituting this term back into Eq. (3.12) and inserting the result together with the SALT ansatz (3.5) into Eq. (3.1a) yields the SALT equations

$$\left\{ \nabla \times \nabla \times - \left[ \varepsilon_c + \frac{\gamma_\perp}{\omega_\mu - \omega_a + i\gamma_\perp} \frac{D_0(\mathbf{x})}{1 + \sum_{\mu=1}^N |\Gamma_\mu \mathbf{E}_\mu|^2} \right] \omega_\mu^2 \right\} \mathbf{E}_\mu = 0. \quad (3.15)$$

The SALT equations are a set of  $N$  non-Hermitian, nonlinearly coupled partial differential equations. Note, that a priori the number of modes  $N$ , the (real) frequencies  $\omega_\mu$ , as well as, the electric field modes  $\mathbf{E}_\mu$  are all unknown and need to be determined self-consistently when solving Eq. (3.15). Note that Eq. (3.15) is still very similar to a non-Hermitian Maxwell/Helmholtz equation similar to the one we have used in section 2.3.1. However, it contains a modified electric permittivity  $\varepsilon$ , which not only includes the passive dielectric constant of the cavities  $\varepsilon_c$ , but in addition an active nonlinear part. This latter term accounts both for gain pulling as well as for gain saturation via spatial hole burning.

The only approximation necessary, as discussed above, for deriving the SALT equations is the stationary inversion approximation. Note in particular that the slowly varying envelope approximation, which reduces the accuracy of the Maxwell-Bloch equations, is not necessary for SALT as it doesn't provide any speedup when solving the SALT equations numerically and [53].

Since the nonlinear term in the SALT equation only involves the sum of the absolute squares of all modes, a SALT solution consisting of  $N$  modes is independent of the individual phases of any mode of the solution. Hence, for

arbitrary real values of the phase  $\varphi_\mu$ , the transformation,

$$\mathbf{E}_\mu \rightarrow e^{i\varphi_\mu} \mathbf{E}_\mu, \quad (3.16)$$

on each mode  $\mathbf{E}_\mu$  of a SALT solution is still a valid solution of Eq. (3.15).

Furthermore, since SALT treats the full spatial fields of the laser modes it can accurately model both the nonlinear interactions of the modes as well as all spatial variations of the pump  $D_0(\mathbf{x})$ . Especially the latter property is of interest for accurately modeling the pump-induced EP as outlined in chapter 2. In general, we can define a pump parameter  $d$ , which in addition to varying the overall pump strength can represent diverse experimental pump protocols evolving along a ‘‘pump trajectory’’  $D_0(\mathbf{x}, d)$ . Note, that when not all parts of the gain medium of the laser are pumped, the unexcited parts of the medium will be strongly absorbing - a situation, which can be modeled in SALT by using negative values for  $D_0(\mathbf{x}, d)$  in these parts of the system.

### 3.4 Modal output power

A laser mode is typically characterized both by its frequency  $\omega_\mu$  and by its output power  $P_\mu$ . While the first quantity is directly obtained in the process of solving the SALT Eqs. (3.15), the latter one is extracted from the electric field  $\mathbf{E}_\mu$  in a postprocessing step. The output power of a single SALT mode can be obtained from Poynting’s theorem [55] as

$$P_\mu = \int_{\partial\mathcal{V}} \mathbf{S}_\mu = \omega_\mu \int_{\mathcal{V}} \text{Im}(\varepsilon) |\mathbf{E}_\mu|^2, \quad (3.17)$$

where  $\mathbf{S}_\mu$  is the Poynting vector. The output power is here determined as the energy flowing through the boundary  $\partial\mathcal{V}$  of a volume  $\mathcal{V}$  surrounding the laser. By inserting the electric permittivity  $\varepsilon$  from Eq. (3.15) into (3.17) we obtain

$$P_\mu = \omega_\mu \int_{\mathcal{C}} \left[ \frac{|\Gamma_\mu|^2 D_0}{1 + \sum_\mu |\Gamma_\mu \mathbf{E}_\mu|^2} - \text{Im}(\varepsilon_c) \right] |\mathbf{E}_\mu|^2. \quad (3.18)$$

Since both the pump  $D_0$  as well as the imaginary part of the dielectric constant are only non-zero within the laser cavity, the integral can be limited to the corresponding region  $\mathcal{C}$ . The modal output power  $P_\mu$  is here given in SALT units

(c.f. 3.1.1) and the output power in SI units can be recovered by multiplying with  $\varepsilon_0 e_{\text{SI}}^2$ .

### 3.5 Solution strategy

In this section we will give an overview on how to solve the nonlinear SALT equations. In principle one can separate the solution procedure for the SALT equations into two parts:

- Finding the number of active laser modes  $N$  and checking the stability of the SALT solution
- Solving the nonlinear SALT equations (3.15) for a given number of  $N$  active laser modes

Both of these tasks are intertwined with each other. Once the SALT equations have been solved for a given number of modes  $N$ , the output, comprised by the set of laser modes  $\mathbf{E}_\mu$  and corresponding frequencies  $\omega_\mu$ , is used to check if any additional mode might be lasing in the system. If this is the case, the check will provide an estimate for the mode that is assumed to lase and it is used as a guess for the nonlinear solver of the SALT equations. In the following we will outline both procedures in detail.

#### 3.5.1 Finding the number of active laser modes $N$

In addition to the active laser modes an infinite number of additional eigenmodes exists. Since, however, these modes do not contribute to the steady-state behavior of the system they should be exponentially decaying modes, which are characterized by a complex frequency  $\bar{\omega}_\mu$  with negative imaginary part. These modes are affected through spatial hole burning from the active laser modes, which saturate the available gain particularly at the active modes' anti-nodes. The idea behind checking for additional lasing modes of the system is therefore to calculate all eigenmodes of the system under the influence of the spatial hole

burning. If not all other eigenmodes of the system decay, then the system is assumed to be unstable as the other modes would grow exponentially in time when excited. A more rigorous way to determine the stability will be given in chapter 5.

For calculating the eigenmodes of the system we assume that we have already found a solution  $\mathbf{E}_\mu, \omega_\mu$  of  $N$  modes which solves the SALT equations. From this solution one can calculate the spatial hole burning contributions and subsequently the steady-state inversion  $D(\mathbf{x}, d)$  via Eq. (3.14). When fixing the spatial hole burning contributions in the SALT Eqs. (3.15), one effectively reduces the problem to a nonlinear eigenvalue problem

$$\left\{ \nabla \times \nabla \times - \left[ \varepsilon_c + \frac{\gamma_\perp}{\bar{\omega}_\mu - \omega_a + i\gamma_\perp} \frac{D_0(\mathbf{x}, d)}{1 + \sum_{\mu=1}^N |\Gamma_\mu \mathbf{E}_\mu|^2} \right] \bar{\omega}_\mu^2 \right\} \bar{\mathbf{E}}_\mu = 0, \quad (3.19)$$

with eigenmodes  $\bar{\mathbf{E}}_\mu$  and in general complex eigenfrequencies  $\bar{\omega}_\mu$ , which we denote by a overbar. Note, that this eigenvalue problem is only nonlinear in the eigenvalues and not in the eigenvectors. These complex eigenfrequencies correspond to the poles of the scattering matrix for a system which is described by the *active* electric permittivity  $\varepsilon(\mathbf{x})$  including both the dielectric function  $\varepsilon_c$  as well as an amplifying term with the spatial hole burning contributions of the active modes. Note, that all active eigenmodes  $\mathbf{E}_\mu$  with a (real) eigenfrequency  $\omega_\mu$  are eigensolutions of Eq. (3.19) as well. In general, it is sufficient to only calculate the eigensolutions of Eq. (3.19) in a small complex region around the peak gain frequency  $\omega_a$ . In the real part, this region is bounded approximately by the gain width  $\omega_a \pm \gamma_\perp$ . Since  $\bar{\Gamma}_\mu = \frac{\gamma_\perp}{\bar{\omega}_\mu - \omega_a + i\gamma_\perp}$  is singular for  $\bar{\omega}_\mu = \omega_a - i\gamma_\perp$ , the imaginary part of the region needs to be bounded from below by  $\gamma_\perp$ .

After solving the nonlinear eigenvalue problem, a SALT solution is considered to be valid when all eigenvalues  $\bar{\omega}_\mu$  except for the lasing modes satisfy  $\text{Im}(\bar{\omega}_\mu) < 0$ . If this is not the case the mode with the greatest imaginary part can be used as the initial guess for an additional mode by feeding it back into the solver for the SALT equations.

Note, that the same procedure can also be applied when the system is below the laser threshold. Here, however, only the trivial solution  $\mathbf{E}_\mu = 0$  of the



SALT equation exists and, therefore, the inversion is simply given by the external pump  $D_0(\mathbf{x})$ . The above procedure can, however, still be applied and used to check for the threshold of the first active laser mode.

### 3.5.2 Solving the SALT equation

The SALT Eqs. (3.15) are a system of nonlinearly coupled partial differential equations. They are both nonlinear in the fields  $\mathbf{E}_\mu$  as well as in the laser frequencies  $\omega_\mu$ . As we have discussed in the previous section, when an originally inactive mode crosses the laser threshold, the corresponding field of the mode,  $\mathbf{E}_\nu$ , and the real part of its complex frequency,  $\bar{\omega}_\nu$ , are already a good approximation for the active mode close above threshold since its spatial hole burning contributions will be small. With such a suitable guess, the SALT equations can be solved using a standard multi-dimensional Newton-Raphson solver. However, there are two minor hitches:

The SALT equations including the outgoing boundary conditions do not provide enough information to solve for both the fields  $\mathbf{E}_\mu$  and the frequencies  $\omega_\mu$ . This can easily be circumvented by using the fact that for a solution of the SALT equation every mode  $\mathbf{E}_\mu$  is invariant with regard to a global phase  $\varphi_\mu$ . By fixing the global phase for each of the modes  $\mathbf{E}_\mu$  one obtains an additional constraint, which enables us to solve for both the fields  $\mathbf{E}_\mu$ , as well as the frequencies  $\omega_\mu$  [56].

Furthermore, note that the trivial solution  $\mathbf{E}_\mu = 0$  always solves the SALT equations. When solving the SALT equations numerically, this fact can be a nuisance for modes very close to threshold. Here, the amplitude of the corresponding mode is small such that the solver may wrongly converge to the trivial solution. In order to avoid this problem, we rewrite the SALT equation such that the amplitude of the mode is determined as an additional quantity similar to the frequency  $\omega_\mu$ . In order to solve the problem in this case, an additional necessary constraint needs to be applied to the set of equations. This constraint is obtained by not only fixing the global phase of each mode  $\mathbf{E}_\mu$ , but instead fixing the global (complex) amplitude of the mode. For this we rewrite

$\mathbf{E}_\mu = a_\mu \mathbf{F}_\mu$ , where  $a_\mu$  is the complex amplitude for mode  $\mu$ . The SALT equations for the field  $\mathbf{F}_\mu$  then read

$$\left\{ \nabla \times \nabla \times - \left[ \varepsilon_c + \frac{\gamma_\perp}{\omega_\mu - \omega_a + i\gamma_\perp} \frac{D_0(\mathbf{x})}{1 + \sum_{\mu=1}^N |\Gamma_\mu a_\mu \mathbf{F}_\mu|^2} \right] \omega_\mu^2 \right\} \mathbf{F}_\mu = 0. \quad (3.20)$$

In order to be able to solve Eq. (3.20) for the  $N$  solutions  $\{\mathbf{F}_\mu, \omega_\mu, a_\mu\}$ , we use the additional constraints that  $\|\mathbf{F}_\mu\|_\infty = 1.0$  and  $\mathbf{F}_\mu(\mathbf{x}_{\max}) = 1.0$ , where the latter fixes the global phase of  $\mathbf{F}_\mu$  such that the imaginary part of  $\mathbf{F}_\mu(\mathbf{x})$  is zero at the mode's maximum.

Since all lasing modes are coupled together through the spatial hole burning term, the SALT equations need to be solved for all modes simultaneously. In general such a system of nonlinear equations can be written as

$$\mathbf{f}(\mathbf{v}) = 0, \quad (3.21)$$

where  $\mathbf{v}$  includes all unknowns  $\mathbf{F}_\mu, \omega_\mu, a_\mu$ . We then solve this type of nonlinear problem using a Newton-Raphson method [57]. The idea behind this method is, that given a suitable guess  $\mathbf{v}_0$ , which in our case comes from the nonlinear eigenvalue problem discussed in the previous section, one can estimate

$$\mathbf{v} - \mathbf{v}_0 = -\mathcal{J}(\mathbf{v}_0)^{-1} \mathbf{f}(\mathbf{v}_0) + \mathcal{O}(|\mathbf{v} - \mathbf{v}_0|^2), \quad (3.22)$$

where  $\mathcal{J}$  is the Jacobian of  $\mathbf{f}(\mathbf{v})$  at  $\mathbf{v}_0$ . By iterating only the linear terms of Eq. (3.22),  $\mathbf{v}$  converges ‘‘quadratically’’ if the initial guess  $\mathbf{v}_0$  is sufficiently close to the actual solution  $\mathbf{v}$  [54].

### 3.5.3 Example: slab cavity laser

In order to demonstrate the scheme for solving the SALT equations let us consider the simplest laser system consisting of a one-dimensional slab cavity of index of refraction  $n = 1.2$ , length  $\tilde{L}$ , and a perfect mirror on one side of the slab. The gain medium is given by the Lorentzian gain curve with a peak gain frequency of  $\omega_a = 10.0 \tilde{L}$  and a half width half maximum (HWHM) of  $\gamma_\perp = 1.0 \tilde{L}$ . The slab is uniformly pumped such that  $D_0(\mathbf{x}, d) = d$  within the laser cavity and

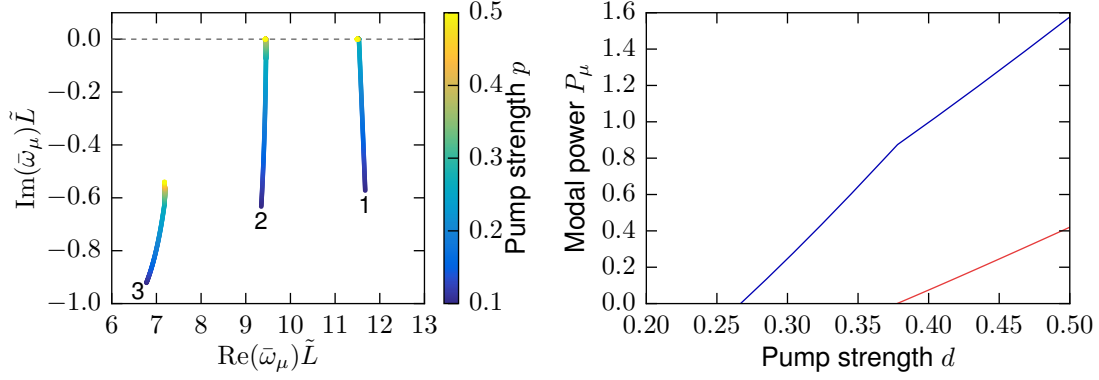


**Figure 3.1:** Example solution of the SALT for a simple 1D slab cavity. (left panel) Complex frequencies  $\omega_\mu$  in dependence of the pump strength  $p$ . (right panel) Modal power of the laser mode  $\mathbf{E}_\mu$ .

$D_0(\mathbf{x}, d) = 0$  outside. We assume that the pump  $d$  of the system is adiabatically increased starting from a value of 0.1 at which point the system is still below threshold. Here, the system does not lase as the loss due to the open boundary condition is not compensated by the gain in the system. Therefore only the trivial solution  $\mathbf{E}_\mu=0$  exists for Eq. (3.15) and the system is below threshold. Hence, the nonlinear eigenvalue problem of Eq. (3.19) yields only decaying solutions. The corresponding complex eigenfrequencies of the three inactive modes closest to the gain center  $\omega_a$  are shown in the left panel of Fig. 3.1. The labels of the modes are ordered by their threshold pump strength. When increasing the pump strength  $d$  above  $\approx 0.27$  the complex eigenvalue  $\bar{\omega}_1$  of mode 1 crosses the real axis and therefore the laser threshold. At this point, one uses the corresponding mode  $\bar{\mathbf{E}}_1$  and the real part of  $\bar{\omega}_1$  as a guess for the lasing solution  $\{\mathbf{E}_1, \omega_1\}$  to solve the nonlinear SALT Eq. (3.15). While increasing the pump strength  $d$  in small steps, we solve the SALT Eq. (3.15) at each step with the solution of the previous step as a guess. The modal power of the SALT modes above threshold are shown in the right panel of Fig. 3.1. In addition to the SALT equation we solve the nonlinear eigenvalue problem of Eq. (3.19) for which the SALT solution at the current pump step is used to check for another mode with  $\text{Im}(\omega_\nu) \geq 0$ . This occurs at a pump strength of  $d \approx 0.37$ , such that the corre-

sponding mode has to be included in the nonlinear SALT Eq. (3.15) to find a two-mode SALT solution. The pump is then further increased while tracking the SALT solutions.

This procedure will be used throughout this thesis in order to calculate the lasing behavior of the system while modifying the pump in the system. Note, however, that this procedure can be applied to the variation of any input parameter of the system. In chapter 5, we will refine this procedure by taking into account the linear stability of the SALT.

## 3.6 Numerical implementation

So far we have given a general overview on how to deal with the nonlinearity of the SALT equations while varying the pump parameter  $d$ . In this section, we will present a method for implementing this procedure numerically. At first we will give a short review of the approach for solving the SALT equations by expanding the laser modes in constant flux states [18] and explain its shortcomings. Next, we show how to efficiently implement the outgoing boundary conditions in such a way that the computational domain can be truncated to a small region surrounding the laser cavities of interest. Finally, we will describe how to implement both the nonlinear eigenvalue problem of Eq. (3.19) as well as the full nonlinear system of PDEs given by the SALT equations (3.15) numerically using a finite element method.

### 3.6.1 Review: constant-flux state approach

In the original formulation of SALT, which originated as the ab-initio self-consistent (AISC) laser theory [17–19], the SALT equations were not discretized directly but instead the modes  $E_\mu$  were expanded in a constant flux (CF) state basis. CF-states have originally been formulated by Kapur and Peierls for the problem of neutron decay [58], but have subsequently been reintroduced in the context of SALT [18]. Similar to quasi-bound states these states are the eigenstates of a harmonic Maxwell's equation with outgoing boundary conditions

(c.f. Eq. (2.5) in section 2.3.1). However, in contrast to the QB states the frequency does not correspond to the eigenvalue of the mode, but is instead given as an input parameter. In the most recent formulation, these states are determined by the *linear* non-Hermitian eigenvalue problem,

$$[-\nabla \times \nabla \times + \omega^2 \varepsilon_c(\mathbf{x}) + \omega^2 \eta_n(\omega) f(\mathbf{x})] \mathbf{u}_n(\mathbf{x}, \omega) = 0, \quad (3.23)$$

which defines the set of CF-states  $\mathbf{u}_n(\mathbf{x}, \omega)$  with eigenvalues  $\eta_n(\omega)$  that is optimal for a pump profile given by  $D_0(\mathbf{x}, d) = d f(\mathbf{x})$  [19]. One advantage of using CF-states in comparison to, for example, the QB-states is that these states are biorthogonal with respect to each other

$$\int f(\mathbf{x}) \mathbf{u}_n(\mathbf{x}, \omega) \cdot \mathbf{u}_m(\mathbf{x}, \omega) d\mathbf{x} = \delta_{nm}. \quad (3.24)$$

In addition, since the frequency outside the laser cavity is always real, the CF-states feature a constant flux outside the cavity, hence their name. This is in contrast to QB-states, where the flux increases exponentially with the distance from the laser cavity due to the negative imaginary part of their complex frequency outside the cavity. Note, that the spatial profile  $f(\mathbf{x})$  of the external pump is only non-zero within the laser cavity and as such the integral in Eq. (3.24) can be constrained to the laser cavity. A laser mode  $\mathbf{E}_\mu$  can then be expanded in terms of CF-states as

$$\mathbf{E}_\mu(\mathbf{x}) = \sum_{n=1}^{N_{\text{CF}}} c_n^\mu \mathbf{u}_n(\mathbf{x}, \omega_\mu). \quad (3.25)$$

For high-Q cavities and weak pump strengths  $D_0(\mathbf{x})$  the sum can be truncated to only a small number  $N_{\text{CF}}$  as here typically one CF-state is already a relatively good approximation of the laser mode, which has been used in the context of the single pole approximation (SPA) of SALT [19]. The expansion of laser modes in Eq. (3.25), however, already shows a weakness of the approach. Neglecting the few cases where CF-states and the corresponding eigenvalues can be calculated analytically, the eigenvalue problem determining the CF-states need to be solved for every frequency  $\omega_\mu$ . One can circumvent this problem, by calculating the CF-states at multiple steps in the frequency interval  $[\omega_a - \alpha\gamma_\perp, \omega_a + \alpha\gamma_\perp]$

and by interpolating the CF-states in between to obtain the CF-states at arbitrary frequencies within this interval. For large cavities, where the Lorentzian gain curve is much wider than the free spectral range, and especially for three-dimensional systems, however, this procedure is problematic with regard to the memory consumption of the stored CF-states and quickly becomes the limiting factor for increasing the system size.

When solving the SALT equation, the Newton-Raphson method requires the calculation of the Jacobian of the nonlinear problem with regard to the coefficients  $c_n^\mu$ . The Jacobian corresponds to a dense matrix with  $(N \times N_{\text{CF}})^2$  matrix entries. Although a convoluted analytic expression for the Jacobian exists, the Jacobian is typically calculated numerically using a finite difference scheme, which for an increasing number of modes and CF-states becomes computationally expensive.

Due to these restrictions the CF-state basis is therefore not ideal for solving the SALT equations and we will instead solve the SALT equations directly on top of a finite element discretization. However, first we will discuss how the outgoing boundary conditions (see 2.3.1) can be implemented for this case.

### 3.6.2 Perfectly matched layer

We implement outgoing boundary conditions using a perfectly matched layer (PML). Here, an absorptive medium is placed around the laser cavity and absorbs incident electromagnetic waves in all directions with practically no back reflections [59]. For this we use a uniaxial PML, which for the Helmholtz-type SALT equation can be implemented by using an artificial dielectric function  $\bar{\bar{\epsilon}}_s$  and magnetic permeability  $\bar{\bar{\mu}}_s$  inside the PML [60]. The corresponding stationary Maxwell equation for a vectorial field  $\Psi_\mu$  is given by

$$\nabla \times (\bar{\bar{\mu}}_s)^{-1} \nabla \times \mathbf{E}_\mu - \omega_\mu^2 \bar{\bar{\epsilon}}_s \mathbf{E}_\mu = 0. \quad (3.26)$$

Inside the cavity and surrounding regions but not within the PML  $\bar{\bar{\epsilon}}_s$  is a  $3 \times 3$  diagonal matrix and each entry is given by the (scalar) nonlinear dielectric function of SALT as discussed above. Inside the PML, both  $\bar{\bar{\mu}}_s$  and  $\bar{\bar{\epsilon}}_s$  are defined

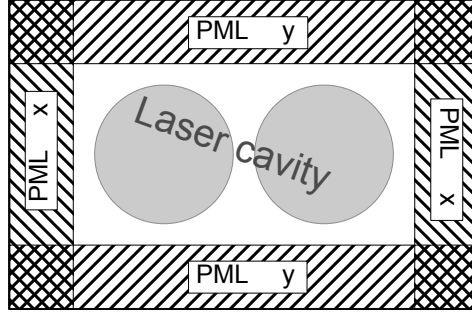


**Figure 3.2:** Sketch of the perfectly matched layer as implemented by the SALT solver.

as  $3 \times 3$  matrices,

$$\bar{\bar{\epsilon}}_s = \bar{\bar{\epsilon}}_s = \begin{bmatrix} \frac{s_y s_z}{s_x} & 0 & 0 \\ 0 & \frac{s_x s_y}{s_y} & 0 \\ 0 & 0 & \frac{s_x s_y}{s_z} \end{bmatrix} \quad (3.27)$$

where the PML scale factors  $s_w$ , for  $w = x, y, z$ , are given by

$$s_w = \begin{cases} 1 - i \frac{\sigma}{\omega_{\text{ch}}} & \text{inside the PML } \perp w, \\ 1 & \text{elsewhere} \end{cases}. \quad (3.28)$$

Here,  $\sigma$  is the PML-loss parameter and  $\omega_{\text{ch}}$  the characteristic wave frequency to be absorbed by the PML. For SALT calculations this can be typically chosen to be  $\omega_a$ , since the width of the gain curve,  $\gamma_{\perp}$ , is typically narrow in comparison to  $\omega_a$ . For ease of notation, we will refer to the magnetic permeability  $\bar{\bar{\mu}}_s$  and dielectric function  $\bar{\bar{\epsilon}}_s$ , by  $\mu$  and  $\epsilon$ , respectively. The PML can be neglected for the nonlinear active part of the electric permittivity since this term is by definition constrained to the laser cavity and as such vanishes inside the PML.

### 3.7 Finite element discretization of SALT

We have implemented the solver for solving the SALT equations on top of a finite element discretization. For this we use the finite element method as implemented by the FEniCS software collection [61]. Compared to the CF-state

approach we discretize the SALT equations directly without the need of first projecting the modes of the system on a constant flux basis [18,54].

### 3.7.1 Solving the SALT equation (3.15)

For a finite element discretization of the SALT Eqs. (3.15), we first need to find the corresponding weak form of this set of partial differential equations. Note, that we assume here that a PML is used and therefore already include the artificial magnetic permeability, which is needed for incorporating the outgoing boundary conditions. The weak form of SALT is obtained by multiplying Eq. (3.15) by a test function  $\mathbf{v}(\mathbf{x})$ , using the identity

$$\nabla \cdot (\mathbf{a} \times \mathbf{b}) = (\nabla \times \mathbf{a}) \cdot \mathbf{b} - \mathbf{a} \cdot (\nabla \times \mathbf{b}) \quad (3.29)$$

and applying Green's theorem. The resulting term with the surface integral along the boundary of the geometry can be neglected as the mode vanishes there due to the presence of the PML. The weak form of the SALT equations is then given by

$$\int_{\Omega} (\mu^{-1} \cdot \nabla \times \mathbf{E}_{\mu})(\nabla \times \mathbf{v}) - \left[ \varepsilon + \frac{\gamma_{\perp}}{\omega_{\mu} - \omega_a + i\gamma_{\perp}} \frac{D_0(\mathbf{x})}{1 + \sum_{\nu=1}^N |\Gamma_{\nu} \mathbf{E}_{\nu}|^2} \right] \omega_{\mu}^2 \mathbf{E}_{\mu} \cdot \mathbf{v} \, d\mathbf{x} = 0. \quad (3.30)$$

As outlined in section 3.5.2, we need to take the symbolic derivative of Eq. (3.30) with respect to  $\mathbf{E}_{\mu}$  and  $\omega_{\mu}$  for solving the equation using a Newton-Raphson scheme. For this we need to separate Eq. (3.30) into two equations for the real and imaginary part of  $\mathbf{E}_{\mu}$ , respectively, since the SALT equations are not differentiable in the complex fields due to the absolute square of the modes  $\mathbf{E}_{\mu}$  in the spatial hole burning denominator. In comparison to reference [54], we perform this separation already on the level of the weak form as this simplifies the implementation with FEniCS. The complex form (3.30) can be rewritten as two real forms by splitting the modes  $\mathbf{E}_{\mu} = \mathbf{E}_{\mu,r} + i\mathbf{E}_{\mu,i}$ , as well as the inverse of the artificial magnetic permeability  $\mu^{-1} = \mu_r^{-1} + i\mu_i^{-1}$  and the dielectric function  $\varepsilon = \varepsilon_r + i\varepsilon_i$  into their real and imaginary components and collecting the



imaginary unit into an *imaginary* test function  $v_i = iv$ . In addition we relabel the remaining *real* test function as  $v_r = v$ . This results in two real forms

$$\begin{aligned} & \int (\mu_r^{-1} \nabla \times \mathbf{E}_{\mu,r})(\nabla \times \mathbf{v}_r) - (\mu_i^{-1} \nabla \times \mathbf{E}_{\mu,i})(\nabla \times \mathbf{v}_r) + \\ & + \left(\frac{\omega_\mu}{c}\right)^2 \left[ \frac{\gamma_\perp (\omega_\mu - \omega_a) D \mathbf{E}_{\mu,r} + \gamma_\perp \mathbf{E}_{\mu,i}}{(\omega_\mu - \omega_a)^2 + \gamma_\perp^2} + \mathbf{E}_{\mu,r} \varepsilon_r - \mathbf{E}_{\mu,i} \varepsilon_i \right] \cdot \mathbf{v}_r \, dx = 0 \end{aligned} \quad (3.31)$$

and

$$\begin{aligned} & \int_\Omega (\mu_r^{-1} \nabla \times \mathbf{E}_{\mu,i})(\nabla \times \mathbf{v}_i) + (\mu_i^{-1} \nabla \times \mathbf{E}_{\mu,r})(\nabla \times \mathbf{v}_i) + \\ & + \left(\frac{\omega_\mu}{c}\right)^2 \left[ \frac{\gamma_\perp (\omega_\mu - \omega_a) D \mathbf{E}_{\mu,i} - \gamma_\perp \mathbf{E}_{\mu,r}}{(\omega_\mu - \omega_a)^2 + \gamma_\perp^2} + \mathbf{E}_{\mu,r} \varepsilon_i + \mathbf{E}_{\mu,i} \varepsilon_r \right] \cdot \mathbf{v}_i \, dx = 0. \end{aligned} \quad (3.32)$$

For both equations one still needs to insert the (real) inversion  $D$  from Eq. (3.14). The advantage of using FEniCS for solving this coupled nonlinear set of equations is that from these expressions FEniCS can automatically symbolically derive the Jacobian necessary for the Newton Raphson solution procedure. It therefore eliminates the tedious task of manually assembling the Jacobian [54, 62]. In comparison to the CF-state method as reviewed in section 3.23 the Jacobian is no longer a dense, but instead a sparse matrix.

In our numerical calculations, where we use the FEniCS software collection, we use the PETSc library [63] in order to solve the sparse linear system in each iteration of the Newton-Raphson solver.

### 3.7.2 Solving the nonlinear eigenvalue problem of Eq. (3.19)

In order to find a suitable guess for the SALT equations (3.15) and to check for the threshold of a laser mode, we need to solve the eigenvalue problem of Eq. (3.19). Here, we can assume that the inversion  $D(\mathbf{x}, d, \{\mathbf{E}_\mu, \omega_\mu\})$  is fixed by a given solution of the SALT equations. This also includes the case when the system is not lasing, where the inversion is simply given by the pump  $D_0$ .

In contrast to the SALT equation, the nonlinear complex eigenvalue problem of Eq. (3.19) is only nonlinear in the complex frequency  $\bar{\omega}_\mu$ , but linear in the eigenvector  $\bar{\mathbf{E}}_\mu$ . The resulting eigenvalue problem is thus of the form

$$\mathcal{T}(\bar{\omega}_\mu) \bar{\mathbf{E}}_\mu = 0. \quad (3.33)$$

Several different strategies for solving this problem exist [64, 65]. In the following we will present several of these and discuss their advantages and disadvantages. First, we note, that the nonlinear eigenvalue problem, which we consider here, is in fact a rational eigenvalue problem. One way to solve this problem is to divide Eq. (3.19) by  $\Gamma_\mu$ , which effectively results in a cubic eigenvalue problem. However, solving the cubic eigenvalue problem as such has the disadvantage of increasing the size of the problem threefold and the resulting matrix is possibly ill-conditioned. Furthermore, it is important to note, that the problem features a singularity at the point  $\omega_a - i\gamma_\perp$ , which can result in spurious numerical solutions.

The only eigenvalues relevant in SALT calculations are located close to the center of the gain curve  $\omega_a$ . Hence, it is sufficient to restrict the calculation of eigenvalues to a cropped region of the complex plane given by  $\{z \in \mathbb{C} | \text{Im}(z) > -\gamma_\perp \wedge \text{Re}(z) \in [\omega_a - \gamma_\perp, \omega_a + \gamma_\perp]\}$ . One way to find all eigenvalues within such a region of the complex plane is a contour integral method developed in [66, 67]. There the calculation of eigenvalues is restricted to a confined region with a smooth contour. Making use of the residue theorem, all poles of  $\mathcal{T}^{-1}$ , which correspond to the eigenvalues of  $\mathcal{T}$ , are found within the contour. This method has the advantage that all eigenvalues within the contour can easily be found, however, it is computationally relatively expensive as one needs to solve  $N \times M$  linear systems of the fully discretized system, where  $N$  corresponds to the number of eigenmodes within the contour and  $M$  to the integration points along the contour.

In most calculations, however, only a couple of relevant inactive modes close to threshold need to be considered. Furthermore, for the case of resonators with a high Q factor, the spatial fields of these modes are only weakly affected by the spatial hole burning contributions of the active modes. Hence, one strategy for calculating only the relevant inactive modes is the following: One first starts by calculating the quasi-bound modes of the system close to the center of the gain curve, which we have already discussed in section 2.3.1. Next, each of these modes is used as a guess for a nonlinear solver in order to find a solution to

Eq. (3.19). For this one can again use Newton's method, which we have already discussed for the case of solving the SALT equation [68]. In comparison to the SALT equations, this has the advantage that since the problem is differentiable in all unknowns, one can work with the complex fields and frequencies directly<sup>1</sup> and the convergence of the problem is "quadratic".

In most cases, we are not only interested in the SALT solution for a fixed set of parameters, but instead we want to study the behavior of the laser system under variation of one of the parameters as, e.g., the pump strength or pump parameter. One then typically scans this parameter in discrete steps. In this case, it is not necessary to recalculate the QB-states in each step, but one can then simply use the inactive modes from the last step and track the inactive modes along with the full SALT solutions  $\{\mathbf{E}_\mu, \omega_\mu\}$  of the system.

---

<sup>1</sup>As of this writing, the FEniCS software collection unfortunately does not yet support complex finite element spaces. Hence, when implementing the solver for the inactive modes, we still need to split the complex fields into the corresponding real and imaginary parts as shown for the case of the SALT equations in section 3.7.1

# Study of exceptional points in coupled cavity lasers with SALT

In this chapter we will revisit the system of two coupled 1D cavities from section 2.3 and study the influence of the EP on the system's lasing behavior in more detail with the help of SALT. Furthermore, we will demonstrate that the EP is not specific to the case of one-dimensional coupled cavities but also occurs for a realistic system of two coupled microdisk lasers and a distributed feedback laser with a loss grating.

## 4.1 Two coupled cavities in 1D

The system of coupled cavities as discussed in section 2.3 (see also the two insets of Fig. 4.1) consists of two one-dimensional cavities of length  $\tilde{L}$  with index of refraction  $n = 3.0 + 0.13i$  surrounded by air, where  $n = 1$ . Note, that the unpumped cavities are strongly absorbing when the system is not pumped. A gap of  $0.1\tilde{L}$  separates the two cavities. For the SALT calculations we used the following parametrization of the pump: For  $0 < d < 1$ , the pump in the left cavity is linearly increased in the range  $0 < D < 1.2$ , and, for  $1 < d < 2$ , the same is done in the right cavity while keeping the pump in the left cavity at 1.2.

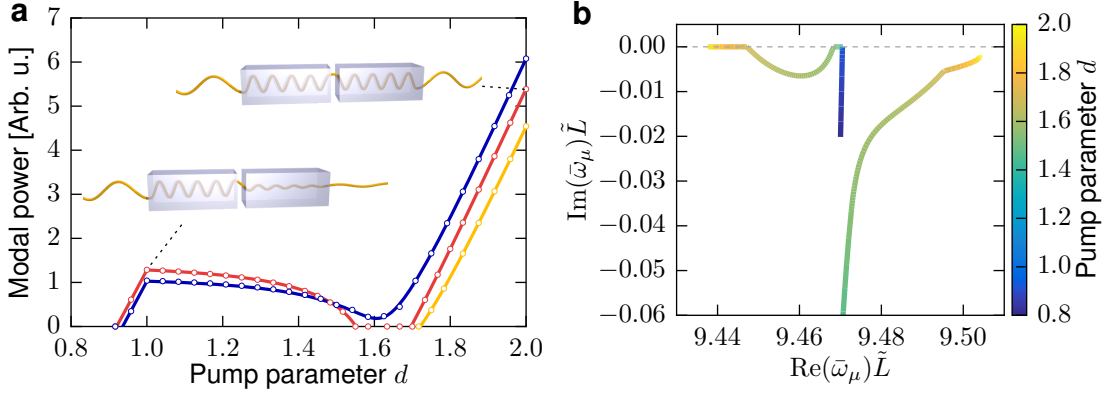


**Figure 4.1:** Lasing behavior as determined by SALT for a system of two coupled 1D cavities with dimensions as given in the text. (a) Dependence of the power output on the pump parameter  $d$ . The results are shown for three different gain curves at  $\omega_a \tilde{L} = 9.46, 9.24,$  and  $9.63$ , which correspond to the red, yellow, and blue curves, respectively. Note, that for all curves the power reduces around  $d \approx 1.6$ . The dots represent the results obtained from a full Maxwell-Bloch solver and show excellent agreement with the SALT results [69,70]. The insets depict the cavity setup together with the field of the lasing mode for  $\omega_a \tilde{L} = 9.46$  at the pump parameters  $d = 1$  and  $d = 2$ . (b) Movement of the complex frequencies of the two modes closest to the center of the gain curve under variation of the pump parameter  $d$ . Only the results for  $\omega_a \tilde{L} = 9.46$  are shown. Note, that in comparison to Fig. 2.4 the results have been obtained using SALT such that all active lasing modes feature a real frequency  $\omega_\mu$  due to the contributions from spatial hole burning. Complex frequencies with  $\text{Im}(\tilde{\omega}_\mu) < 0$  represent inactive modes.

Outside of the cavities the pump  $D_0$  has been chosen to be 0. The gain curve describing the homogeneously broadened amplifying gain medium has a half width at half maximum of  $\gamma_\perp \tilde{L} = 0.1$  and a central gain frequency of  $\omega_a \tilde{L} = 9.46$ .

The results obtained from the SALT calculations are shown in Fig. 4.1 and confirm the results from the coupled mode theory in section 2.3, i.e., the laser power output strongly decreases close to an EP. The pump has been chosen such that the system starts lasing even for the case when only one of the cavities is pumped. Here, only the left cavity is pumped in a pump parameter range  $0 < d < 1$ , where the cavity is pumped up to a maximum pump strength of  $D_0 = 1.2$ . For  $\omega_a \tilde{L} = 9.46$ , the output power of the system is given by the red

curve in Fig. 4.1a. At pump parameter  $d \approx 0.92$  the system reaches threshold. At this point the dominant weight of the lasing mode is primarily located within the amplifying cavity and decreases exponentially in the other cavity (see inset in Fig. 4.1a, where the amplitude of the electric field of the corresponding mode is shown). The complex frequency of the corresponding mode is depicted in Fig. 4.1b. Below the laser threshold of  $d \approx 0.92$ , the complex frequency of the dark blue mode moves towards the real axis for increasing values of  $d$ . After reaching the threshold the mode's frequency  $\omega_1$  remains real due to the nonlinear spatial hole burning interaction. This is in contrast to the results from the simple frequency-domain Maxwell equations in section 2.3.1, where the mode's self-interaction was not taken into account.

In the second pump range,  $1 < d < 2$ , only the pump  $D_0$  in the right cavity is linearly increased from 0 to 1.2, and the pump in the left cavity is kept constant at a value of  $D_0 = 1.2$ . As seen in Fig. 4.1 the output power of the laser at first slightly decreases despite an overall increase of the pump applied to the system and the real frequency of  $\omega_1$  changes only slightly. In contrast to that, the imaginary part of a second mode with complex frequency  $\bar{\omega}_2$  increases quickly and enters Fig. 4.1 at  $d \approx 1.64$ . In the same manner as described in section 2.3.1 an avoided crossing between modes 1 and 2 induces the shutdown of the first laser mode for the pump parameter range from 1.55 to 1.7. After the avoided crossing mode 1 starts lasing again. The spatial hole burning interaction then not only keeps the frequency of mode 1 real, but also affects the non-interacting complex eigenfrequency of mode 2 as can be seen by a kink in its complex eigenfrequency trajectory. For the chosen parameters, the second mode doesn't reach threshold and the system stays single-mode.

The same SALT calculations were repeated for two additional gain center frequencies, which are displayed as the yellow and blue curve in Fig. 4.1a, respectively. All other input parameters were not modified. The blue curve shows the results for  $\omega_a \tilde{L} = 9.63$ . Here, the laser doesn't completely shut down, but only features an output power minimum close to  $d \approx 1.6$ . For  $\omega_a \tilde{L} = 9.63$ , the results of which are shown in Fig. 4.1a by the yellow curve, the laser only starts

lasing after passing the EP.

In order to verify that the results are stable, our colleague Alexander Cerjan from Yale University has tested the SALT calculations against a full time-dependent Maxwell-Bloch solver. We have found an excellent agreement between the SALT results and the full Maxwell-Bloch results. The latter results are shown in Fig. 4.1a as white dots on top of the SALT results.

So far the calculations have shown that for a couple of different gain curve parameters,  $\omega_a$  and  $\gamma_\perp$ , a shutdown or loss in the power output occurs. However, the EP to which we have attributed this phenomenon in chapter 2.3 was not directly accessible in the SALT calculations. To alleviate this issue we are going to use constant flux states, which we have introduced in section 3.23 to find a measure that is both independent of the gain curve parameters and shows an EP directly.

The CF-states are defined by the non-Hermitian eigenvalue problem in Eq. (3.23) with eigenvalues  $\eta_n(\omega, d)$ . These states are parametrized by the frequency  $\omega$  outside the system as well as by the pump parameter  $d$ . In addition, these states depend on the same parameters as the full SALT calculations except for the definition of the gain curve defined by  $\omega_a$  and  $\gamma_\perp$ . When comparing the definition of the CF-states, Eq. (3.23), with the SALT Eq. (3.15), we observe that at threshold, i.e. , when the spatial hole burning contributions are negligible, a CF-state exactly corresponds to a threshold laser mode when the following condition is satisfied [19, 69]

$$\eta_n(\omega, d) = \frac{\gamma_\perp}{\omega - \omega_a + i\gamma_\perp}. \quad (4.1)$$

For a specific gain curve the first laser mode is determined out of the countably infinite set of eigenvalues  $\eta_n(\omega, d)$  as the one which satisfies Eq. (4.1) for the smallest value of  $d_\mu$ , which in turn also yields the threshold lasing frequency  $\omega_\mu$ . The lasing mode  $\mathbf{E}_\mu(\mathbf{x})$  at the threshold is then just given by the corresponding eigenstate  $\mathbf{u}_n(\omega_\mu, d_\mu; \mathbf{x})$ .

In order to exactly reach an EP of the system, it is in general required to tune two parameters [20]. Since the linear non-Hermitian eigenvalue problem

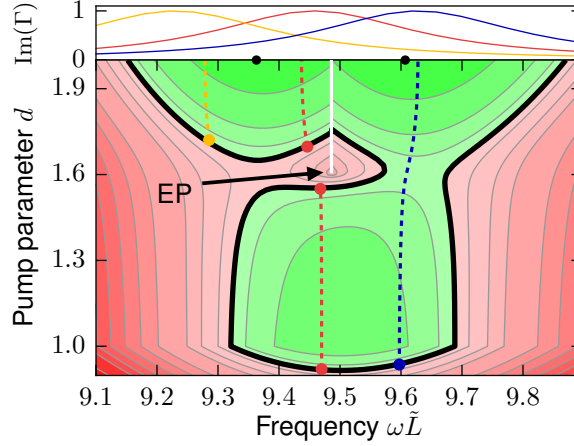


**Figure 4.2:** Contour plot of the function  $f(k, d)$ , which indicates the parameter regions of  $k$  and  $d$  where the laser in 4.1 is above threshold (green, inside black contour) or below threshold (red, outside black contour). The threshold condition,  $f(k, d) = 0$ , is satisfied at the solid black contour. The EP in the center of the plot pulls the laser below the threshold in its vicinity. The frequency dependence of the solutions of the nonlinear SALT equations (dashed lines) and the corresponding laser thresholds (dots on the solid black contour) are provided for the same gain curves (shown in the top panel) as in Fig. 4.1. The evaluation of  $f(k, d)$  involves two interconnected Riemann sheets (see Fig. 4.3), resulting in a cut between the two sheets (see the white line right above the EP). The two black dots at the upper edge of the plot represent the resonance frequencies of the passive cavity system.

of Eq. (3.23), can, however, be solved for arbitrary values of the frequency  $\omega$  and pump parameters  $d$ , we are thus naturally provided with such two continuous parameters. This brings us to the central insight that Eq. (3.23), which determines the lasing thresholds, can already contain the EPs that control the lasing behavior shown in 4.1.

To show this explicitly, we rewrite the complex Eq. (4.1) as two real conditions which neatly separate the role of the CF-spectrum and the gain curve

$$|\eta_n|^2 + \text{Im}(\eta_n) = 0 \quad (4.2a)$$

$$\frac{\omega - \omega_a}{\gamma_\perp} = \frac{\text{Im}(\eta_n) + 1}{\text{Re}(\eta_n)}. \quad (4.2b)$$

$$(4.2c)$$



Equation (4.2a) has the remarkable property of being entirely independent of the gain curve parameters  $\omega_a$  and  $\gamma_\perp$ . Hence, it defines a threshold boundary in the  $\omega, d$  plane dividing lasing and nonlasing regions, solely based on the values of  $\{\eta_n\}$ . To conveniently capture the entire  $\omega, d$  landscape of possible lasing solutions, we define a function

$$f(\omega, d) \equiv \min_n [|\eta_n|^2 + \text{Im}(\eta_n)], \quad (4.3)$$

which has the property that the contour  $f(\omega, d) = 0$  is the locus of all possible lasing thresholds. The actual lasing thresholds on this contour are then determined by the gain curve parameters in Eq. (4.2b). In Fig. 4.2, we show the relevant regions of  $f(\omega, d)$  above ( $f < 0$ , green, within black contour) and below ( $f > 0$ , red, outside black contour) threshold, as well as the threshold boundary ( $f = 0$ , black contour). When  $f < 0$ , the CF-states do not give the full lasing solutions and the nonlinear SALT is needed to find the output power and frequency, as was done for the curves showing the modal output power in Fig. 4.1, as well as for the frequency curves in Fig. 4.2.

The most striking feature of the contour plot shown in Fig. 4.2 is the existence of a substantial inclusion of a subthreshold region (red, outside black contour) in the midst of the superthreshold region (green, within black contour). At the center of this inclusion is a local maximum of  $f$ ; this point corresponds to an EP of Eq. (3.23). For the middle gain curve (red), there are three threshold solutions, two very near the EP. If we order these solutions according to increasing pump,  $d$ , we find that  $\partial f/\partial d < 0$  at the first and third thresholds and  $\partial f/\partial d > 0$  at the second. As a function of  $d$ , the laser thus turns on-off-on, just as found in Fig. 4.1. Hence, nonlinear effects play no role in the qualitative behavior of this laser; they only determine the amplitude of the lasing emission in the green region. All the interesting behavior is controlled by the EP: It completely suppresses lasing in its vicinity of  $\omega$  and  $d$ -parameters, thereby causing the reentrant lasing (red curve) as well as the nonmonotonic but continuous lasing emission (blue curve), which is influenced by its proximity to the EP.

In the entire  $\omega$  and  $d$  range shown in Fig. 4.2, exactly only two eigenvalues  $\eta_{1,2}$  contribute to  $f(\omega, d)$ . In the coupled cavities studied here, these two eigen-

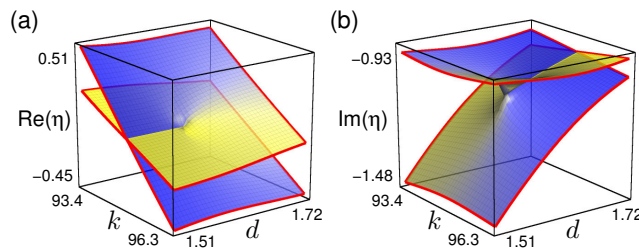


**Figure 4.3:** (a) Real and (b) imaginary parts of the two CF-eigenvalues  $\eta_{1,2}(\omega, d)$  which are closest to the threshold in the  $\omega$  and  $d$  parameter region around the laser turn-off observed in Figs. 4.1 and 4.2. The eigenvalue surfaces display the typical structure of intersecting Riemann surfaces, centered around an EP.

values are associated with a symmetric-antisymmetric doublet of passive cavity resonances (see black dots in Fig. 4.2). If both cavities are *uniformly* pumped with the same gain curves as in Fig. 4.2, the laser emits in modes each of which can be associated with one of the passive resonances (not shown). However, no EP and hence no pump-induced inclusion or nonmonotonic laser emission appears. Only when nonuniform pumping is applied may a pair of eigenvalues coalesce at an EP.

In Fig. 4.3, we plot the  $\omega$  and  $d$  dependence of the real and imaginary part of the two eigenvalues  $\eta_{1,2}$ . Focusing on the parameter region around  $d = 1.55$ , where the laser turns off, we find that the parametric dependence of the eigenvalues on  $\omega$  and  $d$  shows the typical topological structure of two intersecting Riemann sheets around an EP located at  $\omega\tilde{L} \approx 9.5, d \approx 1.6$ . Away from the EP, the laser can always “choose” the lower threshold solution for lasing (upper part of the Riemann sheet), but at the EP only one solution is available, which is a compromise between the low and high threshold solution. This gives rise to a local minimum in the effective gain and inhibits lasing in the vicinity of the EP. In this way, the essential physics of an EP directly translates into the physical effects observed in Fig. 4.1.

## 4.2 Photonic molecule

Since the laser shutdown effect close to an EP could already be demonstrated using coupled mode theory in chapter 2.3 the same effect is certainly not limited to the 1D toy model of the previous section. Therefore we will next investigate the realization of EPs for a more realistic setup involving two coupled microdisk lasers. Such lasers are ubiquitous in photonic labs and are used as cavities for lasers ranging from the THz regime [71,72] up to infrared and optical frequencies [42,73,74].

In the following we will consider a laser system with a configuration based on the photonic molecule laser described in reference [71]. The system consists of two microdisk lasers both of which have diameters smaller than the freespace wavelength. In dimensionless units the radii of both disks are given by  $0.45\tilde{L}$  and the gap between the disks amounts to  $0.1\tilde{L}$ . The gain material is modeled with a gain curve defined by a peak gain frequency  $\omega_a\tilde{L} = 5.92$  and a HWHM of  $\gamma_{\perp}\tilde{L} = 0.6$ . The index of refraction of the unpumped disks is given by  $n = 3.67 + 0.09i$ . When considering only a single microdisk, the modes with the lowest thresholds are degenerate pairs of whispering gallery modes [73,74]. Any superposition of these modes is an eigenstate of the underlying harmonic Maxwell equations (2.5) with outgoing boundary conditions. Hence, both clockwise- and counter-clockwise traveling modes, as well as two standing-wave modes with interlaced spatial intensity patterns can be formed out of a degenerate eigenpair. When coupling two of these disks the two degenerate eigensolutions of the problem form quadruplets of modes whose degeneracy is slightly broken. Since the rotational symmetry is no longer preserved, the traveling wave solutions are no longer solutions of the linear harmonic Maxwell equations. Instead super-modes with a standing wave pattern are formed from combinations of the single disk modes. A sketch of the system including the spatial intensity pattern of one of these modes is shown in the inset of Fig. 4.4a.

In the following we will apply the same pumping scheme as for the one-dimensional system. Here each of the disks is in sequence pumped up to a pump strength of  $D_0 = 0.71$ . The results as obtained with SALT are shown in

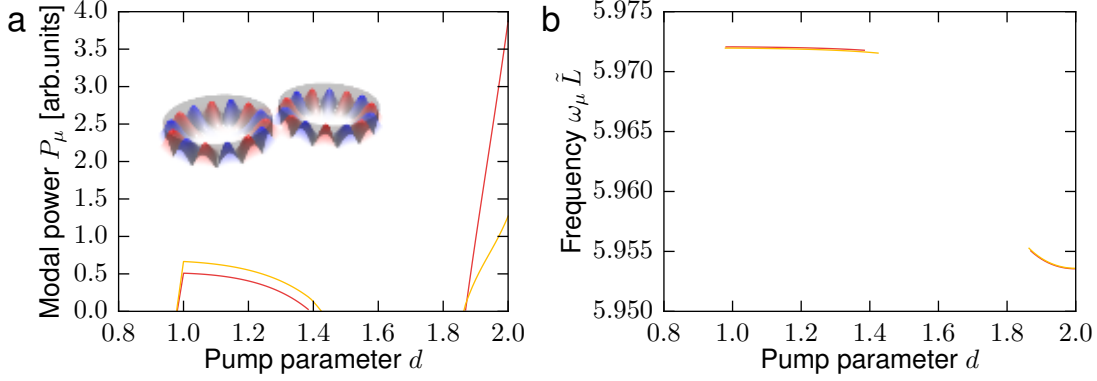


**Figure 4.4:** Modal power output (a) and mode frequencies (b) for a photonic molecule laser in dependence of the pump parameter  $d$ . The same pumping scheme is used as for the coupled 1D.

Fig. 4.4, where both the modal power output, as well as the mode frequencies are plotted with respect to the pump parameter  $d$ . Due to the near-degeneracy of the modes, not only a single mode, but two of the four near-degenerate modes start to lase according to SALT. However, both of the modes demonstrate the expected counterintuitive behavior, i.e., a laser shutdown occurs despite a continuous increase of the overall applied pump strength. In addition the lasing frequency shifts significantly between the lasing shutdown and the reemergence of lasing.

The intensity pattern of the two modes is depicted in Fig. 4.5 for pump parameters  $d = 1$  and  $d = 2$ . Here, it is clearly visible that the EP can be interpreted as a transition from modes localized in the individual disks (at  $d = 1$ ) to modes that extend over both resonators (at  $d = 2$ ).

Note, that in the calculations presented here, we have so far neglected the relaxation rate of the inversion,  $\gamma_{\parallel}$ , since it does not explicitly appear in the SALT calculations. However, its value has to be considered in order to check the validity of the stationary inversion approximation, for which the frequency splitting between any two active modes  $|\omega_\mu - \omega_\nu|$  of the laser has to be greater than  $\gamma_{\parallel}$ . For the case of the photonic molecule laser shown here and, in general, for any resonator that features nearly-degenerate modes, this condition is not

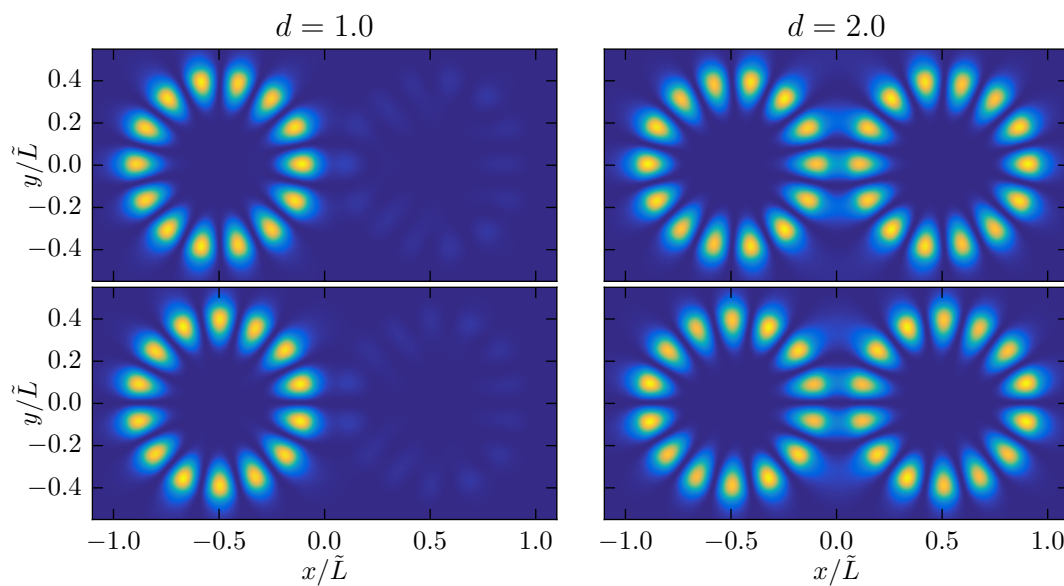


**Figure 4.5:** Intensity pattern  $|E_\mu|^2$  of the two active modes of the photonic molecule laser calculation presented in Fig. 4.4 for pump parameters  $d = 1.0$  (left panels) and  $d = 2.0$  (right panels).

fulfilled since the splitting can be arbitrarily small. A possible route in order to remedy this shortcoming will be presented in the following chapter. Note, however, that the central result of this chapter, namely the shutdown of the laser system close to the EP, is not affected by this issue, as close to the EP the system is not lasing.

### 4.3 Distributed feedback laser

In all systems that we have considered so far, we have been able to link the counterintuitive phenomenon of a laser shutdown for increasing pump values or, alternatively, an increased laser output power for decreasing pump values to the presence of an EP. As has recently been emphasized in the literature [48], similar lasing phenomena have already been described theoretically by Kogelnik and Shank for distributed feedback (DFB) lasers with a loss grating in the early seventies [47]. However, their theoretical description of loss-induced las-

ing did not involve exceptional points. In these references a simple 1D waveguide has been considered, which at first is uniformly pumped. By imposing a loss grating on this waveguide it is shown that despite increasing the overall loss of the system the system shows a strong increase in lasing intensity. The intuitive explanation for this phenomenon is that the lasing mode will adjust its shape such that the nodes of the electric field coincide with the maxima of the loss grating whereas the field's antinodes coincide with the gain maxima. In this section we revisit this problem and show that in contrast to assertions made in [48] this lasing behavior can indeed also be attributed to the presence of an EP.

For this we consider the same model for the DFB laser as in [48], featuring a one-dimensional system with a refractive index of

$$n(x) = n_0 - ig_{\text{th}} + \Lambda(1 - \cos(2\omega_0 xn_0)), \quad (4.4)$$

in the region where the laser is pumped and with a background index of  $n_0$  outside the pumped region. The modulation of the grating is determined by the Bragg frequency  $\omega_0$  and furthermore we assume that the pumped region is of an integer multiple of the Bragg-wavelength  $\frac{2\pi c}{n_0\omega_0}$  such that no additional reflections occur at the edge of the waveguide due to the grating. The (spatially constant) gain is only present in those sections where the grating is defined. Hence, small reflections can occur at the interfaces due to an index mismatch, which, even when no grating is present, already provides sufficient feedback for reaching the laser threshold. In the following calculations, the gain is chosen such that the system is at threshold for the mode closest to the Bragg frequency  $\omega_0$  when no grating is present. At first we investigate a loss grating, which is modeled by a purely positive imaginary grating parameter  $\Lambda$  similar to what has been done in [48]. For this we consider a system where the background index of refraction is given by  $n_0 = 1$ , and the Bragg frequency by  $\omega_0\tilde{L} = 100$ . The grating has a length of 40 Bragg wavelengths and the laser threshold of this system is  $g_{\text{th}} \approx 0.0185$ .

In Fig. 4.6 we show the numerically calculated complex frequencies of the QB states of the system under variation of the loss parameter  $\text{Im}(\Lambda)$ , which is

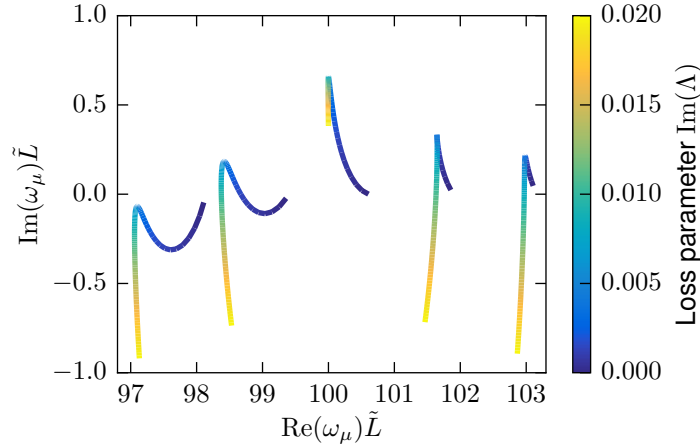


**Figure 4.6:** Evolution of the QB mode eigenfrequencies in a DFB laser with a pure loss grating.

increased from 0 to 0.02. For the mode located closest to the the Bragg frequency,  $\omega_0 \tilde{L} = 100$ , we observe a stark increase of the imaginary part of the corresponding quasibound state eigenfrequency. In addition the real part of the frequency shifts towards the Bragg frequency. The imaginary part of this mode reaches a maximum for a loss parameter of  $\text{Im}(\Lambda) \approx 0.008$  after which it decreases again.

In contrast to the preceding results of loss-induced lasing in coupled cavities, here the progression of the eigenvalues does not show an avoided crossing, which could hint at the presence of an EP. However, as we have mentioned earlier, the only general way to find an EP is to scan two parameters of the system. The quantity, which is best suited for this in this context, is the real part of the grating parameter  $\Lambda$  since in an actual experiment one can typically not precisely control only the imaginary part of the grating.

Hence, we extend the calculations to include the real part of the grating parameter  $\Lambda$ . In Fig. 4.7 we plot the dependence of the mode closest to the Bragg frequency  $\omega_0$  on the real and imaginary part of  $\Lambda$ . In Figs. 4.7a and b, we plot the real and imaginary part of the eigenvalue, respectively. The dashed red line corresponds to the result tracked in Fig. 4.6 for increasing values of  $\text{Im}(\Lambda)$ . Note, that we only varied a very small parameter range of  $\Lambda$  as compared to

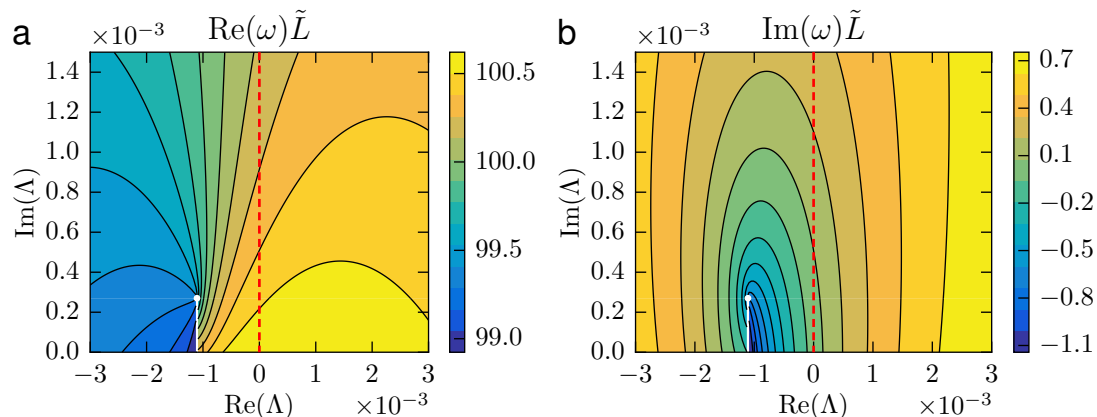


**Figure 4.7:** Real and imaginary part of the QB-mode eigenfrequency associated with the dominant mode of the DFB laser under variation of the real and imaginary part of the DFB grating in the index of refraction. The EP is marked by a white point.

Fig. 4.6. In this calculation we find an EP at  $\Lambda \approx (-1.1 + i0.27) \cdot 10^{-3}$ , which is marked by a white dot in Fig. 4.7 connecting two Riemann sheets with each other. Furthermore we can clearly observe in Fig. 4.7b that in the vicinity of the EP the imaginary part of the eigenvalue  $\omega$  features a minimum. Hence, the effect of loss-induced lasing for the loss-grating in a DFB laser can be explained in exactly the same manner as we have already done in chapter 2.3, however, here, no avoided crossing is visible as the EP connects “neighboring” modes of a single cavity instead of individual modes of neighboring resonators.

## 4.4 Open questions

In this chapter we have shown that the prediction that a laser system shuts down in the vicinity of an EP can indeed be verified with the full nonlinear model of the steady-state ab-initio laser theory. In addition we have shown that even for the case of the DFB laser with a loss grating the counterintuitive loss-induced lasing phenomenon can be attributed to the presence of an EP.

However, a couple of questions remain to be answered. For the system of two coupled cavities we have shown that the results of the SALT have to be



taken with a grain of salt since the presented results above the laser threshold do not fulfill the stationary inversion approximation for typical values of the relaxation rate of the inversion,  $\gamma_{\parallel}$ . Since this will pose a problem for arbitrary cavities with degenerate or near-degenerate modes, we will investigate in the next chapter how such systems can, in general, be treated in the context of SALT.

Furthermore, we have so far only looked at the case where the parameters were chosen such that the EP occurred when the system is actually below the laser threshold (compare Fig. 4.2) which has significantly simplified the analysis. One such issue, which has already been discussed in the literature on EPs, is that the linewidth should tend towards infinity due to a divergence of the Petermann factor [14,75]. Furthermore, since two active modes merge at an EP above the laser threshold, the stationary inversion approximation cannot be fulfilled either.

Due to these difficulties it is important to check for the stability of the system close to the EP. In this chapter, this has been done by explicitly comparing the solutions from SALT with the solutions of the full Maxwell-Bloch equations. However, numerically integrating the computationally demanding time-dependent Maxwell-Bloch equations defeats the efficiency of the SALT approach. Hence, finding a more efficient tool for determining the stability directly from the SALT solution is of importance.

# Linear stability analysis in SALT and its application for near-degenerate modes

In this chapter we will enhance the steady-state ab-initio laser theory in order to be able to treat laser resonators featuring degenerate and near-degenerate modes where the traditional SALT algorithm fails as the stationary inversion approximation is not fulfilled. In this case the (near-)degenerate modes may form a single hybridized mode, which doesn't fulfill the traditional criterion for the stability of a SALT solution, i.e.  $\forall_\nu \text{Im}(\bar{\omega}_\nu) < 0$ . Hence, in order to test the stability of such a mode we develop a linear stability analysis. This work has been executed together with my colleagues S. Burkhardt and D. Krimer and parts of the shown results have been published in [76].

We furthermore present an extension to SALT where we self-consistently incorporate the mode beating terms in the inversion and which can be used to apply SALT to input parameters where the beating terms cannot be neglected entirely.

## 5.1 Linear stability

In section 4 the stability of the SALT solutions close to the EP was determined by comparison with the results from a full time-dependent Maxwell-Bloch calculation. However, one central reason for using SALT is to avoid these computationally demanding calculations.

One possible route to avoid such expensive numerics is to perform a rigorous linear stability analysis on the SALT solutions [76]. For this, we linearize the Maxwell-Bloch Eqs. (3.1) around a given SALT solution and we check if all possible perturbations to the SALT solution are decaying. In the following we give a short overview of the derivation of this linear stability analysis.

We first extend the SALT ansatz from Eq. (3.5) as

$$\begin{aligned}\mathbf{E}(\mathbf{x}, t) &= \sum_{\mu=1}^N [\mathbf{E}_{\mu}(\mathbf{x}) + \delta\mathbf{E}_{\mu}(\mathbf{x}, t)] e^{-i\omega_{\mu}t} \\ \mathbf{P}(\mathbf{x}, t) &= \sum_{\mu=1}^N [\mathbf{P}_{\mu}(\mathbf{x}) + \delta\mathbf{P}_{\mu}(\mathbf{x}, t)] e^{-i\omega_{\mu}t} \\ D(\mathbf{x}, t) &= D(\mathbf{x}) + \delta D(\mathbf{x}, t),\end{aligned}\tag{5.1}$$

where we have added small perturbations  $\delta\mathbf{E}_{\mu}(\mathbf{x}, t)$ ,  $\delta\mathbf{P}_{\mu}(\mathbf{x}, t)$ , and  $\delta D(\mathbf{x}, t)$  around the SALT solution, the corresponding polarizations  $\mathbf{P}_{\mu}$  and inversion  $D$ . Note, that although the polarization  $\mathbf{P}_{\mu}$  induced by each mode and the inversion  $D$  are not directly obtained in the process of solving the SALT equation, one can easily obtain these quantities from the SALT solution  $\{\mathbf{E}_{\mu}, \omega_{\mu}\}$  as follows

$$\begin{aligned}D(\mathbf{x}) &= \frac{D_0(\mathbf{x})}{1 + \sum_{\mu=1}^N |\Gamma_{\mu} \mathbf{E}_{\mu}(\mathbf{x})|^2} \\ \mathbf{P}_{\mu}(\mathbf{x}) &= \Gamma_{\mu} D(\mathbf{x}) \mathbf{E}_{\mu}(\mathbf{x}).\end{aligned}\tag{5.2}$$

In comparison to [77], the ansatz (5.1) does not only capture perturbations in the amplitude of the electric field, the polarization and the inversion, but instead all spatial perturbations are taken into account. Next we insert the ansatz into the MB equations (3.1). Here, we have to differentiate between single and

multi-mode lasing. When only a single mode is active the single-mode SALT solution is also an exact solution of the Maxwell-Bloch equations. Using this and furthermore neglecting any higher-order terms of  $\delta\mathbf{E}_\mu$ ,  $\delta\mathbf{P}_\mu$ , and  $\delta D$ , we can obtain a set of partial differential equations, which rigorously describe the linearized dynamics of the perturbations for single-mode lasing. For multi-mode lasing, however, we need to neglect the beating of the modes' perturbations by applying the stationary inversion approximation similar to the original SALT approach. As a consequence, since neither a solution of the multi-mode SALT is an exact solution of the Maxwell-Bloch equations nor the perturbations are driven by the exact Maxwell-Bloch equations, spurious instabilities can occur which we will briefly discuss in section 6.2.

Inserting the ansatz, Eqs. (5.1), into the Maxwell-Bloch equations and assuming the SIA for the case of multi-mode lasing, leads to the following set of partial differential equations for the perturbations  $\delta\mathbf{E}_\mu$ ,  $\delta\mathbf{P}_\mu$ , and  $\delta D$ ,

$$\epsilon \delta\ddot{\mathbf{E}}_\mu = -\nabla \times \nabla \times \delta\mathbf{E}_\mu - \delta\ddot{\mathbf{P}}_\mu + \omega_\mu^2(\delta\mathbf{P}_\mu + \epsilon \delta\mathbf{E}_\mu) + 2i\omega_\mu(\delta\dot{\mathbf{P}}_\mu + \epsilon \delta\dot{\mathbf{E}}_\mu) \quad (5.3)$$

$$\delta\dot{\mathbf{P}}_\mu = [i(\omega_\mu - \omega_a) - \gamma_\perp] \delta\mathbf{P}_\mu - i\gamma_\perp(\mathbf{E}_\mu \delta D + \delta\mathbf{E}_\mu D) \quad (5.4)$$

$$\delta\dot{D} = -\gamma_\parallel \delta D + \frac{i\gamma_\parallel}{2} \sum_{\mu=1}^N (\delta\mathbf{E}_\mu \mathbf{P}_\mu^* + \mathbf{E}_\mu \delta\mathbf{P}_\mu^* - \delta\mathbf{E}_\mu^* \mathbf{P}_\mu - \mathbf{E}_\mu^* \delta\mathbf{P}_\mu). \quad (5.5)$$

This set of equations corresponds to  $2 \times N$  equations for the perturbations of the electric fields,  $\delta\mathbf{E}_\mu$ , and corresponding polarizations,  $\delta\mathbf{P}_\mu$ , of each mode and one equation for the perturbation of the inversion  $\delta D$ . Although the system of equations is linear in the perturbations, Eq. (5.5) contains the terms  $\delta\mathbf{E}_\mu^*$  and  $\delta\mathbf{P}_\mu^*$ , which can not be expressed by a linear combination of  $\delta\mathbf{E}_\mu$ ,  $\delta\mathbf{P}_\mu$ , and  $\delta D$ . Hence, in order to produce a fully linear system, we split the perturbed fields and polarizations, as well as the dielectric function  $\epsilon_c$  into their respective real and imaginary parts in order to obtain a purely real set of equations. Note, that since the perturbation of the inversion has already initially been real-valued, the corresponding equation can remain as it is. This procedure yields a set of  $4 \times N + 1$  real partial differential equations for the fields  $\text{Re}(\delta\mathbf{E}_\mu)$ ,  $\text{Im}(\delta\mathbf{E}_\mu)$ ,  $\text{Re}(\delta\mathbf{P}_\mu)$ ,  $\text{Im}(\delta\mathbf{P}_\mu)$ , and  $\delta D$ . Since the system of equations is now completely

linear we can summarize them as a single vector

$$\vec{F}(\mathbf{x}, t) = \begin{pmatrix} \text{Re}[\delta\mathbf{E}_\mu(\mathbf{x}, t)] \\ \text{Im}[\delta\mathbf{E}_\mu(\mathbf{x}, t)] \\ \text{Re}[\delta\mathbf{P}_\mu(\mathbf{x}, t)] \\ \text{Im}[\delta\mathbf{P}_\mu(\mathbf{x}, t)] \\ \delta D(\mathbf{x}, t) \end{pmatrix}. \quad (5.6)$$

A solution of the SALT equations is considered to be stable when all possible perturbations of the solutions decay. Hence, we make the following ansatz,  $\vec{F}(\mathbf{x}, t) = \vec{F}(\mathbf{x})e^{\sigma t}$ . By inserting this ansatz back into Eqs. (5.3)-(5.5) we obtain an eigenvalue problem with eigenvalues  $\sigma_j$  and eigenvectors  $\vec{F}_j$ . When all eigenvalues have a real part smaller than 0, i.e.  $\text{Re}(\sigma_j) < 0$ , then the solution is considered to be stable. The eigenvalue problem is given by the following set of equations

$$(\delta\mathbf{P}_{\mu,r} - \epsilon_i\delta\mathbf{E}_{\mu,i} + \epsilon_r\delta\mathbf{E}_{\mu,r})\sigma^2 + 2(\delta\mathbf{P}_{\mu,i} + \epsilon_i\delta\mathbf{E}_{\mu,r} + \epsilon_r\delta\mathbf{E}_{\mu,i})\omega_\mu\sigma - \quad (5.7a)$$

$$-(\delta\mathbf{P}_{\mu,r} - \epsilon_i\delta\mathbf{E}_{\mu,i} + \epsilon_r\delta\mathbf{E}_{\mu,r})\omega_\mu^2 + \nabla \times \nabla \times \delta\mathbf{E}_{\mu,r} = 0$$

$$(\delta\mathbf{P}_{\mu,i} + \epsilon_i\delta\mathbf{E}_{\mu,r} + \epsilon_r\delta\mathbf{E}_{\mu,i})\sigma^2 - 2(\delta\mathbf{P}_{\mu,r} - \epsilon_i\delta\mathbf{E}_{\mu,i} + \epsilon_r\delta\mathbf{E}_{\mu,r})\omega_\mu\sigma - \quad (5.7b)$$

$$-(\delta\mathbf{P}_{\mu,i} + \epsilon_i\delta\mathbf{E}_{\mu,r} + \epsilon_r\delta\mathbf{E}_{\mu,i})\omega_\mu^2 + \nabla \times \nabla \times \delta\mathbf{E}_{\mu,i} = 0$$

$$\delta\mathbf{P}_{\mu,r}\sigma + \gamma_\perp(\delta\mathbf{P}_{\mu,r} - D\delta\mathbf{E}_{\mu,i} - \delta D\mathbf{E}_{\mu,i}) + (\omega_\mu - \omega_a)\delta\mathbf{P}_{\mu,i} = 0 \quad (5.7c)$$

$$\delta\mathbf{P}_{\mu,i}\sigma + \gamma_\perp(\delta\mathbf{P}_{\mu,i} + D\delta\mathbf{E}_{\mu,r} + \delta D\mathbf{E}_{\mu,r}) - (\omega_\mu - \omega_a)\delta\mathbf{P}_{\mu,r} = 0 \quad (5.7d)$$

$$\delta D\sigma + \gamma_\parallel(\delta D + \sum_{\mu=1}^N \mathbf{P}_{\mu,r}\delta\mathbf{E}_{\mu,i} + \delta\mathbf{P}_{\mu,r}\mathbf{E}_{\mu,i} - \delta\mathbf{E}_{\mu,r}\mathbf{P}_{\mu,i} - \mathbf{E}_{\mu,r}\delta\mathbf{P}_{\mu,i}) = 0. \quad (5.7e)$$

In order to keep the equations compact, we have abbreviated  $\text{Re}(\cdot)$  and  $\text{Im}(\cdot)$  through the sub-indices r and i, respectively. Note, that the problem is quadratic in the eigenvalue  $\sigma_j$ . In the numerical calculations the quadratic dependency can be linearized by introducing two additional fields  $\delta\mathbf{G}_\mu = \sigma_j\delta\mathbf{E}_\mu$  and  $\delta\mathbf{Q}_\mu = \sigma_j\delta\mathbf{E}_\mu$  such that one ends up with  $8 \times N + 1$  real-valued equations for the eigenvalue problem. In order to be able to solve the eigenvalue problem defined by Eqs. (5.7), we need to impose outgoing boundary conditions on  $\delta\mathbf{E}_\mu$  similar as for the SALT equations. We have implemented this approach using a perfectly

matched layer as described in section 3.6.2. Note, that this requires an additional artificial magnetic permeability, which is not yet included in Eqs. (5.7) but is straightforward to add. We discretize the eigenvalue problem using a finite element method for which we use the FEniCS toolkit to assemble the generalized linearized eigenvalue problem [61]. The eigenvalue problem itself is solved using the numerical software libraries PETSc and SLEPc [78,79].

Whereas the real part of an eigenvalue  $\sigma_j$  determines the growth/decay rate of a perturbation, the imaginary part corresponds to the frequency relative to the original modes  $\mathbf{E}_\mu$  at which the perturbation is oscillating. When we detect an eigenvalue with  $\text{Re}(\sigma_j)$  greater than 0, then the corresponding SALT solution  $\mathbf{E}_\mu$  is considered to be unstable. Hence, it would be sufficient to only calculate the eigenvalue with the largest real part. However, in the current implementation due to a frequency-independent perfectly matched layer spurious numerical solutions with  $\text{Re}(\sigma_j)$  can occur for eigenvalues with  $|\text{Im}(\sigma_j)| > \omega_\mu$ . Instead of calculating the whole eigenvalue spectrum  $\{\sigma_j\}$ , we instead limit the calculation of eigenvalues to a range from 0 to  $\max(\omega_\mu)$  in the imaginary part and to real values close to the imaginary axis. The first restriction can be justified in the sense that beyond  $\text{Im}(\sigma_j) = \omega_\mu$  the rotating wave approximation is no longer valid. For 1D systems this procedure has been validated using an explicit comparison with time-dependent calculations [76].

For every active laser mode one always finds an eigenvalue at zero in the spectrum of eigenvalues  $\sigma_j$ . The reason for this is that the solutions of the SALT equations are only unique up to a global phase factor. Hence, a perturbation corresponding to such a phase shift leads to a valid solution. This eigenvalue, however, does not affect the stability of the problem. For the case of multi-mode lasing one obtains further eigenvalues with  $\text{Re}(\sigma_j) = 0$ , but with  $\text{Im}(\sigma_j)$  corresponding to all possible combinations of frequency splittings  $\Omega_\mu - \Omega_\nu$ . This can be attributed to the fact that the labeling of the SALT solutions is arbitrary. Hence, a SALT solution with the corresponding two modes  $\mathbf{E}_\mu$  and  $\mathbf{E}_\nu$  interchanged is still a solution of the SALT. Similar to the eigenvalue at  $\sigma_j = 0$  these eigenvalues do not affect the stability of the SALT solution although they are

located exactly on the stability threshold  $\text{Re}(\sigma_j) = 0$ .

Note, that since we neglect mode beating in the standard SALT Eqs. (3.15), the SALT solutions do not depend on the relaxation rate of the inversion  $\gamma_{\parallel}$ . The governing equations of linear stability on the other hand depend on this parameter. Hence, we can calculate the stability of a SALT solution for different values of this relaxation rate without the need to recalculate the SALT solution itself. Note, however, that in an actual experiment  $\gamma_{\parallel}$  is intrinsic to the gain material and hence can't be varied easily.

## 5.2 SALT for degenerate and near-degenerate modes

One deficiency of SALT is that it can't be straightforwardly applied to a resonator with degenerate or near-degenerate modes of which both are active. In this case the frequency difference  $\Delta = |\omega_{\mu} - \omega_{\nu}|$  between the two (near-) degenerate modes can be much smaller than or of the same order of magnitude as the relaxation rate of the inversion  $\gamma_{\parallel}$  such that the stationary inversion approximation does not hold. From experiments it is evident that such systems show stable stationary laser action such that SALT should be applicable [72].

In order to show how such systems can be solved with SALT we consider a 2D microdisk laser whose rotational symmetry is broken by a small wedge. The outline of such a cavity is shown in Fig. 5.1 by the white curve. The small wedge is annotated by a red arrow. The disk has a radius of  $1\tilde{L}$ , a refractive index of  $n = 2 + 0.01i$  and the wedge on the right side of the disk has a depth of  $0.05\tilde{L}$  and a width of  $0.05\tilde{L}$ . The gain parameters are  $\omega_a\tilde{L} = 4.83$  and  $\gamma_{\perp}\tilde{L} = 0.1$  and have been chosen such that only a single pair of near-degenerate modes, which in the following are labeled as mode *A* and *B*, need to be considered for a large pump range above threshold. The wedge has the effect that the two originally degenerate threshold modes of the microdisk split slightly with a frequency difference of  $\Delta\omega\tilde{L} \approx 1.4 \cdot 10^{-3}$ . Therefore, the condition for the validity of the SIA given by the condition,  $\gamma_{\parallel} \ll \Delta\omega$ , cannot be satisfied for reasonable values of

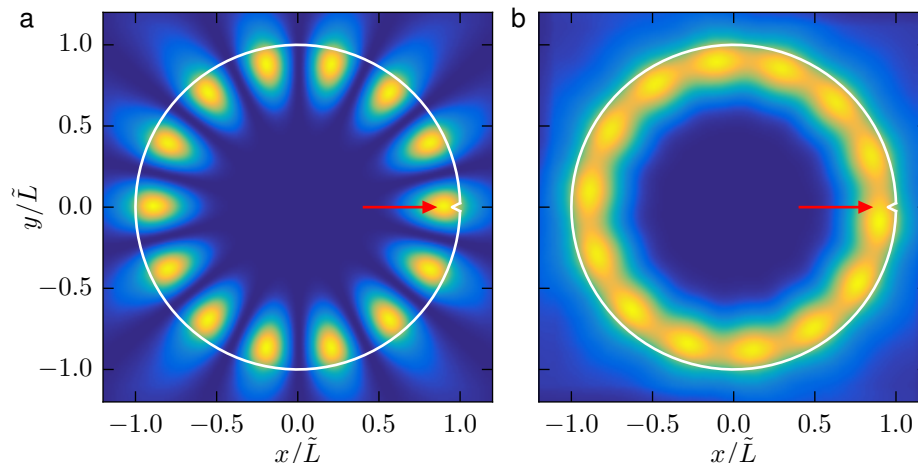


**Figure 5.1:** Single-mode lasing states for a 2D microdisk cavity perturbed by a wedge. The cavity is outlined in white with arrows marking the position of the wedge. The spatial intensity pattern of two stable single-mode solutions are shown: (a) Standing wave mode  $B$  at pump strength  $D_0 = 0.0773$  with regularly spaced nodes of intensity zero; (right) dominantly traveling wave solution  $C_1$  at pump strength  $D_0 = 0.15$ .

$\gamma_{\parallel}$  and the traditional SALT algorithm cannot be applied for the case when both modes would become active [56]. In Fig. 5.1a, the intensity pattern of one of the two degenerate passive modes is shown. The second mode features nearly the same intensity pattern, but in comparison to the mode shown in Fig. 5.1a, is rotated by a quarter wavelength such that one of its antinodes is situated right on top of the small wedge. Hence, the mode shown in Fig. 5.1a has a slightly lower threshold since the mode is less affected by the wedge. However, since both modes are nearly degenerate, their thresholds are very close to each other.

When naïvely using the solution method for SALT as described in section 3.5.2, the solution is only valid up to the pump strength where the threshold of the second mode is reached. The frequency dependence of the single mode solution on the pump parameter  $D_0$  of mode  $B$  is, among others, shown in Fig. 5.2. Using the linear stability analysis developed in the previous section we find that there is only a tiny pump range between 0.077 and 0.078, where this single mode solution corresponding to mode  $B$  is stable before the near-



degenerate partner mode reaches threshold. However, beyond this threshold the two-mode solution is not valid due to the failure of the SIA.

It is well-known that for ring and microdisk lasers with a perfect rotational symmetry the active mode corresponds to a traveling wave mode [76, 80, 81] running either in clockwise-, or counterclockwise direction. Since the perturbation induced by the wedge on the mode structures is weak, one could therefore assume that an active mode of the perturbed microdisk should be dominantly traveling in one direction as well. This, however, is in stark contrast to the passive modes of the system. As evident from the intensity pattern shown in Fig. 5.1a, the corresponding passive mode is a standing-wave mode. In the unperturbed case, the passive standing-wave modes can be superimposed to form a traveling wave mode which still corresponds to an eigenmode of the passive system. For the perturbed case, however, this is not possible since the degeneracy is slightly broken. Furthermore, since the wedge is symmetric with respect to the  $x$ -axis in Fig. 5.1, the modes have to be symmetric or anti-symmetric with respect to this symmetry axis as well. When the laser is active and the system is sufficiently pumped, however, the modes no longer have to fulfill this symmetry condition, since a broken symmetry in the modes can spontaneously break the symmetry of the electric permittivity through the spatial hole burning term.

This suggests the following approach to solve for a single mode solution of the system above threshold: One can form a superposition of modes  $A$  and  $B$  as  $\mathbf{E}_A \pm i\mathbf{E}_B$  to create a traveling wave mode  $C_{1,2}$ , which depending on the sign travels either clockwise or counter-clockwise. This mode can then be used well above threshold as a guess for the nonlinear SALT solver. Here, the mean value of the real parts of the frequencies of the passive modes can be used as an initial guess for the frequency  $\omega_{C_{1,2}}$ . Using this procedure we were indeed able to find two additional modes at a pump strength of  $D_0 = 0.15$ . The intensity pattern of one of these modes is shown in Fig. 5.1b. In comparison to an unperturbed disk, the modes are not fully traveling into one direction, but also have contributions traveling into the opposite direction as evident from the slight beating in the intensity pattern. Both modes are mirror-symmetric to each other with respect

to the  $x$ -axis and either solution is a single-mode solution of the SALT equations.

Once such a solution is found, we need to determine if the solution is a valid, stable solution. In the solution strategy discussed in section 3.5.2, we argued that a solution to the SALT equations is only accepted as a valid solution of the SALT if for a fixed spatial hole burning contribution all inactive eigenmodes of the SALT operator feature an imaginary part of their complex frequency which is less than 0. Otherwise such an inactive mode would grow exponentially in time. If this was the case, this is taken as a hint that this inactive mode is in fact active and needs to be included as an additional laser mode in the SALT calculation.

When applying this strategy to either of the active modes  $C_{1,2}$ , we indeed find that one of the inactive modes features a positive imaginary part. However, when trying to include this mode as an additional mode in the SALT solver, the calculation does not converge. Furthermore, since this additional mode is separated in frequency by less than the frequency splitting  $\Delta$  we would have the same problem as for a superposition of two active modes  $A$  and  $B$ , namely, that the SIA could not be used here.

The situation can be repaired by noticing that the original argument for evaluating the stability/validity of a SALT solution only takes into account the dynamics of a simple wave equation. The dynamics of the problem at hand is, however, determined by the Maxwell-Bloch equations. Hence, it is suggestive to use the linear stability formalism developed in the previous section to check the stability of a SALT solution.

The linear stability analysis takes into account the relaxation rate of the inversion,  $\gamma_{\parallel}$ , for which we choose a value of  $10^{-3}$  as is a reasonable value for a semiconductor microlaser with  $\gamma_{\perp} = 0.1$  [53]. Solving for the linear stability eigenvalues  $\sigma_j$  of Eq. (5.7) we find that the solution shown in Fig. 5.1b is indeed stable. Since the SALT algorithm has already been shown to agree well with full time-dependent calculations [52–54,70,76,82] this opens the question when it is necessary to perform such a full linear stability analysis compared to the simpler argument based purely on the imaginary part of the complex frequencies

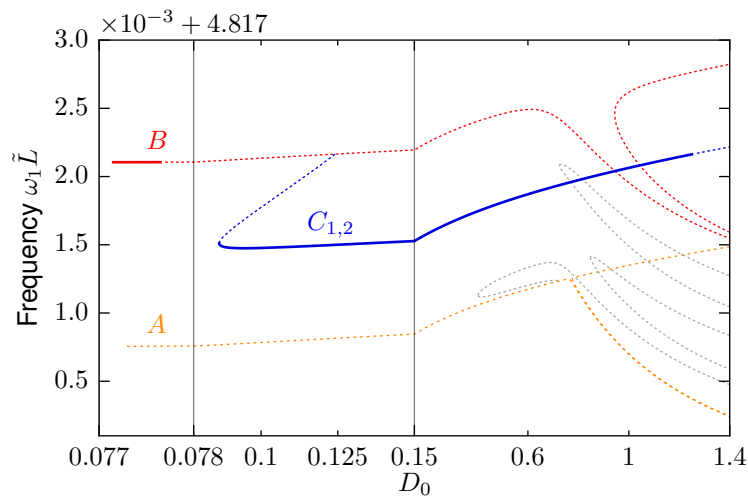


**Figure 5.2:** Laser frequencies of single-mode SALT solutions for the cavity shown in Fig. 5.1. Curves *A* (orange) and *B* (red) correspond to two standing wave solutions, which have even and odd symmetry with respect to the  $x$ -axis. The two modes represented by curve  $C_{1,2}$  (blue) feature a broken symmetry, but are mirror-symmetric to each other. Solid (dotted) lines denote a stable (unstable) solution for  $\gamma_{\parallel} = 0.01$ . Note, that the pump axis is separated into three regions of different linear scaling for the sake of clarity. The dotted gray curves represent further nonlinear single-mode SALT solutions which are never stable.

of the inactive modes.

In order to be able to answer this question it is instructive to investigate the system we have discussed so far in more detail. Since each of the one-mode SALT solutions  $C_{1,2}$  cannot appear out of nowhere they have to be connected somehow to the single-mode solutions *A* and *B* corresponding to the original near-degenerate passive modes. In order to study this connection it is therefore instructive to track all these single-mode solutions while disregarding the previous condition that all inactive modes need to feature an imaginary part less than 0. Instead we will replace this check by a linear stability analysis in each step.

In Fig. 5.2 we show the laser frequency of all single-mode solutions of the SALT equation that we have found for this system close to the original near-degenerate frequency doublet. Solid curves depict stable lasing whereas dotted

curves correspond to an unstable solution of the SALT equations as determined with a linear stability analysis for  $\gamma_{\parallel} = 10^{-2}$ . We find that at  $D_0 \approx 0.124$  the pair of solutions  $C_{1,2}$  (blue) branches off from the solution  $B$  (red). We have mentioned before that whereas mode  $B$  and mode  $A$  feature a perfect even and odd symmetry with respect to the  $x$ -axis, the solutions  $C_{1,2}$  do not possess this symmetry, but rather are mirror images of each other. We can therefore relate this branch point to the point at which the symmetry of the system is spontaneously broken. A similar phenomenon has previously been observed in simulations as well as in experiments [83].

Furthermore, note that in order to track the various single-mode solutions in Fig. 5.2, it is not sufficient to track modes for continuously increasing values of the pump  $D_0$ . Instead one needs to track these solutions by both increasing and decreasing the pump strength  $D_0$ . As an example the modes  $C_{1,2}$  are first tracked backward in pump strength starting from the branching point at  $D_0 \approx 0.124$  (see Fig. 5.2). When further reducing the pump strength, we observe that a sharp bend occurs in the frequency dependence of solutions  $C_{1,2}$  at  $D_0 \approx 0.086$ , where each of the modes  $C_{1,2}$  has evolved into a dominantly traveling wave mode. Beyond this turning point, the solutions  $C_{1,2}$  become stable in a large interval of the pump strength  $D_0$ . Note, that we have uncovered the whole branch of modes  $C_{1,2}$  by simply tracking the corresponding solution starting from the guess at  $D_0 = 0.15$  as discussed above as we have yet to find an efficient mechanism to detect the branch point directly while tracking solution  $B$ .

At  $D_0 \approx 0.8$  both (unstable) modes  $A$  (orange) and  $B$  (red) feature two further branches. These can be understood as follows: Since the wedge of the two dimensional cavity only represents a small perturbation to the system, the symmetry with respect to the  $y$ -axis is only slightly broken, and, hence, modes  $A$  and  $B$  are nearly symmetric with respect to this axis (see left panel of Fig. 5.1 for the intensity pattern of mode  $B$ ). At  $D_0 \approx 0.8$ , this near-symmetry no longer holds. However, since the modes have never been fully symmetric, there is not a single point at which the symmetry of these modes spontaneously breaks, but rather a smooth transition (as compared, e.g., to the symmetry breaking transi-

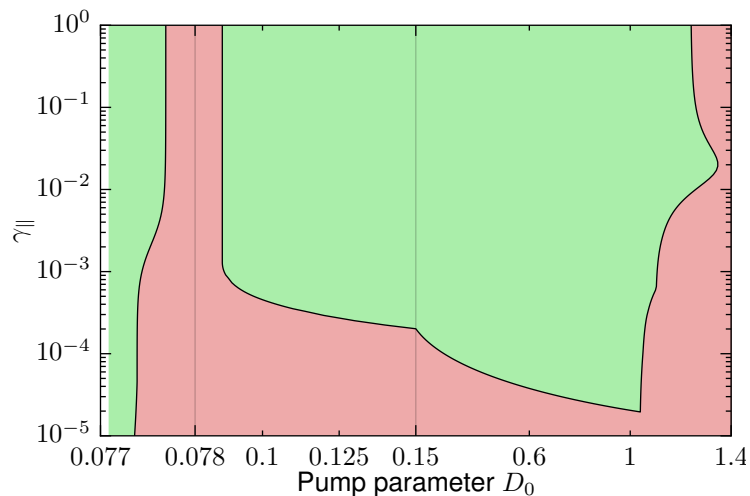


**Figure 5.3:** Stability diagram of the single-mode standing wave solution  $B$  for  $D_0 < 0.078$  and of the single-mode traveling wave solutions  $C_{1,2}$  for  $D_0 > 0.078$ . The stability results are shown with respect to the pump strength  $D_0$  and the relaxation rate of the inversion,  $\gamma_{||}$ . Green regions denote stable lasing, whereas red regions denote an unstable SALT solution.

tion with respect to the  $x$ -axis at  $D_0 \approx 0.124$ ). For mode  $B$ , this smooth transition is clearly visible in Fig. 5.2. For mode  $A$  this transition occurs in a much smaller pump interval, since mode  $A$  has a node directly located at the wedge of the 2D cavity and its symmetry is therefore only very slightly distorted.

Using similar superpositions of already known modes as starting points for the nonlinear solver, we can find several more branches of non-linearly induced single-mode SALT solutions within the plotted frequency range of Fig. 5.3 which are shown as gray curves. Note, however, that these solutions are never stable according to linear stability analysis.

In Fig. 5.2 we have only shown the stability of all single mode laser solutions for a fixed value of  $\gamma_{||}$ . Although  $\gamma_{||}$  can not easily be varied dynamically in an actual experiment as it is specific to the used gain material, it is instructive to investigate the dependence of the stability of the found solutions with respect to both the pump strength  $D_0$ , as well as  $\gamma_{||}$ . The corresponding stability diagram is shown in Fig. 5.3, where the green regions denote stable lasing and the red ones unstable lasing as found by the linear stability analysis.

The solution corresponding to mode  $B$  is found to be stable for a tiny interval of pump strength  $D_0$  on the left side of the stability diagram in Fig. 5.3. Although this stable region depends slightly on both the pump strength  $D_0$  and on  $\gamma_{\parallel}$ , it roughly corresponds to the original stability criterion  $\forall \nu, \text{Im}(\bar{\omega}_\nu) \leq 0$ , which is fulfilled (independently of  $\gamma_{\parallel}$ ) for values of  $D_0 < 0.0773$ . This is in contrast to the traveling wave solutions  $C_{1,2}$ , which are stable only for values of  $\gamma_{\parallel} > 2 \cdot 10^{-5}$ . This highlights the importance of taking into account the value of  $\gamma_{\parallel}$  for assessing the stability of a SALT mode which is not possible when only looking at the imaginary parts of the eigenmodes of the system. Furthermore we observe that even the solutions  $C_{1,2}$  only remain stable until a pump strength of  $D_0 \approx 1.3$ . This instability can be attributed to an additional mode, not included in the pair of near-degenerate modes, which would start to lase at this point. By including this additional mode as an active mode in the SALT calculations we can, similarly as in the traditional SALT algorithm, find a stable SALT solution.

### 5.3 Discussion

The results of the previous section show that stable SALT solutions can also exist for the case of multiple inactive laser modes featuring a QB mode frequency with a positive imaginary part. Hence, for a correct interpretation of the SALT results, it is required to modify the SALT algorithm such that a linear stability analysis is performed for every SALT solution. This step replaces the calculation of the inactive eigenmodes of the system. The disadvantage of this additional check is, however, that numerically it is relatively expensive to calculate the stability eigenvalues  $\sigma_j$ .

Hence, we will give a short argument on when a full linear stability analysis is strictly required: In the results shown in Fig. 5.3, we observe that the stability for the traveling wave mode strongly depends on the value for the relaxation rate of the inversion  $\gamma_{\parallel}$ . Since only the perturbation of the inversion  $\delta D$  directly depends on this quantity in the linear stability analysis (compare Eq. (5.5)), it is

evident that the coupling to the inversion is crucial for stabilizing the traveling wave solution. This can also be checked explicitly by decoupling the equation for the perturbation of the polarization [Eq. (5.4)] from the inversion by neglecting the term containing  $\delta D$ . The resulting stability eigenvalues then give the same results as the original SALT stability criterion. In order for the inversion to be able to influence the stability of a mode, it is necessary that the time-scales of the fields are of the same order of magnitude as  $\gamma_{\parallel}$ . Since the linear stability analysis as presented in section 5.1 considers all spatial perturbations, a criterion for when a linear stability analysis is strictly required when  $|\omega_{\mu} - \bar{\omega}_{\nu}|$  is of the same order of magnitude or smaller than  $\gamma_{\parallel}$ , which means that whenever the frequency spacing of an active mode  $\mu$  and any other active or inactive mode  $\nu$  is of the same order of magnitude as  $\gamma_{\parallel}$ , a linear stability analysis has to be done to ensure the stability of the solution.

## 5.4 Application: Photonic molecule laser

At this point we can revisit the system of two coupled microdisk cavities of section 4.2. For two uncoupled microdisks the whispering gallery modes of the combined disks feature a four-fold degeneracy, which in our setup is slightly broken due to the coupling. The coupling is so weak that the frequency spacing  $\Delta \approx 10^{-4}$  of the near-degenerate modes is smaller than the relaxation rate of the inversion for which we assume  $\gamma_{\parallel} \approx 10^{-3}$ . In section 4.2 we have used the unmodified SALT algorithm as presented in chapter 3, which resulted in two of the four near-degenerate passive modes lasing when the system is not close to the EP. For an easier comparison we show the corresponding data for the modal power output and laser frequency of the active modes once more as gray curves in Fig. 5.4.

Following the discussion in the previous section we expect to see the emergence of traveling wave single mode solutions when the system is pumped above threshold. In order to find this correct and stable solution we similarly make an educated guess for the traveling wave mode from the superposition of

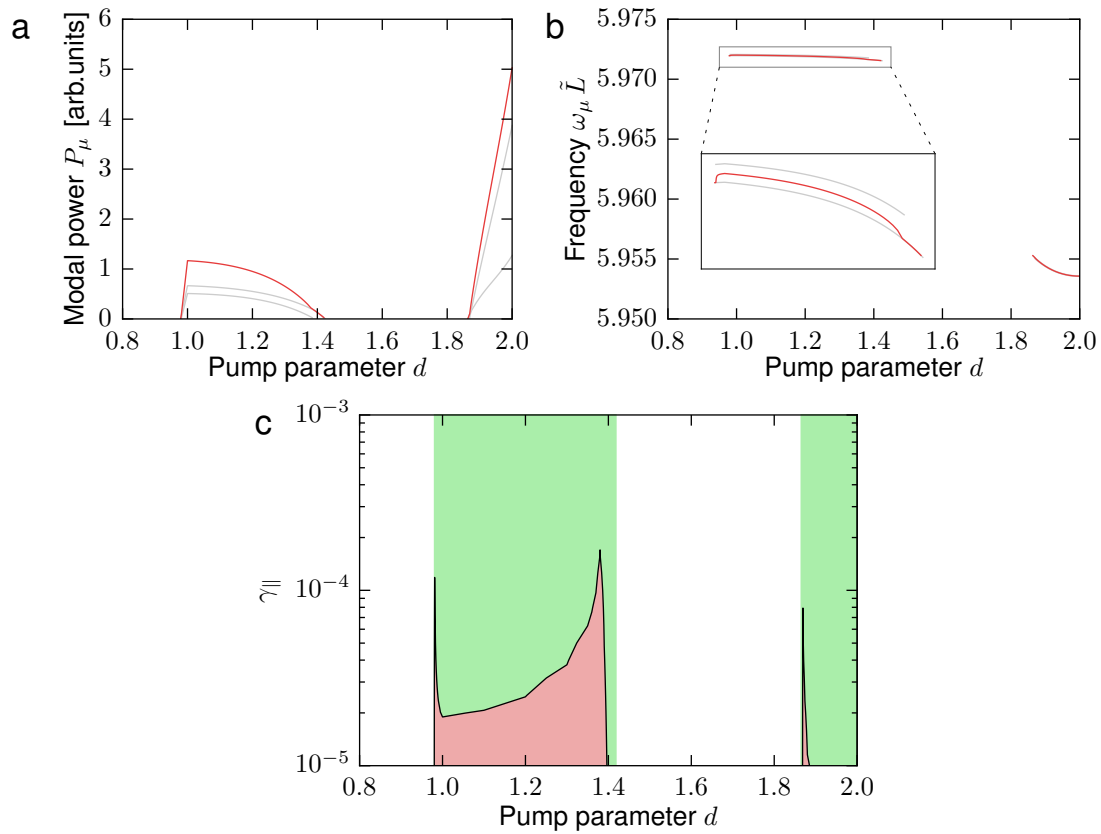


**Figure 5.4:** Dependence of the modal power (a) and the laser mode frequency (b) on the pump parameter  $d$  for the sequential pump sequence applied to a photonic molecule laser as discussed in Sec. 4.2. Both the results for the invalid traditional SALT algorithm (gray curves), and the stable traveling wave mode solution (red curves) are shown. In (c) the linear stability diagram for the traveling wave mode solution is shown in dependence of the relaxation rate of the inversion  $\gamma_{||}$ .



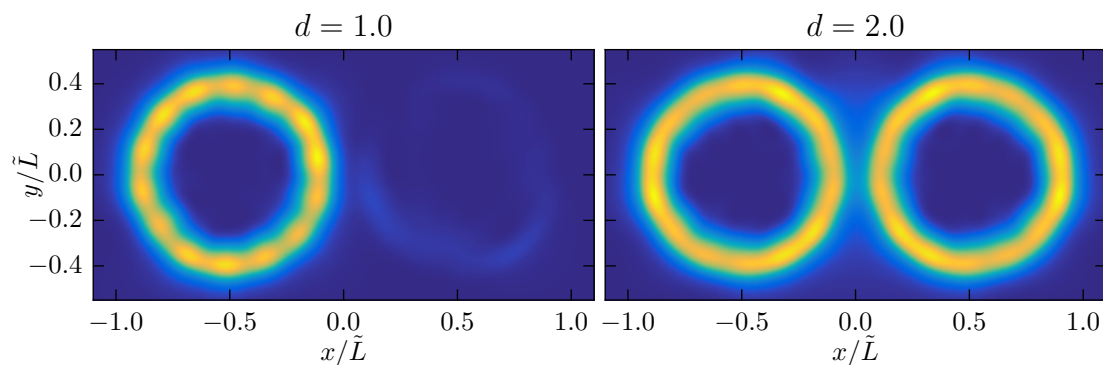


**Figure 5.5:** Intensity pattern  $|E|^2$  of one of the two traveling wave mode solutions for the photonic molecule laser evaluated at the pump parameters  $d = 1.0$  and  $d = 2.0$ . The same geometry and gain parameters are used as in section 4.2.

the invalid SALT solution by using  $\mathbf{E}_1 \pm i\mathbf{E}_2$ . Note, that each of these modes will feature the same power as well as frequency output such that we only describe one of these modes here, the other one is mirror-symmetric with respect to the symmetry axis of the system. We use this guess to solve the nonlinear SALT equations at pump parameters  $d = 1$  and  $d = 2$  for the traveling wave solution. The intensity pattern of the solution at these two pump steps are shown in Fig. 5.5.

From the solution at these two pump parameters we then track the traveling wave solution back to the branch points close to the laser threshold where they merge with the solutions from the original calculation. This can be seen in both the power output as well as the lasing frequency displayed in Fig. 5.4a,b where the traveling wave mode solution is shown by the red curve. As shown in the linear stability diagram of Fig. 5.4c we found that the traveling wave mode is in general stable for values of  $\gamma_{\parallel} \approx 10^{-3}$ . Only for much smaller values of  $\gamma_{\parallel}$  the traveling wave mode becomes unstable. Note, that the laser thresholds of the standing-wave and traveling wave SALT solutions match such that the discussion of chapter 4 on the shutdown of the laser in the vicinity of the EP remains fully valid.

## 5.5 SALT beyond the stationary inversion approximation

In this chapter we have so far extended the regime in which SALT is valid from the case in which mode beating can be completely neglected  $\gamma_{\parallel} \ll |\Delta|$  to a regime where an extremely small frequency spacing of modes enables the formation of hybridized modes due to nonlinear self-interactions. In between these two regimes, typically a great wealth of time-dependent phenomena can be observed in the laser output ranging from self-pulsations to an entire chaotic lasing behavior [1] all of which are out of reach for a steady-state model. However, another regime can be found to which SALT can be extended, i.e., when the ratio of  $\frac{\gamma_{\parallel}}{|\Delta|}$  is not sufficiently close to 0. Here, the mode beatings can yield a significant time-dependence in the inversion, but the laser sidebands, which stem from the interaction of the beatings with the modes, can still be neglected. In the following we give a short derivation of this extended theory.

Following a similar strategy as developed in [53] for a perturbative treatment of the beating terms but going beyond the two-mode simplification we extend the SALT ansatz for the electric field  $E$  and the polarization  $P$  from Eq. (3.5) with an ansatz for the inversion  $D$  that includes all mode beatings

$$D(\mathbf{x}, t) = D_s(\mathbf{x}) + \sum_{\mu=1}^N \sum_{\nu=\mu+1}^N d_{\mu\nu}(\mathbf{x}) e^{-i\Delta_{\mu\nu}t} + d_{\mu\nu}^*(\mathbf{x}) e^{i\Delta_{\mu\nu}t}, \quad (5.8)$$

where  $\Delta_{\mu\nu} = \omega_{\mu} - \omega_{\nu}$ . Furthermore, all diagonal terms  $d_{\mu\mu}$  vanish, i.e.,  $d_{\mu\mu} = 0$  for  $1 \leq \mu \leq N$ . Note, that one could take the second sum in Eq. (5.8) from 1 to  $N$  as well. This would have the advantage that the resulting equations become a bit simpler, but at the cost of twice the number of beating terms in the inversion. Next, we insert ansatz (5.8) into the MB-equation for the inversion, Eq. (3.1c), and match the time-dependent and time-independent terms, which yields

$$d_{\mu\nu} = -\frac{1}{2} \frac{\gamma_{\parallel}}{\Delta_{\mu\nu} + i\gamma_{\parallel}} (\mathbf{E}_{\mu} \cdot \mathbf{P}_{\nu}^* - \mathbf{E}_{\nu}^* \cdot \mathbf{P}_{\mu}) \quad (5.9)$$

$$D_s = D_0 - \sum_{\mu=1}^N \text{Im}(\mathbf{E}_{\mu} \cdot \mathbf{P}_{\mu}^*). \quad (5.10)$$

Similarly, we insert the SALT ansatz, Eq. (3.5), together with Eq. (5.8) into the MB-equation for the polarization, Eq. (3.1b) which yields

$$\begin{aligned} \sum_{\mu=1}^N -i\omega_{\mu} \mathbf{P}_{\mu} e^{-i\omega_{\mu} t} = & - (i\omega_a + \gamma_{\perp}) \sum_{\mu=1}^N \mathbf{P}_{\mu} e^{-i\omega_{\mu} t} - i\gamma_{\perp} \sum_{\mu=1}^N \mathbf{E}_{\mu} e^{-i\omega_{\mu} t} D_s \\ & - i\gamma_{\perp} \sum_{\mu=1}^N \sum_{\alpha=1}^N \sum_{\beta=\alpha+1}^N \left( \mathbf{E}_{\mu} e^{-i(\omega_{\mu} + \Delta_{\alpha\beta})t} d_{\alpha\beta} + \mathbf{E}_{\mu} e^{-i(\omega_{\mu} - \Delta_{\alpha\beta})t} d_{\alpha\beta}^* \right). \end{aligned} \quad (5.11)$$

In the last term of Eq. (5.11) the polarization is driven by the product of the electric field and the beating terms of the inversion. If we considered all of these terms, we would need to include the sideband modes in the ansatz for the polarization  $\mathbf{P}$  and the electric field  $\mathbf{E}$ . However, for  $\frac{\gamma_{\parallel}}{\Delta_{\mu\nu}} \ll 1$  these can be safely omitted. Thus, we will only consider the beating terms in Eq. (5.11), which contribute back to the mode frequencies  $\omega_{\mu}$ . In general, we will therefore overestimate the beating terms  $d_{\mu\nu}$  since the coupling to the sidebands of the system is neglected. The last term in Eq. (5.11) is hence approximated as

$$\sum_{\mu=1}^N \sum_{\alpha=1}^N \sum_{\beta=\alpha+1}^N \left( \mathbf{E}_{\mu} e^{-i(\omega_{\mu} + \Delta_{\alpha\beta})t} d_{\alpha\beta} + \mathbf{E}_{\mu} e^{-i(\omega_{\mu} - \Delta_{\alpha\beta})t} d_{\alpha\beta}^* \right) \quad (5.12)$$

$$\approx \sum_{\alpha=1}^N \sum_{\mu=\alpha+1}^N \mathbf{E}_{\mu} e^{-i\omega_{\alpha} t} d_{\alpha\mu} + \sum_{\mu=1}^N \sum_{\beta=\mu+1}^N \mathbf{E}_{\mu} e^{-i\omega_{\beta} t} d_{\mu\beta}^* \quad (5.13)$$

$$= \sum_{\mu=1}^N \sum_{\alpha=\mu+1}^N \mathbf{E}_{\alpha} e^{-i\omega_{\mu} t} d_{\mu\alpha} + \sum_{\mu=1}^N \sum_{\beta=1}^{\mu-1} \mathbf{E}_{\beta} e^{-i\omega_{\mu} t} d_{\beta\mu}^*, \quad (5.14)$$

which reduces the polarization of each mode to

$$\mathbf{P}_{\mu} = \frac{\gamma_{\perp}}{\underbrace{\omega_{\mu} - \omega_a + i\gamma_{\perp}}_{\Gamma_{\mu}}} \left( \mathbf{E}_{\mu} D_s + \sum_{\alpha=\mu+1}^N \mathbf{E}_{\alpha} d_{\mu\alpha} + \sum_{\alpha=1}^{\mu-1} \mathbf{E}_{\alpha} d_{\alpha\mu}^* \right). \quad (5.15)$$

Inserting the polarization back into the MB equation for the electric field, Eq. (3.1a), and into the equations for the inversion, Eqs. (5.9) and (5.10), yields the refined SALT equations which treat the beating in the inversion in a self-consistent manner. The set of refined equations is given by

$$\nabla \times \nabla \times \mathbf{E}_\mu - \left[ \varepsilon_c \mathbf{E}_\mu + \Gamma_\mu (D_s \mathbf{E}_\mu + \sum_{\alpha=\mu+1}^N \mathbf{E}_\alpha d_{\mu\alpha} + \sum_{\alpha=1}^{\mu-1} \mathbf{E}_\alpha d_{\alpha\mu}^*) \right] \omega_\mu^2 = 0, \quad (5.16)$$

$$d_{\mu\nu} = -\frac{1}{2} \frac{\gamma_{\parallel}}{\Delta_{\mu\nu} + i\gamma_{\parallel}} \left[ \Gamma_\nu^* \mathbf{E}_\mu (D_s \mathbf{E}_\nu^* + \sum_{\alpha=\nu+1}^N \mathbf{E}_\alpha^* d_{\nu\alpha}^* + \sum_{\alpha=1}^{\nu-1} \mathbf{E}_\alpha^* d_{\alpha\nu}) - \Gamma_\mu \mathbf{E}_\nu^* (D_s \mathbf{E}_\mu + \sum_{\alpha=\mu+1}^N \mathbf{E}_\alpha d_{\mu\alpha} + \sum_{\alpha=1}^{\mu-1} \mathbf{E}_\alpha d_{\alpha\mu}^*) \right], \quad (5.17)$$

$$D_s = \frac{D_0 - \sum_{\mu=1}^N \text{Im} \left[ \Gamma_\mu^* \mathbf{E}_\mu (\sum_{\alpha=\mu+1}^N \mathbf{E}_\alpha^* d_{\mu\alpha}^* + \sum_{\alpha=1}^{\mu-1} \mathbf{E}_\alpha^* d_{\alpha\mu}) \right]}{1 + \sum_{\mu=1}^N |\Gamma_\mu \mathbf{E}_\mu|^2}. \quad (5.18)$$

Similar to when solving the SALT equation, there are no assumptions made, a priori about the modal fields  $\mathbf{E}_\mu$ , the laser frequencies  $\omega_\mu$ , as well as the beating terms  $d_{\mu\nu}$ . In comparison to the SALT equations, this refined set of equations explicitly depends on the relaxation rate of the inversion  $\gamma_{\parallel}$ . In particular, the ratio  $\frac{\gamma_{\parallel}}{\Delta_{\mu\nu} + i\gamma_{\parallel}}$  determines the overall amplitude of the beating terms relative to the modes  $\mathbf{E}_\mu$  and in the limit of  $d_{\mu\nu} \rightarrow 0$  the original SALT equations are recovered.

Whereas the original SALT solutions are invariant with respect to the global phase of each mode, this is no longer the case here. Instead, the phase of each mode is coupled to every other mode via the beating terms  $d_{\mu\nu}$ .

## Exceptional points above the laser threshold

So far we have only discussed exceptional points in laser systems that have been designed such that the EP occurs below the laser threshold. In this chapter, we extend the discussion of EPs to laser systems where the EP actually occurs above the threshold.

Such a scenario entails several further questions. One issue, which has been investigated only by using linear models for describing a laser system [14, 75] involves the linewidth of the emitted laser emission. One quantity, which can significantly increase the linewidth, is the Petermann factor. It stems from the non-power-orthogonal nature of the resonator modes of a laser system due to the outcoupling [84]. In particular the Petermann factor predicts that exactly at the EP the linewidth should diverge.

Furthermore, since both modes coalesce directly at the EP, this poses a further question with regard to the stability of the laser close to the EP. Since close to the EP the stationary inversion approximation cannot be fulfilled the stability of the system needs to be investigated as well. For the latter case we apply the linear stability theory developed in the previous chapter.

The chapter is arranged as follows: First we are going to review how the

linewidth of laser modes as obtained with SALT can be calculated. Next, we are going to apply both the linewidth calculation and the stability analysis to an adapted version of the coupled cavity system of section 4.1 which comes significantly close to an EP above threshold.

## 6.1 Linewidth calculation in SALT

The first account on the linewidth of a laser mode has been given by Schawlow and Townes in their seminal paper [85] in which they derived the following equation for the linewidth

$$\delta\omega_{\text{ST}} = \frac{\hbar\omega_0\gamma_c^2}{2P} \quad (6.1)$$

Here,  $\omega_0$  is the frequency of the laser,  $\gamma_c$  the decay rate of the passive cavity and  $P$  the output power. Since the publication of this paper several correction factors to this linewidth formula have been found: The incomplete inversion factor, the Petermann factor, the  $\alpha$  factor, and the bad cavity factor [52, 86–88]. The incomplete inversion factor is due to an incomplete inversion of the population of the upper and lower level of the lasing transition. The  $\alpha$  factor, which for semiconductor lasers is also known as the Henry  $\alpha$  factor, is due to a coupling of amplitude fluctuations to the phase dynamics. The bad cavity factor arises in low-Q cavities where the passive cavity resonances are of comparable order to the gain width  $\gamma_{\perp}$  such that strong dispersion effects can occur when the laser is pumped to threshold. For a complete account on these corrections see, e.g., [52, 88]. For the particular case, which we are considering in this thesis, i.e., when the laser system is close to an EP, the Petermann factor  $K$  is of particular importance. Whereas the original linewidth formula, (6.1), was derived for closed cavities, the Petermann factor takes into account the openness of the cavity and is a measure of the non-orthogonality of the modes and is given by

$$K = \left| \frac{\int dx |E(x)|^2}{\int dx E(x)^2} \right|^2. \quad (6.2)$$

Since at the EP the corresponding eigenmode becomes self-orthogonal the Petermann factor would diverge.

Semiclassical laser theory and therefore SALT as described in chapter 3 does not include noise due to quantum fluctuations and hence the intrinsic linewidth is not captured. Recently, however, two approaches for calculating the linewidth based on SALT have been developed and enable the calculation of the linewidth in a post-processing step. In the first approach [86, 87], Chong and Stone used input-output theory together with a scattering matrix formalism of the quantum fluctuations to calculate the linewidth of a SALT mode. This approach, in contrast to earlier theories, works for arbitrary shaped geometries and can fully take into account the nonlinear terms due to spatial hole burning. However, it only takes into account the Petermann factor and the bad cavity factor. In [88], Pick et al. have derived a similar linewidth formula for SALT by coupling the full Maxwell-Bloch equations to an atomic gain medium combined with random currents whose statistics are described by the fluctuation-dissipation theorem. Here, all correction factors are included and it is shown that all correction factors are intertwined with each other and often can not be calculated separately. Recently, this linewidth formula has been successfully quantitatively compared to a full time-dependent model [52].

Both derivations of the linewidth are based on the expansion of the Green's function in eigenmodes. Hence, these formulas are not valid when a mode is exactly at an EP since the eigenvectors do not form a complete basis of the space such that the Green's function expansion is no longer valid [89]. We can thus only calculate the linewidth of a laser mode that passes in the vicinity of an EP without, however, reaching it exactly.

Since we are primarily interested in the linewidth enhancement due to the Petermann factor we will use the formula given in [87] for calculating the generalized decay rate  $\gamma_L$ . This generalized decay rate replaces  $\gamma_c$  in the Schawlow-Townes formula of Eq. (6.1) and is given by

$$\gamma_L = \frac{\int_C d\mathbf{x} \operatorname{Im}[\varepsilon(\mathbf{x}, \omega_\mu) \omega_\mu^2] |\mathbf{E}_\mu^2|}{|\frac{ib^T b}{2} + \int_C d\mathbf{x} [\omega \varepsilon(\mathbf{x}, \omega) + \frac{\omega^2}{2} \frac{d\varepsilon}{d\omega}]_{\omega_\mu} \mathbf{E}_\mu^2|}. \quad (6.3)$$

Here,  $\varepsilon(\mathbf{x})$  is the full nonlinear electric permittivity as given in Eq. (3.15), and  $\frac{d\varepsilon}{d\omega}$  is the derivative of the electric permittivity with respect to the frequency

dependence in  $\Gamma(\omega) = \frac{\gamma_{\perp}}{\omega - \omega_a + i\gamma_{\perp}}$ . The integrals are performed within a domain  $C$  surrounding the laser cavity. The coefficients  $b$  are the expansion coefficients for expanding the electric field  $\mathbf{E}_{\mu}$  in terms of outgoing eigenmodes by connecting it to the interior solution  $\mathbf{E}_{\mu}$ , as determined by SALT, at the interface  $\delta C$ .

## 6.2 Stability close to an exceptional point

In order to steer the coupled laser system, which we have studied in section 4.1, closer to an EP above threshold, we slightly modify the parameters of the system. For this we will increase the maximum pump strength applied to each of the cavities from 1.2 to 1.6. Furthermore, we shift the center of the gain curve to  $\omega_a \tilde{L} = 9.49$  to get significantly close to an EP.

In the left column of Fig. 6.1 we show the traditional SALT solution for this laser configuration, encompassing, from top to bottom, the power output of the laser, the mode frequencies, as well as a stability diagram. Here, a clear signature of an EP can be observed at a pump parameter of 1.67 when considering the mode frequencies. First, the active mode (red curve) approaches the EP without any significant alteration of its frequency. At the EP a second mode (blue curve) becomes active and the frequencies of the two modes now rapidly diverge from each other. For the power output of this system we surprisingly observe a very different behavior compared to the system with the EP below threshold. Instead of a drop we observe a continuous rise of the total power output! Furthermore, when the second mode becomes active after the system has passed the EP, we see an almost instantaneous equilibration of the power emitted from each mode which is expected due to the coalescence of the two modes at the EP. Hence, the modes are almost identical when the second mode starts lasing.

In the bottom figure, the stability diagram of this two-mode configuration is shown, which depicts the dependence of the stability on the relaxation rate of the inversion  $\gamma_{\parallel}$  and the pump parameter  $d$ . For realistic values of  $\gamma_{\parallel} \approx 10^{-3}$  [56], we observe that the system becomes unstable close to the EP at  $d \approx 1.67$  as



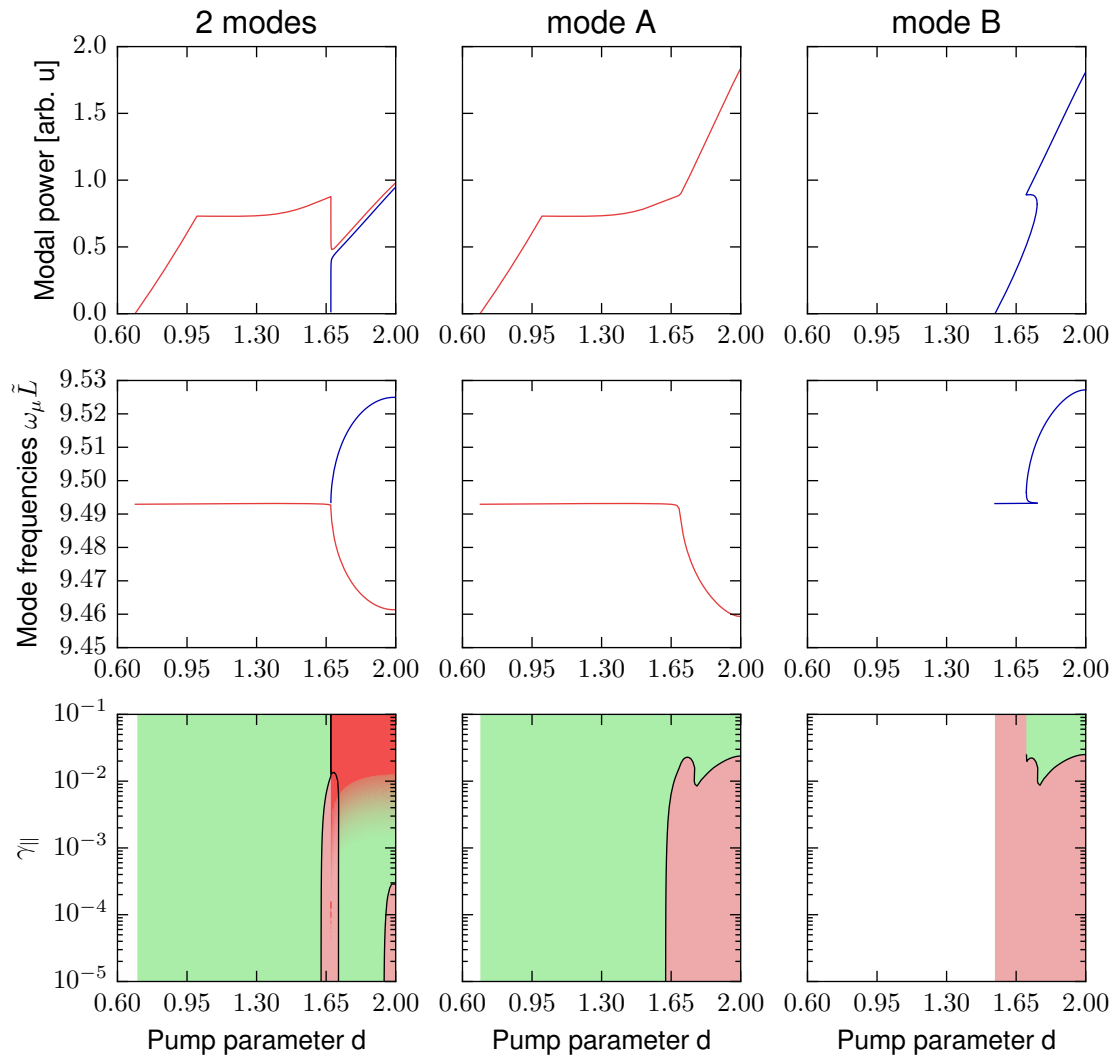


**Figure 6.1:** Modal power (upper row), mode frequencies (center row), and linear stability diagram for three different SALT solutions of a 1D coupled cavity laser featuring an EP above the laser threshold. The first column shows the solution as obtained from a normal SALT calculation, which at the EP, splits into two modes. In addition, the single-mode solutions, mode *A* and mode *B* exist as well. However, these solutions are only stable for large values of the relaxation rate  $\gamma_{||}$ .

indicated by the bright red shading. Hence, the continuous rise of the power output for this particular solution cannot be observed in an experiment as the mode is not stable. Therefore, even for an EP above threshold we should be able to observe that the laser output is no longer multi-periodic and hence the spectrum should change significantly.

Beyond the EP, when two modes are lasing, one has to consider the linear stability analysis carefully. Since its derivation involved the stationary inversion approximation, it is not possible to detect multi-mode instabilities that are due to the beating of the modes. Hence, we have to exclude any parameter region where  $\gamma_{\parallel} \not\ll |\omega_{\mu} - \omega_{\nu}|$ . We have marked this region in the linear stability analysis by a dark red shade. In addition the stability analysis reveals an instability of the system at a pump parameter of  $d = 2.0$  for small values of  $\gamma_{\parallel}$ . However, this instability is spurious and the system is in fact stable at this point. This failure of the linear stability analysis can be attributed to the stationary inversion approximation used in the derivation.

Note that this two-mode solution is not the only solution of the SALT for this particular system. When sweeping the pump parameter  $d$  through the EP one can simply continue tracking the single mode without activating the second mode. The corresponding solution of the SALT is shown in the middle column of Fig. 6.1. Similar to the two-mode solution a continuous increase of the output power is observed. However, in order for this mode to be stable a very large relaxation rate,  $\gamma_{\parallel}$ , of the inversion is required. This mode has the exceptional property that it can be even stable at the EP. However, the corresponding relaxation rate of  $\gamma_{\parallel}$  is not available for semiconductor lasers [90]. Note, that the frequency behavior of this mode is very similar to one mode of the solution in the left column. Similarly we find the second mode, which features a frequency shift towards a higher frequency at the EP, to be a single-mode solution of the SALT equation as well. However, it only becomes stable beyond the EP.

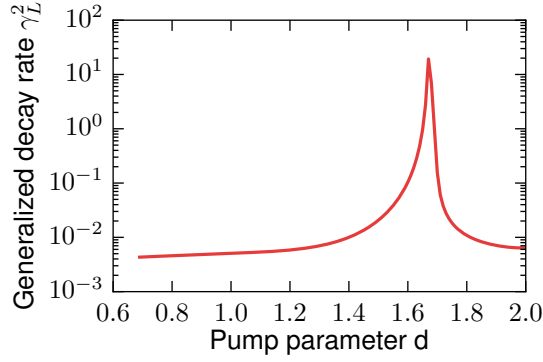


**Figure 6.2:** Linewidth broadening as given by the generalized decay rate  $\gamma_L$ . Close to the EP at  $d \approx 1.67$  a broadening of the linewidth by sixth orders of magnitude can be observed.

### 6.3 Laser linewidth close to an EP

Since, the two-mode solution is not stable at the EP, we will only evaluate the linewidth of mode  $A$ . A SALT solution, in general, is independent of the transition dipole moment  $g$  of the gain medium, which only appears as a scaling factor for converting the field of a mode to SI units. The linewidth, however, directly depends on this parameter. Since we are primarily interested in the relative linewidth change close to the EP, we will instead only look at the generalized decay rate  $\gamma_L$  as given by Eq. (6.3). From the Schawlow-Townes formula, where  $\gamma_L$  replaces the passive cavity decay rate  $\gamma_c$ , we find that the linewidth depends on the square of  $\gamma_L$ .

The generalized decay rate for mode  $A$  is shown in Fig. 6.2. Here, we observe an increase of the generalized decay rate by two orders of magnitude close to the EP and hence an increase of four orders of magnitude of the linewidth. This qualitatively agrees with the prediction of the Petermann factor [14, 75]. Note, that even when the EP is reached exactly, the linewidth would not be infinite as this case has not been considered in the corresponding derivation of the linewidth formula [89]. However, preliminary results, which use an adaptation of the linewidth formula found in [88], show that the linewidth indeed stays finite [89].

## EPs in transmission experiments and chirality

When inducing an EP above threshold in a coupled microdisk system, the typical feature of an avoided crossing in the complex eigenvalues is strongly modified due to the nonlinear spatial-hole burning interactions. In order to be able to study this eigenvalue progression including the EP in a linear system one can, however, study a system below the laser threshold. For this the system has to be probed by an external signal by coupling two wave guides to it and measuring the transmission through the waveguides. The simplest theoretical description of these systems is given by the temporal coupled mode theory (TCMT) [91–93], which has already been used for the toy model in chapter 2. The results from the TCMT are compared to full numerical calculations.

In addition to the system of two coupled microdisks where an EP is induced by carefully adjusting gain and loss in the individual disks we will investigate a further system featuring an EP consisting of a single microdisk. In this system, two degenerate whispering gallery modes of the disk are perturbed by two nanoscatterers which are positioned very close to the disk, i.e., the gap between each of the scatterers and the disk is less than the wavelength corresponding to the eigenfrequency of the system. Here, careful positioning of the

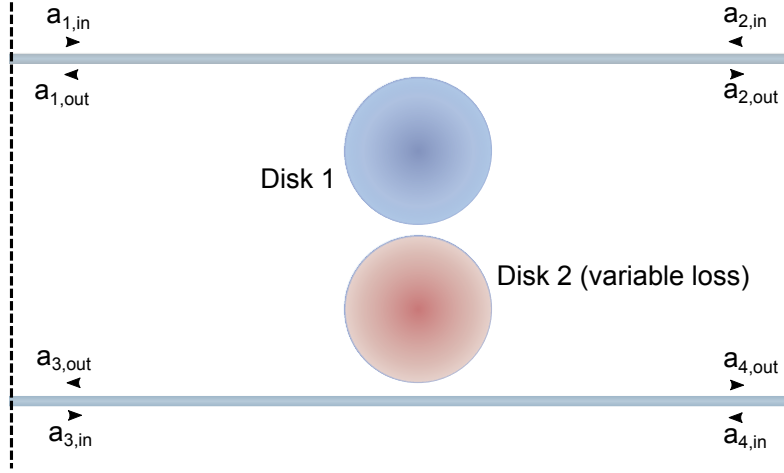


**Figure 7.1:** Sketch of the setup for measuring the EP transition via a transmission setup

two nanoscatterers can lead to the collapse of the two originally left- and right-traveling whispering gallery modes into a mode traveling into only one or the other direction. This collapse can again be associated with an EP.

## 7.1 EPs in coupled microdisks

First, we study the appearance of an EP in a photonic molecule coupled to two waveguides. In comparison to the previous chapters, here, an EP is only investigated below the laser threshold by varying the loss applied to one of the resonators. The setup of the system is depicted in Fig. 7.1. The disks each have a radius of  $0.41 \tilde{L}$  and feature an index of refraction of  $n = 1.444$ . The gap between the disks is  $d = 0.125 \tilde{L}$ . The waveguides have a width of  $0.0125 \tilde{L}$  and are situated at a distance of  $0.085 \tilde{L}$  from each of the disks, respectively. They feature the same index of refraction as the two disks.

When isolated, each of the disks has a resonance at  $\Omega_{1,2} \approx 79.7291617 - 0.0001695283i$ . These individual resonances will be coupled to each other and an EP is induced by varying the loss within the second resonator.

### 7.1.1 TCMT model

For a simple physical description, we extend the coupled mode model of chapter 2 to include the coupling to the two adiabatically coupled waveguides. Following Ref. [93], the TCMT gives the following equations for describing the system

$$i \frac{\partial}{\partial t} \begin{pmatrix} \Psi_1 \\ \Psi_2 \end{pmatrix} = \underbrace{\begin{pmatrix} \Omega_1 - i\frac{\kappa}{2} & \gamma \\ \gamma & \Omega_2 - i\frac{\kappa}{2} - i\eta \end{pmatrix}}_{H_{\text{pm}}} \begin{pmatrix} \Psi_1 \\ \Psi_2 \end{pmatrix} + i\sqrt{\kappa} \begin{pmatrix} a_{1,\text{in}} \\ a_{3,\text{in}} \end{pmatrix}, \quad (7.1)$$

$$a_{2,\text{out}} = -a_{1,\text{in}} + \sqrt{\kappa}\Psi_1 \quad (7.2)$$

$$a_{4,\text{out}} = -a_{3,\text{in}} + \sqrt{\kappa}\Psi_2 \quad (7.3)$$

where  $\Psi_1$  ( $\Psi_2$ ) corresponds the clockwise (counter-clockwise) traveling whispering gallery modes in disk 1 (2). Here,  $\Omega_1$  and  $\Omega_2$  are the eigenfrequencies of the corresponding microdisks. Their imaginary part may be non-zero corresponding to losses due to absorption or leakage of the mode into the environment. The loss due to coupling with the waveguide is given by  $\kappa$ , which describes the coupling strength between waveguide and microdisk.  $\gamma$  corresponds to the coupling strength between the microdisks. For this passive system the loss within the second cavity may be tuned by the parameter  $\eta$ . A fully equivalent independent set of equations can be defined for the whispering gallery modes traveling into the opposite direction by coupling into the system via ports 2 and 4.

When light is injected at one of the ports with a fixed frequency  $\omega_e$ , the electric field must oscillate everywhere at the same frequency due to the linearity of Maxwell's equations. Plugging  $\Psi_{1,2}(t) = e^{-i\omega_e t}\Psi_{1,2}$  into Eq. (7.1) and assuming only input from port 1, i.e.  $a_{3,\text{in}} = 0$ , we can solve for the field amplitudes  $\Psi_{1,2}$

$$\Psi_1 = \frac{i\sqrt{\kappa}(\omega_e - \Omega_2 + i\frac{\kappa}{2} + i\eta)}{(\omega_e - \Omega_1 + i\frac{\kappa}{2})(\omega_e - \Omega_2 + i\frac{\kappa}{2} + i\eta) - \gamma^2} a_{1,\text{in}} \quad (7.4)$$

$$\Psi_2 = \frac{i\sqrt{\kappa}\gamma}{(\omega_e - \Omega_1 + i\frac{\kappa}{2})(\omega_e - \Omega_2 + i\frac{\kappa}{2} + i\eta) - \gamma^2} a_{1,\text{in}}, \quad (7.5)$$

and from Eqs. (7.2) and (7.3) the output amplitudes  $a_{2,\text{out}}$  and  $a_{4,\text{out}}$  are easily obtained.

### 7.1.2 Numerics

In order to verify the TCMT model we compare the results to full numerical calculations obtained with the finite element method as implemented by netgen/ngsolve [94,95]. In these two-dimensional simulations we assume that the light is TM-polarized and only treat the out-of-plane component of the electric field  $E_z$ . The central equation used in the simulations is the inhomogeneous Helmholtz Eq.

$$[\nabla^2 + n(x)^2\omega_e^2]E_z = f_m(x, y), \quad (7.6)$$

where  $n(x)$  is the index of refraction of the respective materials and  $\omega_e$  the frequency of the injected light. The source term  $f_m(x, y)$  can be used to inject light into the system at any port  $m$  and is given by

$$f(x, y) = \delta(x - x_m) \begin{cases} A \cos(\sqrt{n_{\text{wg}}^2\omega_e^2 - \beta_x^2}(y - y_{\text{wg}})) & y \in \text{WG} \\ B \exp(\pm\sqrt{\omega_e^2 - \beta_x^2}y) & y \notin \text{WG}, \end{cases} \quad (7.7)$$

which perfectly couples into the fundamental mode of the corresponding dielectric waveguide (WG). Here,  $n_{\text{wg}}$  is the index of refraction of the wave guide and  $y_{\text{wg}}$  corresponds to the y-coordinate of the center of the waveguide. The propagation constant  $\beta_x$ , as well as one of the constants,  $A$  and  $B$ , are defined through matching conditions at the dielectric waveguide interface [55]. The other constant then determines the overall amplitude of the source term.

The whole setup is surrounded by a perfectly matched layer as described in section 3.6.2 to avoid any back reflections from the boundary of the finite computational domain. The amplitudes  $a_{1 \rightarrow 4, \{in, out\}}$  of the incoming and outgoing waveguide modes are extracted from the numerical solution to Eq. (7.6) by projecting it onto the corresponding modes  $f_{\{1 \rightarrow 4\}}(x, y)e^{\pm i\beta_x x}$ .

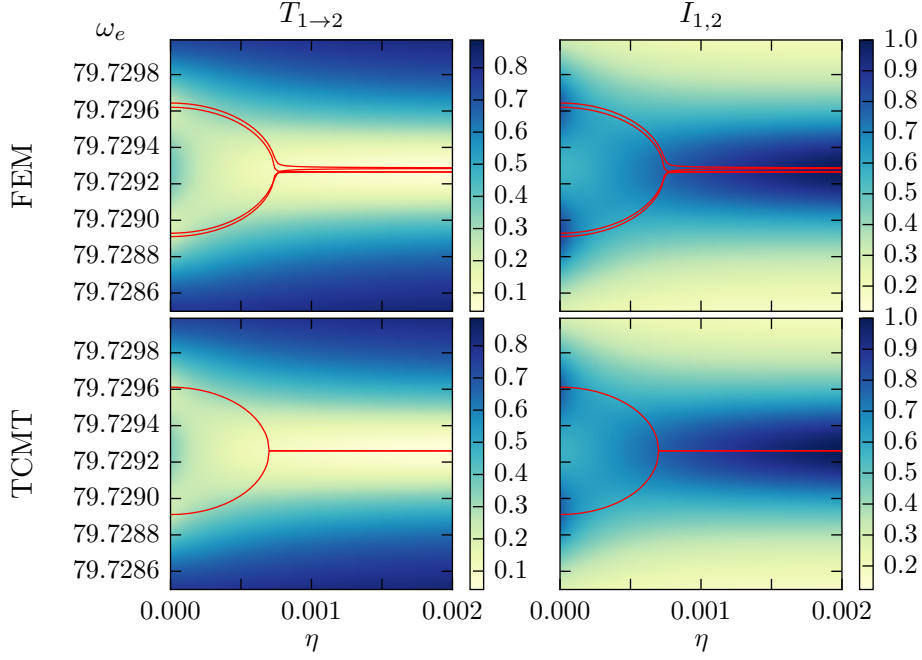


**Figure 7.2:** (left panels) Transmission spectrum from port 1 to port 2 and (right panels) spectrum of the sum of the mode intensities within both disks with respect to the loss parameter  $\eta$ . The upper panels show the results obtained from the finite element simulations, the lower panels the results from coupled mode theory. The red lines show the eigenvalues of the resonances for the respective methods.

In order to map the loss parameter  $\eta$  from the TCMT model to the index of refraction  $\tilde{n}_2$  of the second disk we use the relation  $\tilde{n}_2 \Omega_2 \approx n_2 (\Omega_2 - i\eta)$  and find

$$\tilde{n}_2 = \text{Re}(n_2) \left( 1 + i \frac{\eta}{\text{Re}(\Omega_2)} \right), \quad (7.8)$$

which is used in the numerical calculations.

### 7.1.3 Discussion

In order to determine the effect that the EP has on the system we look at two quantities in particular: The transmission from port 1 to port 2,  $T_{1 \rightarrow 2} = \left| \frac{a_{2,\text{out}}}{a_{1,\text{in}}} \right|^2$ , and the sum of the light intensities within both resonators,  $I_{1+2} = \int_{\mathcal{C}_1 \cup \mathcal{C}_2} |E_z|^2 d\vec{x}$ . The values for the coupling strengths  $\gamma$  and  $\kappa$  in the TCMT model have been



determined from the finite element calculations and are 0.00168 and 0.00035, respectively. The corresponding results are shown in Fig. 7.2 both for the numerical simulations using the finite element method, as well as for the coupled mode theory and the results of both methods show an extremely good agreement with each other. The effect of the EP can be observed both in the transmission  $T_{1 \rightarrow 2}$  spectrum, as well as in the sum of the intensities  $I_{1,2}$ . However, due to the relatively strong coupling between the resonators and the wave guides in comparison to the coupling between the disks, the width of the resonances are relatively broad, such that the exact EP is not clearly visible.

From these results we can draw the conclusion that the occurrence of the EP can easily be verified with transmission experiments and that for this particular system the TCMT model works remarkably well. Furthermore, the EP manifests itself not only in the transmission spectra, but as well in the field intensities inside the two resonators. Hence, the EP can also be observed in physical processes which directly dependent on the intensity of light within the cavities. One such process is for example Raman amplification such that the effect of the EP in the injected signal can be detected in the Raman laser output of such a coupled system as has experimentally been accomplished (c.f. chapter 8).

## 7.2 Chirality

So far we have used EPs in order to observe a drastic change of the behavior of a system of coupled resonators when passing an EP. However, another option for exploiting an EP is to make use of the fact that two or more eigenmodes of the system collapse into a single mode at the EP. One such property is the chirality. For a single microdisk resonator the two degenerate whispering gallery modes travel into opposite directions. As has already been shown by Jan Wiersig in references [10,96] these two originally degenerate modes can be perturbed with the help of two nanoscatterers which are placed in close vicinity of such a microdisk. By carefully choosing the position of the nanoscatterers it is thus possible to make the two whispering gallery modes collapse into a single mode

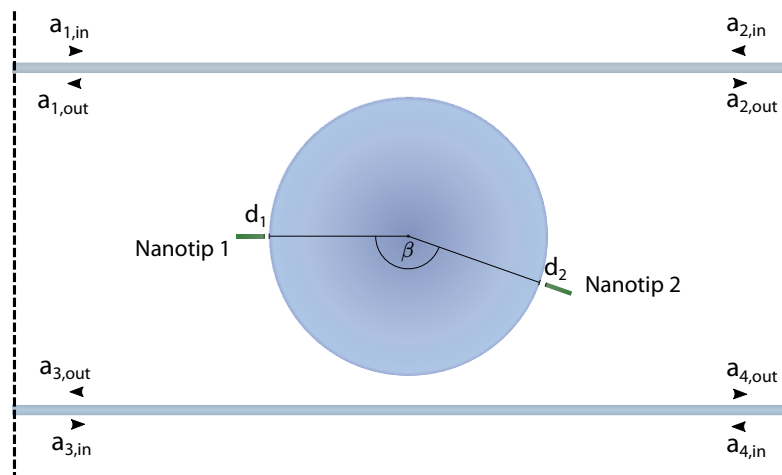


**Figure 7.3:** Sketch of the setup used to explore EPs associated with the chirality of a resonator. Two dielectric nanotips are used as scatterers to manipulate the chirality. They are positioned on opposite sides of the microdisk and are positioned at variable distances of  $d_1$  ( $d_2$ ) away from the microdisk. The system is furthermore coupled to two wave guides in order to be able to probe the system.

with a definitive chirality. This collapse indeed occurs at an EP. In this section we are going to investigate how such EPs, which are induced by asymmetric scattering between the two modes, can be probed in a transmission setup by attaching two waveguides to the microdisk.

Here, we will use a single microdisk, of which all resonances featuring a non-zero angular momentum are degenerate corresponding to counter-clockwise and clockwise traveling modes,  $\Psi_{CCW}$  and  $\Psi_{CW}$  respectively. By placing a single scatterer, i.e. nanotip 1 in Fig. 7.3, close to the resonator, both modes couple to each other in a symmetric fashion, similar to the case of the clockwise and counter-clockwise running waves in the two microdisks discussed above. However, by placing two dissimilar scatterers right next to the microdisk, an asymmetric coupling between the two modes is achieved. In the most extreme case, this asymmetric scattering yields that only either the CCW or the CW mode remains an eigenstate of the system. This collapse of the eigenspace can then be associated with an EP.

In the following we will consider the system as shown in Fig. 7.3. Here, two

dielectric nanotips are used as the scatterers, the first of which is kept fixed at the same position. In order to probe the system in the vicinity of an EP the position of the second nanotip is changed both with respect to its distance from the resonator as well as with respect to the angle between the two nanotips.

### 7.2.1 TCMT model

The simplest model to describe this setup is given by the following equations using the TCMT [92,93]

$$i \frac{\partial}{\partial t} \begin{pmatrix} \Psi_{\text{CCW}} \\ \Psi_{\text{CW}} \end{pmatrix} = \underbrace{\begin{pmatrix} \Omega_C - i\kappa & A \\ B & \Omega_C - i\kappa \end{pmatrix}}_{H_{\text{chiral}}} \begin{pmatrix} \Psi_{\text{CCW}} \\ \Psi_{\text{CW}} \end{pmatrix} + i\sqrt{\kappa} \begin{pmatrix} a_{1,\text{in}} + a_{4,\text{in}} \\ a_{2,\text{in}} + a_{3,\text{in}} \end{pmatrix}, \quad (7.9)$$

$$a_{\{1,4\},\text{out}} = -a_{\{2,3\},\text{in}} + \sqrt{\kappa} \Psi_{\text{CCW}} \quad (7.10)$$

$$a_{\{2,3\},\text{out}} = -a_{\{1,4\},\text{in}} + \sqrt{\kappa} \Psi_{\text{CW}}, \quad (7.11)$$

which allows for injecting light at any input port. Similar to the case of the coupled microdisks,  $\kappa$  corresponds to the coupling strength between cavity and wave guide. The (complex) coefficient  $A$  ( $B$ ) determines the backscattering strength from the CW (CCW) to the CCW (CW) mode. The coefficients  $\Omega_C$ ,  $A$ , and  $B$  are calculated through the positions of the two nano-tips and given by [10]

$$\Omega_C = \Omega_1 + V_1 + U_1 + V_2 + U_2 \quad (7.12)$$

$$A = V_1 - U_1 + (V_2 - U_2)e^{-2im\beta} \quad (7.13)$$

$$B = V_1 - U_1 + (V_2 - U_2)e^{+2im\beta}, \quad (7.14)$$

where  $\Omega_1$  is the complex eigenfrequency of a degenerate eigenpair of the isolated resonator.  $2V_1$ , and  $2U_1$  are the (complex) frequency shifts that are induced on the eigenfrequency  $\Omega_1$  by the perturbation through nano-tip 1.  $V_2$ , and  $U_2$  are similarly defined for nano-tip 2. Note, that due to the cylindrical symmetry of the resonator, these parameters depend only on the distance between the nanotip and the resonator. The angle  $\beta$  between the two nano-tips occur explicitly

in the definition of the coefficients  $A$  and  $B$  together with the angular momentum number  $m$  by which the mode corresponding to  $\Omega_1$  can be identified with. In the following we will calculate the coefficients  $V_1, U_1, V_2,$  and  $U_2$  from finite element calculations.

The eigenvalues of the effective non-Hermitian Hamiltonian  $H_{\text{chiral}}$  are given by

$$\Omega_{\pm} = \Omega_C - i\kappa \pm \sqrt{AB}, \quad (7.15)$$

and the corresponding (non-normalized) eigenvectors by

$$\Psi_{\pm} = \begin{pmatrix} \sqrt{A} \\ \pm\sqrt{B} \end{pmatrix}. \quad (7.16)$$

The eigenvectors become colinear when either of the backscattering coefficients  $A$  or  $B$  becomes 0. Therefore in both cases we encounter an EP. When  $A = 0$  only backscattering from the CCW to the CW mode occurs, but not in the other direction and for  $B = 0$  the exact opposite holds. We can quantify the asymmetry in backscattering using the intrinsic chirality of the resonator, which we can define as

$$\alpha = \frac{|A| - |B|}{|A| + |B|}. \quad (7.17)$$

When  $\alpha = 0$ , i.e. for symmetric scattering or when the modes are not coupled, neither direction is preferred. For  $\alpha \neq 0$ , both eigenvectors have a dominant component. For  $|A| \ll |B|$  ( $|A| \gg |B|$ ), the counter-clockwise (clockwise) mode dominates over the other. If either  $A$  or  $B$  is zero then the points of maximum internal chirality, i.e.  $\alpha = \pm 1$ , are reached, each of which corresponds to an EP.

In the following we want to determine the chirality  $\alpha$  both for the case when the system is lasing close above threshold, as well as for the situation, when the passive system is probed via the coupled wave guides.

For the case when the system is lasing, it is sufficient to consider how the eigenstates (Eq. (7.16)) couple to the wave guides, since the incoming wave guide amplitudes are zero. Note, that for lasing an additional (complex) gain term needs to be added to the diagonal entries of  $H_{\text{chiral}}$ . However, as this term affects both modes equivalently strongly, it can be neglected for describing the

chirality of the resonator. In order to avoid tedious SALT calculations for every scattering configuration, we only assume that the laser is close above threshold such that the QB-states already yield a good approximation to the actual laser modes. Furthermore, we naturally assume that the two modes also correspond to the first laser modes in the system.

The outgoing amplitudes for this model are then given by

$$a_{\{1,4\},out} = \sqrt{\kappa}\Psi_{CCW} = \sqrt{\kappa A} \quad (7.18)$$

$$a_{\{2,3\},out} = \sqrt{\kappa}\Psi_{CW} = \sqrt{\kappa B}, \quad (7.19)$$

such that the chirality for the lasing system can be obtained from the outgoing amplitudes as

$$\alpha_{\text{lasing}} = \frac{|a_{CCW,out}|^2 - |a_{CW,out}|^2}{|a_{CCW,out}|^2 + |a_{CW,out}|^2}, \quad (7.20)$$

where  $a_{CCW,out}$  ( $a_{CW,out}$ ) stands for any outgoing mode amplitude to which the CCW (CW) traveling mode couples to, i.e., either port 1 (2) or port 4 (3). The same quantity has already been used in [97] under the name ‘directionality’.

When probing the passive system via a transmission experiment, the chirality needs to be modified as the system is probed with an external source. From Eqs. (7.9) we find that for input from port 1 or port 4, which both couple into the CW traveling mode, we obtain the following outgoing waveguide amplitudes

$$a_{CW,out} = \frac{i\kappa(\omega_e - \Omega_C + i\kappa)}{(\omega_e - \Omega_C + i\kappa)^2 - AB}(a_{1,in} + a_{4,in}) \quad (7.21)$$

$$a_{CCW,out} = \frac{i\kappa A}{(\omega_e - \Omega_C + i\kappa)^2 - AB}(a_{1,in} + a_{4,in}). \quad (7.22)$$

Note, that when coupling into the CW traveling mode, we can only easily find one of the EPs of the system, namely the one where  $A = 0$ , in which case there is no backscattering from the CW to the CCW traveling mode. When we couple into the system via port 2 or 3, i.e., to a CCW traveling mode, we find

$$a_{CW,out} = \frac{i\kappa B}{(\omega_e - \Omega_C + i\kappa)^2 - AB}(a_{2,in} + a_{3,in}) \quad (7.23)$$

$$a_{CCW,out} = \frac{i\kappa(\omega_e - \Omega_C + i\kappa)}{(\omega_e - \Omega_C + i\kappa)^2 - AB}(a_{2,in} + a_{3,in}). \quad (7.24)$$

Combining Eqs. (7.22) and (7.23), the chirality  $\alpha$  can in general be retrieved in a transmission experiment by combining the results from two separate measurements where the backscattering from the CW to the CCW traveling mode and vice versa are probed separately. This yields the general expression

$$\alpha_{\text{scattering}} = \frac{|a_{\text{CCW,out}}^{\text{CW,in}}| - |a_{\text{CW,out}}^{\text{CCW,in}}|}{|a_{\text{CCW,out}}^{\text{CW,in}}| + |a_{\text{CW,out}}^{\text{CCW,in}}|}, \quad (7.25)$$

where we have denoted the different input channels via the superscripts. In particular we will look at two different options for measuring the chirality when injecting light at ports 1 and 2. First, by measuring the transmission through the system and measuring the transmitted light at ports 3 and 4. This scenario has the advantage that it can be easily realized in an experiment. Second, by measuring the reflection amplitudes at ports 1 and 2.

$$\alpha_{\text{transmission}} = \frac{|a_{4,\text{out}}^{1,\text{in}}| - |a_{3,\text{out}}^{2,\text{in}}|}{|a_{4,\text{out}}^{1,\text{in}}| + |a_{3,\text{out}}^{2,\text{in}}|}, \quad (7.26)$$

$$\alpha_{\text{reflection}} = \frac{|a_{1,\text{out}}^{1,\text{in}}| - |a_{2,\text{out}}^{2,\text{in}}|}{|a_{1,\text{out}}^{1,\text{in}}| + |a_{2,\text{out}}^{2,\text{in}}|}. \quad (7.27)$$

In the TCMT model all definitions, Eqs. (7.26), (7.27), and (7.20), should yield the same results. However, there are effects, which are not included within the TCMT such as backscattering at the wave guide ports. These additional perturbations can strongly affect the chirality as defined by the nanotips. Hence, when the results from all these different definitions agree well with each other we can validate that the assumptions of the TCMT model.

## 7.2.2 Numerical results

In order to compare the two different chirality formulas defined in Eqs. (7.26) and (7.20) we have performed numerical calculations similar to the photonic molecule calculations in 7.1.2. The geometry of the system is shown in Fig. 7.3. The parameters for the waveguides and scatterers have been chosen such that the scatterers perturb the eigenvalues of the system much stronger than the waveguides coupled to the resonator. The microdisk resonator has a radius

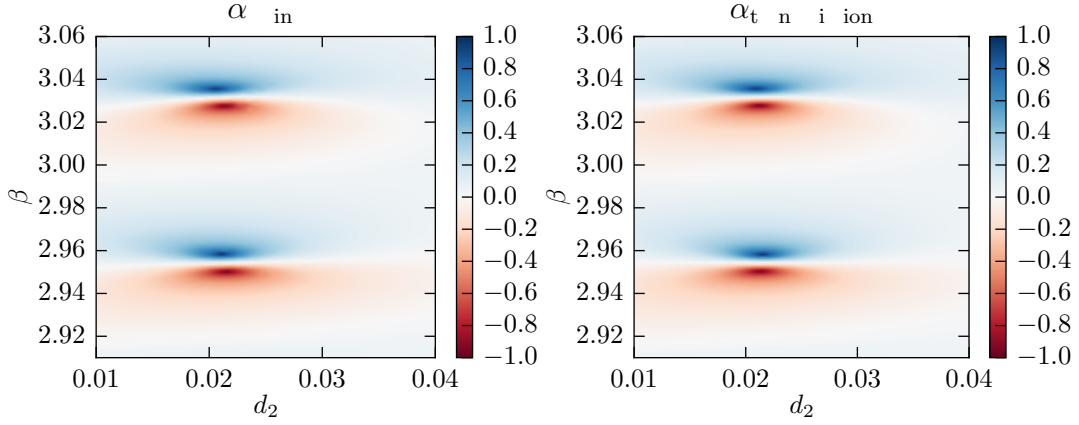


**Figure 7.4:** Comparison of the chirality obtained through a full numerical eigenvalue calculation by Eq. (7.20) and through a full numerical transmission calculation by Eq. (7.26). The dependence of the chirality is plotted with respect to the position of the second nano-tip given by both the angle between the scatterers,  $\beta$ , as well as the gap between the scatterer and the microdisk,  $d_2$ . Both formulas yield very similar values for the chirality corroborating the validity of the TCMT model.

of  $R = 0.41\tilde{L}$ . The width of the waveguides is  $0.0125\tilde{L}$  and the gap between the waveguides and the resonator is  $0.085\tilde{L}$ . The nanotips used as scatterers in the simulations are of rectangular shape and have a length of  $0.102\tilde{L}$ . Nano-tip 1 has a fixed position: It is situated at an angle of  $\pi/2$  with respect to the waveguides and the gap between the tip of the scatterer and the microdisk is  $0.02\tilde{L}$  and its width is  $0.0099\tilde{L}$ . Nano-tip 2 has a width of  $0.0079\tilde{L}$  and is situated on the opposite side of the disk. Its position is given by the angle  $\beta$  between the scatterers and the distance  $d_2$  from the resonator. In the calculations the angle  $\beta$  is varied between 2.91 and 3.06, and the distance  $d_2$  between 0.01 and 0.04. The waveguides, as well as the microdisk resonator have an effective refractive index of  $n = 1.444$ . If not stated otherwise the shown data use a frequency of  $\omega_e\tilde{L} = 79.728$ . The calculations are performed in the same way as described in section 7.1.2.

### 7.2.3 Discussion

In Fig. 7.4 we compare the chirality as determined from the eigenvalue calculations of the system with the chirality as determined from the transmission calculations. The chirality is obtained under variation of the two positional parameters ( $d_2, \beta$ ) of the second scatterer. We chose to vary two parameters in order to be able to exactly reach the EPs where the chirality features an absolute maximum, i.e.  $\alpha = \pm 1$ . In the parameter range as shown in Fig. 7.4 two pairs of EPs are depicted where each pair features two EPs of opposite chirality. The pattern of EP pairs is roughly repetitive when extending the scanned interval of angle  $\beta$  as long as the scatterer does not come close to one of the attached waveguides.

In the calculations we observe an excellent agreement between the two chirality definitions such that we can indeed assume that both methods yield a good estimate for the internal chirality of the whispering gallery modes induced by the presence of the two scatterers.

In a next step we explicitly compare the fully numerical results to the results from the TCMT model. For this, we calculate the parameters  $U_1, U_2, V_1,$  and  $V_2$  through separate eigenvalue calculations for each of the scatterers, where no waveguides are attached to the system, and use these to determine the coefficients  $A, B,$  and  $\Omega_C$ . The value for the coupling coefficient  $\kappa$  is determined as in section 7.1.2.

In Fig. 7.5a the chirality definitions of Eqs. (7.17), (7.20), (7.26), and (7.27) are compared to each other for the case that the distance of nanotip 2 is fixed at the same distance as nanotip 1, i.e.  $d_2 = 0.02$ . Here, we again observe an excellent agreement between the numerical calculations. For the TCMT model we find that it correctly predicts the angles at which the chirality becomes minimal/maximal, but the absolute values for the chirality differ by 50 percent. The reason for this is that the TCMT model does not include other scattering processes as, for example, between the resonator and the waveguide.

In Fig. 7.5b it is shown that the chirality also depends relatively strongly on the frequency  $\omega_e$  of the source emitter. The reason for this is that a change of



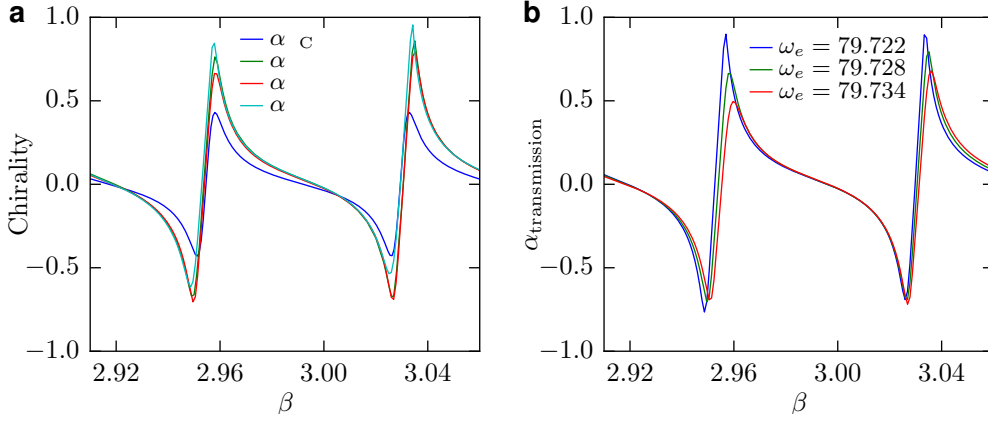


**Figure 7.5:** Comparison of the chirality definitions for  $\alpha_{\text{TCMT}}$ ,  $\alpha_{\text{lasing}}$ , and  $\alpha_{\text{transmission}}$ . In the calculations the nano-tip 2 has a fixed distance  $d_2 = 0.02$  from the resonator and the angle  $\beta$  is varied.

the wavelength results in a different ratio of the angle  $\beta$  and the wavelength, thereby shifting the chirality peaks. This also explains the slight differences of the transmission and lasing cases as observed in Fig. 7.4 since in the latter case the ‘probe’ frequency is fixed by the resonance frequencies.

The asymmetric backscattering, which results in the intriguing chirality behavior in Fig. 7.5, can also be observed by looking at the normalized backscattering intensity  $|\mathcal{B}_{\text{CCW}}|^2 = |a_{\text{ccw,out}}|^2 / |a_{\text{cw,in}}|^2$  from the CW to CCW traveling mode and the similarly defined  $|\mathcal{B}_{\text{CW}}|^2$ . From Eq. (7.20) follows that an EP with its absolute chirality maximum is reached when either of the backscattering intensities,  $|\mathcal{B}_{\text{CCW}}|^2$  or  $|\mathcal{B}_{\text{CW}}|^2$ , is zero. Hence, a chirality maximum (minimum) can be found by minimizing the backscattering intensity  $|\mathcal{B}_{\text{CCW}}|^2 (|\mathcal{B}_{\text{CW}}|^2)$ . The EPs corresponding to opposite chiralities occur at slightly different angles  $\beta$  which manifests itself by shifting the two backscattering intensity patterns  $|\mathcal{B}|^2$  with respect to the angle  $\beta$  as shown in Fig. 7.6. Here, the angles  $\beta$  at which the backscattering  $|\mathcal{B}|^2$  becomes minimal are indicated by dashed lines. In addition, both the results for the TCMT model and the numerical transmission calculations are plotted and show an excellent agreement although the intensities don’t match exactly as we have already shown for the comparison of the different chirality definitions above.

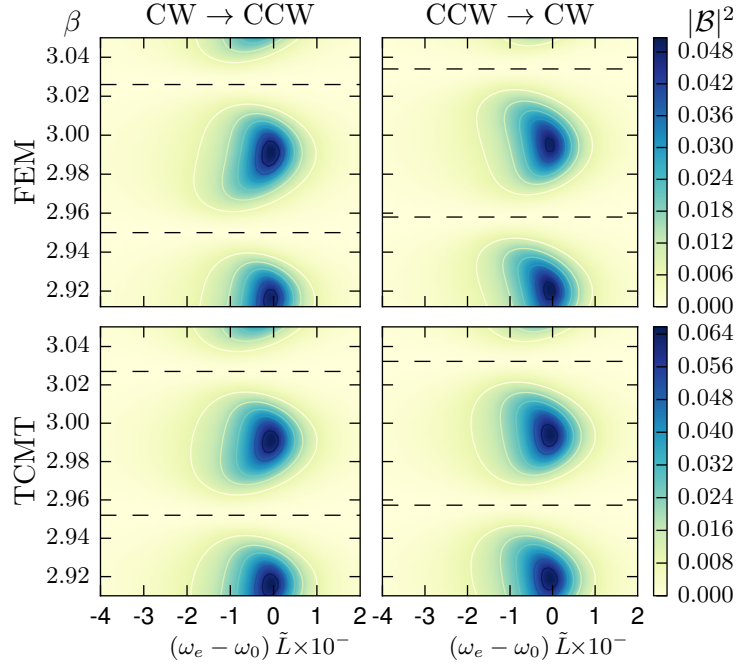


**Figure 7.6:** Asymmetric backscattering intensities  $|\mathcal{B}|^2$  from a CW to a CCW mode (left panels) and from a CCW to a CW mode (right panels). The results have been obtained from a full numerical transmission calculation using a finite element method (upper panels), as well as from the TCMT model (lower panels) and show a good qualitative agreement. In each panel the backscattering intensity is shown in dependence of the injected frequency  $\omega_e$  and the angular position  $\beta$  of the second nanopillar. Here,  $\omega_e$  is given with respect to  $\omega_0 = 79.728\tilde{L}$  at which the asymmetric backscattering intensity peaks. Dashed lines mark the local minima of the backscattering which correspond to the chirality maxima and minima. The asymmetric backscattering is shown by the shifted intensity patterns with respect to the angle  $\beta$ .

## Experimental observations of exceptional points in a laser

In order to verify the theoretical predictions of an EP-induced shutdown and revival of a laser in the experiment, we have worked together with two different experimental groups. In the following chapter we will briefly review these results.

The first group where this effect was experimentally reproduced was the group of Karl Unterrainer at the photonics institute at TU Wien [98]. Their setup consisted of two-coupled microdisk quantum cascade lasers emitting light in the THz spectrum. The second group to demonstrate the presence of an EP in a coupled laser system was the group of Lan Yang at the Washington University. Here, two coupled whispering-gallery-mode resonators were used to demonstrate the effect of an exceptional point in the emission of a Raman laser.

Note, that in addition to these optical systems the effect of loss-induced lasing has been demonstrated in a formally equivalent electrical circuit in the group of Tsampikos Kottos at Wesleyan University [35].

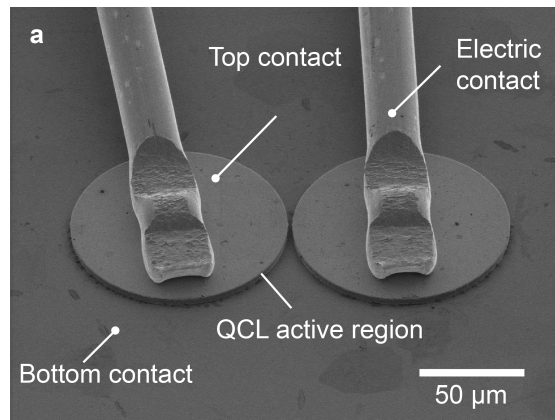


**Figure 8.1:** System of coupled quantum cascade microdisk lasers as used in the experiments at the photonics institute at TU Wien.

## 8.1 EP in coupled THz quantum cascade lasers

Before the experiments at the Institute of Photonics at TU Wien were conducted, we first needed to find an optimal laser configuration for clearly demonstrating the presence of an EP. First of all the coupled laser system needs to lase in the single-mode regime. If this isn't the case, the EP-induced shutdown and revival of the laser emission can be overshadowed by nonlinear mode-competition effects. This can be achieved by using small resonators as well as by operating the laser only closely above threshold. Small resonators help as they thin out the spectrum of modes under the gain curve by increasing the free spectral range. Since the overall gain needs to be small, one needs to be able to apply strong losses to the individual resonators in order to achieve a significant difference of gain in one and loss in the other resonator. This already follows from the simple  $2 \times 2$  matrix of chapter 2.3.

One system which is ideally suited for fulfilling these criteria is a system of coupled microdisk quantum cascade lasers which operates in the THz regime [71,98] and is shown in Fig. 8.1. In each of these microdisks a periodic structure of quantum wells is used to provide the discrete energy levels for the lasing transition [99]. The active material is situated in a wave guide between two metal layers. These metal layers also act as contacts for electrically pumping the

device and they provide rather strong loss due to the finite conductivity of the metal layers. Waveguide simulations have shown that a decrease of the waveguide height together with an absorption layer of Ti on top of the contacts may increase the losses of the system considerably. A disk height of  $3.5\mu\text{m}$  has eventually been found as a good compromise of providing enough loss to suppress multi-mode lasing and enough gain to reach the lasing threshold. Furthermore a given minimal height of the disks is required for reaching a sufficient coupling strength of the resonators.

The active material was designed such that it lases at a frequency of 3.2 THz which corresponds to a wavelength of  $94\mu\text{m}$  such that the wavelength is of comparable size to the diameter of  $96\mu\text{m}$  of the disks. The intercavity distance is  $2\mu\text{m}$ . One advantage for using THz lasers is that due to the large geometric sizes they feature a high tolerance with respect to geometric imperfections in the manufacturing process. This holds especially true in comparison with lasers emitting light in the visible part of the spectrum, where it is thus much harder to fabricate two disks with resonator modes at the same frequencies.

In order to provide theoretical support for the experimental measurements we have performed full vectorial 3D calculations of Maxwell's equations [Eq. (2.5)]. A full SALT calculation was deemed to not be necessary as the lasing frequencies and thresholds for the devices are already sufficiently well given by the quasi-bound states. Furthermore, since the gain curve in the experiment has a FWHM of about 500 GHz and the maximum frequency shift observed in the experiment was about 30 GHz a flat gain curve can be assumed. In the simulations the metal wave guides were modeled as perfect conductors with the outgoing boundary conditions enforced with a PML. Loss and gain were modeled by the imaginary part of the index of refraction. Since we expect the EP to be below the laser threshold it is sufficient to only calculate the QB modes of the system as these already correctly predict the thresholds. The same dimensions were used as in the experiment and the calculations used the open-source finite element framework `ngsolve` [95] which is developed at the Institute for Analysis and Scientific Computing at TU Wien.

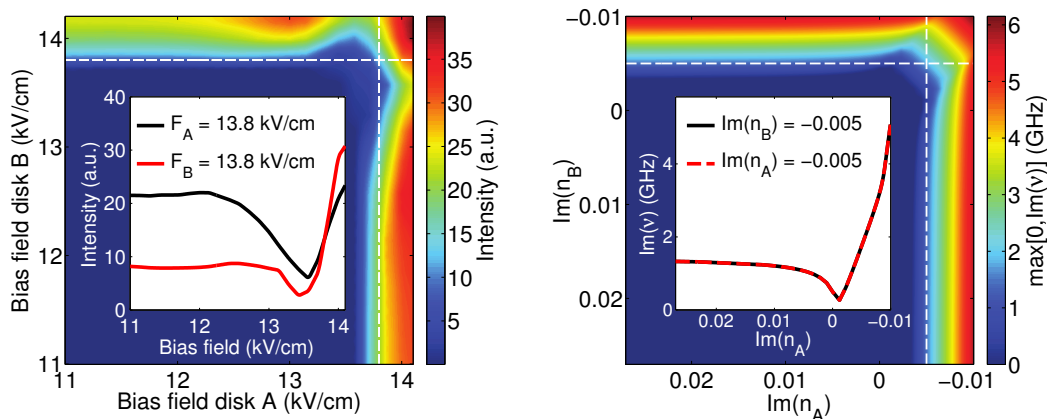


**Figure 8.2:** (left panel) Measured intensity of coupled microdisk quantum cascade lasers as shown in Fig. 8.1 as a function of the bias field applied to each disk. (right panel) The numerical data as calculated from Maxwell’s equations shows the imaginary part of the resonance frequencies  $\nu$ . The data is truncated to only show data for  $\text{Im}(\nu) > 0$  for easier comparison with the experimental data in the left panel. (both panels) To highlight the anomalous pump dependence in the vicinity of the EP, two parameter sweeps marked by the white dashed lines in the original figures are shown in corresponding insets.

Note, that two dimensional calculations show a significant overestimation of the coupling strength such that a direct comparison of the experimental results with such 2D calculations was not possible. This is especially important for identifying the correct lasing modes: For thicker devices that feature multiple modes a comparison of the experimental data with the numerical calculations has shown that the lasing mode are whispering gallery modes with a radial quantization number 3.

The results for the intensity as measured in the QCL setup are compared with the numerical results of the eigenvalue calculations in Fig. 8.2. Here, the bias field, which determines the applied pump strength, of each of the two QCL microdisks were individually scanned in order to expose the EP-induced lasing shutdown, which can be observed in the upper right corner of the individual figures. For a fixed bias field in one disk (as marked by a white dashed line in both panels) scanning the other field revealed the typical decline in intensity

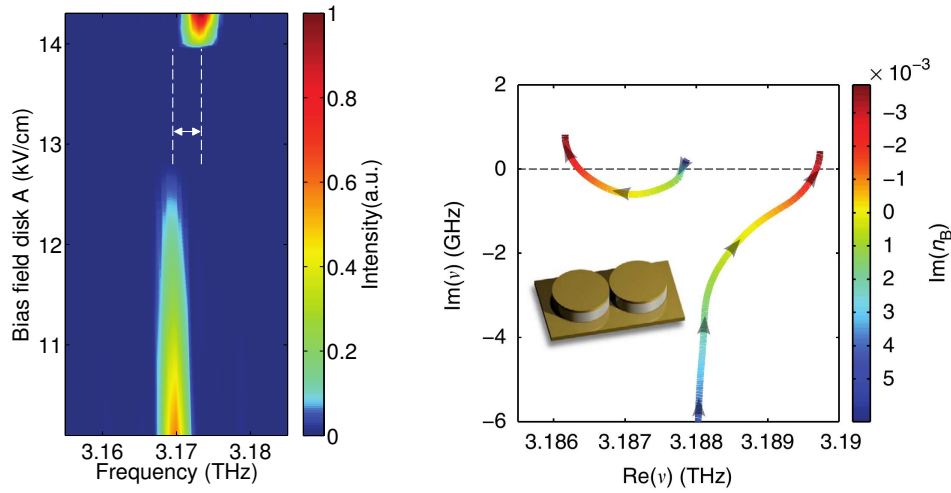


**Figure 8.3:** (Left panel) Experimental spectrum as a function of the bias field of disk A while the bias field of disk B is fixed above threshold. (Right panel) Numerical results: Dependence of the complex eigenfrequency  $\nu$  on the imaginary of the index of refraction in disk B.

with a subsequent revival of lasing (see figure insets). Note, that the patterns from the numerical calculations qualitatively match the behavior of the experimental setup.

In order to further validate that an EP is behind the anomalous lasing behavior observed in Fig. 8.2, a spectrum of the emitted radiation has been recorded and is shown in Fig. 8.3a. In the experiment one observes a pronounced frequency shift of the emitted laser light around the intensity minimum – in accordance with the numerical calculations of Fig. 8.3b. The frequency shift can be attributed to the occurrence of the EP which can already be explained with the simple coupled mode theory model from chapter 2. Whereas below the EP the real frequencies are close to the eigenmode frequencies of a single resonator, above the EP the observed emitted laser frequency corresponds to one of the supermodes. The experiment only revealed a single-mode lasing even for the case when both disks are fully pumped. This is in correspondence with the 2D simulations in chapter 5.4 from which we can conclude that due to strong spatial hole burning only a single mode of the fourfold near-degenerate modes can

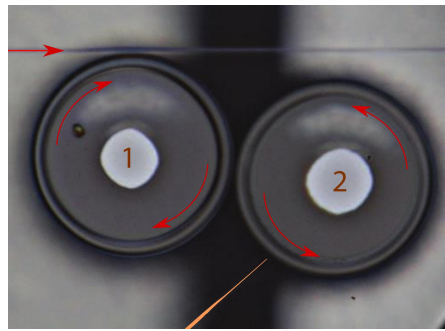


**Figure 8.4:** System of coupled silica whispering-gallery resonators, which are used in the group of Lan Yang at the Washington University in St. Louis. Each of the resonators is coupled to a nano-fiber for probing the system. The loss in resonator 2 can be tuned by bringing a chromium coated silica-nanofiber tip (highlighted in orange) close to the resonator.

lase. This nonlinear effect is, however, not included in the linear numerical 3D calculations shown in Fig. 8.3.

## 8.2 EP in silica whispering-gallery-mode resonators

The second experiment for demonstrating a pump-induced EP in a laser system has been performed at Washington University in St. Louis in the group of Lan Yang [42, 100]. Their experimental setup, which is shown in Fig. 8.4, consists of two coupled silica disk resonators where each of these disks is coupled to a fiber-taper. The disks are Raman lasing such that when light is coupled into the system at a wavelength of 1550nm Raman lasing will be triggered at a frequency of 1650 nm. In contrast to the coupled THz QCL microdisk lasers from the previous experiment, the resonators are much larger than the wavelength. Hence, the modes of the individual resonators will feature different eigenfrequencies due to fabrication imperfections. The modes of the independent resonators are therefore tuned into resonance by manipulating the index of refraction. Since each of the resonators stands on a different substrate, this can be achieved by heating one of the resonators.

In order to steer the system close to an EP two parameters were varied: the



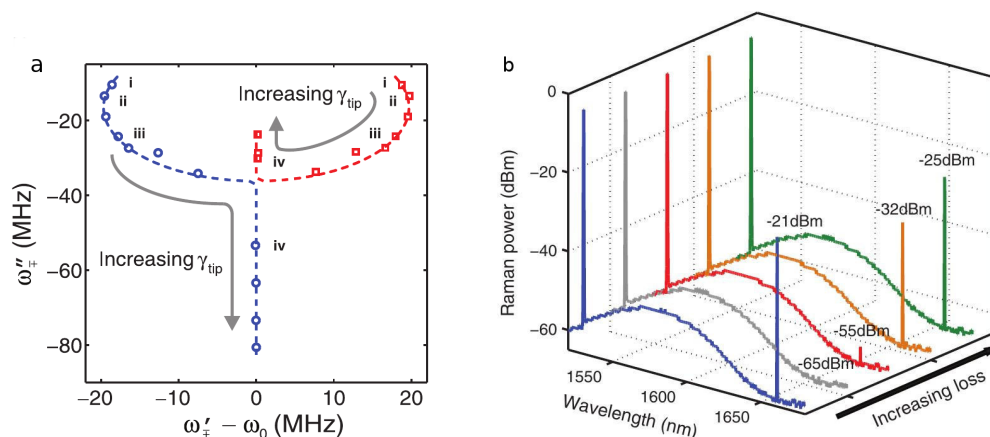


**Figure 8.5:** **a** Measured frequencies and decay rates of two near-degenerate whispering-gallery-modes under variation of the loss induced on resonator 2. **b** Raman lasing spectra of coupled silica microdisks under variation of the applied loss on disk 2 exhibiting the loss-induced shutdown and revival of lasing.

coupling strength  $\kappa$  of the two disks and the loss of the second microdisk. The coupling strength  $\kappa$  was changed by controlling the distance between the two resonators. The loss in the second resonator was manipulated by placing a chromium-coated silica-nanofiber tip, which features strong absorption at the wavelength of the injected light, next to the disk. This additional loss  $\gamma_{\text{tip}}$  was controlled by increasing the overlap between the whispering gallery mode in disk 2 and the nanotip.

The advantage of using this setup in comparison to the THz QCL is that light can be coupled into the resonators via a nearby fiber and therefore enables a direct measurement of the occurrence of the EP by probing the system as we have shown theoretically in section 7.1.2. In particular, the resonance frequencies  $\omega'_{\pm}$  and decay rates  $\omega''_{\pm}$  of a mode pair have been extracted experimentally from the transmission spectra and are shown in Fig. 8.5a. Hence, in this experiment it was managed to connect the below-threshold behavior of the system obtained by measuring the transmission through the waveguides with the above-threshold behavior obtained from measuring the power output of the laser system. The system forms two super-modes in the absence of any

additional loss  $\gamma_{\text{tip}}$  (step i in Fig. 8.5a). By increasing the additional loss  $\gamma_{\text{tip}}$  experienced by disk 2, first the decay rates of both supermodes  $\omega''_{\pm}$  increase while the resonances frequencies  $\omega'_{\pm}$  approach each other. Beyond the EP (step iv in Fig. 8.5a) the super-modes have turned into the single cavity resonator modes with the same frequency  $\omega_0$ , but with two very different decay rates  $\omega'_{\pm}$ . Hence, the typical avoided crossing close to the EP which we have shown, e.g. , for the simple toy model in chapter 2, has been possible to be measured in the experiment.

In Fig. 8.5b several transmission spectra are shown for increasing values of  $\gamma_{\text{tip}}$ . The spectra show both the peaks from the probing light at a wavelength of  $1550\text{nm}$  as well as the Raman laser output signal at  $1650\text{nm}$ . Similar to the THz-QCL measurements an increase of loss at first triggers a shutdown of Raman lasing, but when further increasing the loss Raman lasing is recovered. Note, however, that in the case of Raman lasing the shutdown of the laser is not induced by an EP in the Raman laser mode, but due to the presence of an EP in the pump signal. Here, the intensity of the pump signal within the whispering gallery resonator strongly diminishes in the vicinity of the EP. Since the Raman lasing process is directly proportional to the intensity of the pump signal it therefore shows a similar shutdown effect as discussed in this thesis.

## Conclusion and Outlook

In this thesis we showed that the presence of EPs has a significant effect on the emission characteristics of a laser. In particular, we demonstrated that by steering a laser close to an EP below the laser threshold very unconventional lasing effects occur. For the case of coupled cavities, each of which can be individually pumped, we observed a counter-intuitive reversal of the output power such that an enhanced laser emission can be observed while the overall loss in the system is increased. We have provided a clear recipe for how to observe such loss-induced lasing in the experiment, which is relatively straightforward to implement with present laser technology. Since the publication of our theoretical predictions, two such realizations have been put forward in both of which we were actively involved.

For the numerical calculations we have used the steady-state ab-initio laser theory (SALT) to model the lasing behavior close to the EP. For this we have developed a new and efficient solver for SALT, which does not require expanding the resulting laser modes in a constant flux basis, as has been done previously. Furthermore, our calculations necessitated the development of an extension of the SALT algorithm such that it can also be used to treat resonators featuring near-degenerate modes. For such resonators we showed that above the laser threshold these near-degenerate modes lock into a single mode via the nonlin-

ear spatial hole-burning interaction. In order to prove the stability of this mode we introduced a linear stability analysis of SALT since the original criterion for validating a SALT solution was found to be too strict in this case.

We furthermore investigated the case of an EP *above* the laser threshold where the overall pump of the system was strong enough to avoid a termination of the laser. We showed that for a typical semiconductor material the laser becomes unstable in the vicinity of the EP. However, for systems where the relaxation rate of the inversion is not much smaller than the relaxation rate of the polarization we found the possibility of observing a stable laser output with a strong increase of the laser linewidth. It is still an open question if such a configuration is realizable experimentally.

The topic of exceptional points above the laser threshold where the nonlinearity of the laser equations can no longer be disregarded is certainly a topic of interest for future studies: Adiabatically encircling an exceptional point of a non-Hermitian but linear system is problematic as the adiabatic theorem is not valid for these systems [31]. However, there might be a possibility to realize such a protocol in a laser where the EP itself is influenced by the modes' nonlinear self-interactions. As long as the system can be shown to be stable at each point along the path around the EP an adiabatic passage is feasible and bistable lasing could be observed.

Achieving such a bistable laser system with the help of an EP will require a careful engineering of both geometry and pump parameters of the system. One further system where one can expect to naturally find nonlinearly induced EPs, but which would be much harder to control, is a random laser. Here, many modes typically feature a very similar laser threshold [101], but the modes can experience strong shifts in their frequencies while increasing the pump applied to the laser due to their strong nonlinear modal interactions. If these shifts reliably result in two modes approaching each other in an EP remains an open question.

# Bibliography

- [1] H Haken. *Laser Light Dynamics, Volume II*. North Holland, December 1986.
- [2] W. D. Heiss. The physics of exceptional points. *Journal of Physics A: Mathematical and Theoretical*, 45(44):444016, November 2012.
- [3] Hui Cao and Jan Wiersig. Dielectric microcavities: Model systems for wave chaos and non-Hermitian physics. *Reviews of Modern Physics*, 87(1):61–111, January 2015.
- [4] Bo Zhen, Chia Wei Hsu, Yuichi Igarashi, Ling Lu, Ido Kaminer, Adi Pick, Song-Liang Chua, John D. Joannopoulos, and Marin Soljačić. Spawning rings of exceptional points out of Dirac cones. *arXiv:1504.00734 [physics]*, April 2015. arXiv: 1504.00734.
- [5] R. El-Ganainy, M. Khajavikhan, and Li Ge. Exceptional points and lasing self-termination in photonic molecules. *Physical Review A*, 90(1):013802, July 2014.
- [6] Henning Schomerus and Jan Wiersig. Non-Hermitian-transport effects in coupled-resonator optical waveguides. *Physical Review A*, 90(5):053819, November 2014.
- [7] Jan Wiersig. Chiral and nonorthogonal eigenstate pairs in open quantum systems with weak backscattering between counterpropagating traveling waves. *Physical Review A*, 89(1):012119, January 2014.

- [8] Liang Feng, Xuefeng Zhu, Sui Yang, Hanyu Zhu, Peng Zhang, Xiaobo Yin, Yuan Wang, and Xiang Zhang. Demonstration of a large-scale optical exceptional point structure. *Optics Express*, 22(2):1760–1767, January 2014.
- [9] Jan Wiersig. Enhancing the Sensitivity of Frequency and Energy Splitting Detection by Using Exceptional Points: Application to Microcavity Sensors for Single-Particle Detection. *Physical Review Letters*, 112(20):203901, May 2014.
- [10] Jan Wiersig. Structure of whispering-gallery modes in optical microdisks perturbed by nanoparticles. *Physical Review A*, 84(6):063828, December 2011.
- [11] Sang-Bum Lee, Juhee Yang, Songky Moon, Soo-Young Lee, Jeong-Bo Shim, Sang Wook Kim, Jai-Hyung Lee, and Kyungwon An. Observation of an Exceptional Point in a Chaotic Optical Microcavity. *Physical Review Letters*, 103(13):134101, September 2009.
- [12] Jan Wiersig, Sang Wook Kim, and Martina Hentschel. Asymmetric scattering and nonorthogonal mode patterns in optical microspirals. *Physical Review A*, 78(5):053809, November 2008.
- [13] M. V. Berry and M. R. Dennis. The Optical Singularities of Birefringent Dichroic Chiral Crystals. *Proceedings of the Royal Society of London. Series A: Mathematical, Physical and Engineering Sciences*, 459(2033):1261–1292, May 2003.
- [14] M. V. Berry. Mode degeneracies and the petermann excess-noise factor for unstable lasers. *Journal of Modern Optics*, 50(1):63–81, 2003.
- [15] Carl M. Bender and Stefan Boettcher. Real Spectra in Non-Hermitian Hamiltonians Having PT Symmetry. *Phys. Rev. Lett.*, 80(24):5243–5246, June 1998.
- [16] Christian E. Rüter, Konstantinos G. Makris, Ramy El-Ganainy, Demetrios N. Christodoulides, Mordechai Segev, and Detlef Kip. Ob-

- ervation of parity–time symmetry in optics. *Nature Physics*, 6(3):192–195, March 2010.
- [17] Hakan E. Türeci, A. Douglas Stone, Li Ge, Stefan Rotter, and Robert J. Tandy. Ab initio self-consistent laser theory and random lasers. *Non-linearity*, 22(1):C1–C18, January 2009.
- [18] Hakan E. Türeci, A. Douglas Stone, and B. Collier. Self-consistent multi-mode lasing theory for complex or random lasing media. *Physical Review A*, 74(4):043822, October 2006.
- [19] Li Ge, Y. D. Chong, and A. Douglas Stone. Steady-state ab initio laser theory: Generalizations and analytic results. *Physical Review A*, 82(6):063824, December 2010.
- [20] W. D. Heiss. Exceptional points of non-Hermitian operators. *Journal of Physics A: Mathematical and General*, 37(6):2455, February 2004.
- [21] Nimrod Moiseyev. *Non-Hermitian Quantum Mechanics*. Cambridge University Press, February 2011.
- [22] Tosio Kato. *Perturbation Theory for Linear Operators*. Springer Classics in Mathematics. Springer, 2008.
- [23] Gene H. Golub and Charles F. Van Loan. *Matrix Computations*. JHU Press, December 2012.
- [24] Lloyd N. Trefethen and David Bau III. *Numerical Linear Algebra*. SIAM, June 1997.
- [25] W. D. Heiss. Chirality of wavefunctions for three coalescing levels. *Journal of Physics A: Mathematical and Theoretical*, 41(24):244010, June 2008.
- [26] C. Dembowski, B. Dietz, H.-D. Gräf, H. L. Harney, A. Heine, W. D. Heiss, and A. Richter. Encircling an exceptional point. *Physical Review E*, 69(5):056216, May 2004.

- [27] C. Dembowski, H.-D. Gräf, H. L. Harney, A. Heine, W. D. Heiss, H. Rehfeld, and A. Richter. Experimental Observation of the Topological Structure of Exceptional Points. *Physical Review Letters*, 86(5):787–790, January 2001.
- [28] Raam Uzdin, Alexei Mailybaev, and Nimrod Moiseyev. On the observability and asymmetry of adiabatic state flips generated by exceptional points. *Journal of Physics A: Mathematical and Theoretical*, 44(43):435302, October 2011.
- [29] M V Berry and R Uzdin. Slow non-Hermitian cycling: exact solutions and the Stokes phenomenon. *Journal of Physics A: Mathematical and Theoretical*, 44(43):435303, October 2011.
- [30] Ido Gilary, Alexei A. Mailybaev, and Nimrod Moiseyev. Time-asymmetric quantum-state-exchange mechanism. *Physical Review A*, 88(1):010102, July 2013.
- [31] Thomas J. Milburn, Jörg Doppler, Catherine A. Holmes, Stefano Portolan, Stefan Rotter, and Peter Rabl. General description of quasi-adiabatic dynamical phenomena near exceptional points. *arXiv:1410.1882 [cond-mat, physics:physics, physics:quant-ph]*, October 2014. arXiv: 1410.1882.
- [32] M. Philipp, P. von Brentano, G. Pascovici, and A. Richter. Frequency and width crossing of two interacting resonances in a microwave cavity. *Physical Review E*, 62(2):1922–1926, August 2000.
- [33] B. Dietz, H. L. Harney, O. N. Kirillov, M. Miski-Oglu, A. Richter, and F. Schäfer. Exceptional Points in a Microwave Billiard with Time-Reversal Invariance Violation. *Physical Review Letters*, 106(15):150403, April 2011.
- [34] T. Stehmann, W. D. Heiss, and F. G. Scholtz. Observation of exceptional points in electronic circuits. *Journal of Physics A: Mathematical and General*, 37(31):7813, August 2004.



- [35] M. Chitsazi, S. Factor, J. Schindler, H. Ramezani, F. M. Ellis, and T. Kottos. Experimental observation of lasing shutdown via asymmetric gain. *Physical Review A*, 89(4):043842, April 2014.
- [36] Joseph Schindler, Ang Li, Mei C. Zheng, F. M. Ellis, and Tsampikos Kottos. Experimental study of active LRC circuits with PT symmetries. *Physical Review A*, 84(4):040101, October 2011.
- [37] Youngwoon Choi, Sungsam Kang, Sooin Lim, Wookrae Kim, Jung-Ryul Kim, Jai-Hyung Lee, and Kyungwon An. Quasieigenstate Coalescence in an Atom-Cavity Quantum Composite. *Physical Review Letters*, 104(15):153601, April 2010.
- [38] Carl M. Bender, Bjorn K. Berntson, David Parker, and E. Samuel. Observation of PT phase transition in a simple mechanical system. *American Journal of Physics*, 81(3):173–179, March 2013.
- [39] R. El-Ganainy, K. G. Makris, D. N. Christodoulides, and Ziad H. Musslimani. Theory of coupled optical PT-symmetric structures. *Optics Letters*, 32(17):2632–2634, September 2007.
- [40] Stefano Longhi. PT-symmetric laser absorber. *Physical Review A*, 82(3):031801, September 2010.
- [41] Y. D. Chong, Li Ge, and A. Douglas Stone. PT-Symmetry Breaking and Laser-Absorber Modes in Optical Scattering Systems. *Physical Review Letters*, 106(9):093902, March 2011.
- [42] Bo Peng, Şahin Kaya Özdemir, Fuchuan Lei, Faraz Monifi, Mariagiovanna Gianfreda, Gui Lu Long, Shanhui Fan, Franco Nori, Carl M. Bender, and Lan Yang. Parity-time-symmetric whispering-gallery microcavities. *Nature Physics*, advance online publication, April 2014.
- [43] Long Chang, Xiaoshun Jiang, Shiyue Hua, Chao Yang, Jianming Wen, Liang Jiang, Guanyu Li, Guanzhong Wang, and Min Xiao. Parity-time

- symmetry and variable optical isolation in active-passive-coupled microresonators. *Nature Photonics*, 8(7):524–529, July 2014.
- [44] Liang Feng, Zi Jing Wong, Ren-Min Ma, Yuan Wang, and Xiang Zhang. Single-mode laser by parity-time symmetry breaking. *Science*, 346(6212):972–975, November 2014.
- [45] Hossein Hodaei, Mohammad-Ali Miri, Matthias Heinrich, Demetrios N. Christodoulides, and Mercedeh Khajavikhan. Parity-time–symmetric microring lasers. *Science*, 346(6212):975–978, November 2014.
- [46] A. Guo, G. J. Salamo, D. Duchesne, R. Morandotti, M. Volatier-Ravat, V. Aimez, G. A. Siviloglou, and D. N. Christodoulides. Observation of PT-Symmetry Breaking in Complex Optical Potentials. *Physical Review Letters*, 103(9):093902, August 2009.
- [47] H. Kogelnik and C. V. Shank. Coupled-Wave Theory of Distributed Feedback Lasers. *Journal of Applied Physics*, 43(5):2327–2335, May 1972.
- [48] Stefano Longhi and Giuseppe Della Valle. Loss-induced lasing: new findings in laser theory? *arXiv:1505.03028 [physics, physics:quant-ph]*, May 2015. arXiv: 1505.03028.
- [49] George W. Hanson and Alexander B. Yakovlev. *Operator Theory for Electromagnetics: An Introduction*. Springer Science & Business Media, March 2013.
- [50] Brian McNeil. Due credit for Maxwell-Bloch equations. *Nature Photonics*, 9(4):207–207, April 2015.
- [51] F. Arecchi and R. Bonifacio. Theory of optical maser amplifiers. *IEEE Journal of Quantum Electronics*, 1(4):169–178, July 1965.
- [52] Alexander Cerjan, Adi Pick, Yidong Chong, Steven G. Johnson, and A. Douglas Stone. Quantitative test of general theories of the intrinsic laser linewidth. *arXiv:1505.01884 [physics]*, May 2015. arXiv: 1505.01884.

- [53] Li Ge, Robert J. Tandy, A. D. Stone, and Hakan E. Türeci. Quantitative verification of ab initio self-consistent laser theory. *Optics Express*, 16(21):16895–16902, October 2008.
- [54] S. Esterhazy, D. Liu, M. Liertzer, A. Cerjan, L. Ge, K. G. Makris, A. D. Stone, J. M. Melenk, S. G. Johnson, and S. Rotter. Scalable numerical approach for the steady-state ab initio laser theory. *Physical Review A*, 90(2):023816, August 2014.
- [55] John David Jackson. *Classical Electrodynamics*. Wiley, January 2007.
- [56] Li Ge. *Steady-state Ab Initio Laser Theory and its Applications in Random and Complex Media*. PhD, Yale University, 2010.
- [57] William H. Press. *Numerical Recipes: The Art of Scientific Computing*. Cambridge University Press, 3rd edition edition, September 2007.
- [58] P. L. Kapur and R. Peierls. The Dispersion Formula for Nuclear Reactions. *Proceedings of the Royal Society of London A: Mathematical, Physical and Engineering Sciences*, 166(925):277–295, May 1938.
- [59] Jean-Pierre Berenger. A perfectly matched layer for the absorption of electromagnetic waves. *Journal of Computational Physics*, 114(2):185–200, October 1994.
- [60] Wonseok Shin and Shanhui Fan. Choice of the perfectly matched layer boundary condition for frequency-domain Maxwell’s equations solvers. *Journal of Computational Physics*, 231(8):3406–3431, April 2012.
- [61] A. Logg, K.-A. Mardal, and G.N. Wells, editors. *Automated Solution of Differential Equations by the Finite Element Method*, volume 84 of *Lecture Notes in Computational Science and Engineering*. Springer, Berlin Heidelberg, 2012.
- [62] Sofi Esterhazy. *High-order finite element analysis of the Helmholtz equation and its application in laser physics*. Dissertation, Vienna University of Technology, Wien, September 2013.

- [63] Satish Balay, William D. Gropp, Lois Curfman McInnes, and Barry F. Smith. Efficient Management of Parallelism in Object Oriented Numerical Software Libraries. In *Modern Software Tools in Scientific Computing*, pages 163–202. Birkhäuser Press, 1997.
- [64] Axel Ruhe. Algorithms for the Nonlinear Eigenvalue Problem. *SIAM Journal on Numerical Analysis*, 10(4):674–689, September 1973.
- [65] P. Guillaume. Nonlinear Eigenproblems. *SIAM Journal on Matrix Analysis and Applications*, 20(3):575–595, January 1999.
- [66] Wolf-Jürgen Beyn. An integral method for solving nonlinear eigenvalue problems. *Linear Algebra and its Applications*, 436(10):3839–3863, May 2012.
- [67] Junko Asakura, Tetsuya Sakurai, Hiroto Tadano, Tsutomu Ikegami, and Kinji Kimura. A numerical method for polynomial eigenvalue problems using contour integral. *Japan Journal of Industrial and Applied Mathematics*, 27(1):73–90, May 2010.
- [68] G. Peters and J. Wilkinson. Inverse Iteration, Ill-Conditioned Equations and Newton’s Method. *SIAM Review*, 21(3):339–360, July 1979.
- [69] M. Liertzer, Li Ge, A. Cerjan, A. D. Stone, H. E. Türeci, and S. Rotter. Pump-Induced Exceptional Points in Lasers. *Physical Review Letters*, 108(17):173901, April 2012.
- [70] Alexander Cerjan, Yidong Chong, Li Ge, and A. Douglas Stone. Steady-state ab initio laser theory for N-level lasers. *Optics Express*, 20(1):474–488, January 2012.
- [71] G. Fasching, Ch. Deutsch, A. Benz, A. M. Andrews, P. Klang, R. Zobl, W. Schrenk, G. Strasser, P. Ragulis, V. Tamošiūnas, and K. Unterrainer. Electrically controllable photonic molecule laser. *Optics Express*, 17(22):20321–20326, October 2009.

- [72] G. Fasching, V. Tamosiunas, A. Benz, A.M. Andrews, K. Unterrainer, R. Zobl, Tomas Roch, W. Schrenk, and G. Strasser. Subwavelength Microdisk and Microring Terahertz Quantum-Cascade Lasers. *IEEE Journal of Quantum Electronics*, 43(8):687–697, 2007.
- [73] Kerry J. Vahala. Optical microcavities. *Nature*, 424(6950):839–846, August 2003.
- [74] Lina He, Şahin Kaya Özdemir, and Lan Yang. Whispering gallery microcavity lasers. *Laser & Photonics Reviews*, 7(1):60–82, 2013.
- [75] Soo-Young Lee, Jung-Wan Ryu, Jeong-Bo Shim, Sang-Bum Lee, Sang Wook Kim, and Kyungwon An. Divergent Petermann factor of interacting resonances in a stadium-shaped microcavity. *Physical Review A*, 78(1):015805, July 2008.
- [76] Stephan Burkhardt, Matthias Liertzer, Dmitry O. Krimer, and Stefan Rotter. Steady-state ab initio laser theory for fully or nearly degenerate cavity modes. *Physical Review A*, 92(1):013847, July 2015.
- [77] Alexander Cerjan and A. Douglas Stone. Steady state Ab-initio Theory of Lasers with Injected Signals. *arXiv:1303.2992*, March 2013.
- [78] Satish Balay, William D. Gropp, Lois Curfman McInnes, and Barry F. Smith. Efficient management of parallelism in object oriented numerical software libraries. In E. Arge, A. M. Bruaset, and H. P. Langtangen, editors, *Modern Software Tools in Scientific Computing*, pages 163–202. Birkhäuser Press, 1997.
- [79] Vicente Hernandez, Jose E. Roman, and Vicente Vidal. SLEPc: A Scalable and Flexible Toolkit for the Solution of Eigenvalue Problems. *ACM Trans. Math. Softw.*, 31(3):351–362, September 2005.
- [80] H. Zeghlache, Paul Mandel, N. B. Abraham, L. M. Hoffer, G. L. Lippi, and T. Mello. Bidirectional ring laser: Stability analysis and time-dependent solutions. *Physical Review A*, 37(2):470–497, January 1988.

- [81] Hakan E. Tureci and A. Douglas Stone. Mode competition and output power in regular and chaotic dielectric cavity lasers. pages 255–270, April 2005.
- [82] Alexander Cerjan and A. Douglas Stone. Steady-state ab initio theory of lasers with injected signals. *Physical Review A*, 90(1):013840, July 2014.
- [83] Takahisa Harayama, Takehiro Fukushima, Satoshi Sunada, and Kensuke S. Ikeda. Asymmetric Stationary Lasing Patterns in 2d Symmetric Microcavities. *Physical Review Letters*, 91(7):073903, August 2003.
- [84] A. E. Siegman. Excess spontaneous emission in non-Hermitian optical systems. II. Laser oscillators. *Physical Review A*, 39(3):1264–1268, February 1989.
- [85] A. L. Schawlow and C. H. Townes. Infrared and Optical Masers. *Physical Review*, 112(6):1940–1949, December 1958.
- [86] Y. D. Chong and A. Douglas Stone. General Linewidth Formula for Steady-State Multimode Lasing in Arbitrary Cavities. *Physical Review Letters*, 109(6):063902, August 2012.
- [87] Jason Cornelius Pillay, Yuki Natsume, A. Douglas Stone, and Y. D. Chong. Generalized sub-Schawlow-Townes laser linewidths via material dispersion. *Physical Review A*, 89(3):033840, March 2014.
- [88] A. Pick, A. Cerjan, D. Liu, A. W. Rodriguez, A. D. Stone, Y. D. Chong, and S. G. Johnson. Ab initio multimode linewidth theory for arbitrary inhomogeneous laser cavities. *Physical Review A*, 91(6):063806, June 2015.
- [89] Adi Pick. Private communication, 2015.
- [90] Hong Fu and H. Haken. Multifrequency operations in a short-cavity standing-wave laser. *Physical Review A*, 43(5):2446–2454, March 1991.
- [91] Hermann Haus. *Waves and fields in optoelectronics*, volume 464. Prentice-Hall Englewood Cliffs, NJ, 1984.

- [92] H. Haus and W.P. Huang. Coupled-mode theory. *Proceedings of the IEEE*, 79(10):1505–1518, October 1991.
- [93] John D. Joannopoulos, Steven G. Johnson, Joshua N. Winn, and Robert D. Meade. *Photonic crystals: molding the flow of light*. Princeton university press, 2011.
- [94] Joachim Schöberl. NETGEN An advancing front 2d/3d-mesh generator based on abstract rules. *Computing and Visualization in Science*, 1(1):41–52, July 1997.
- [95] Joachim Schöberl. NGSolve Finite Element Library, 2015.
- [96] Jan Wiersig, Alexander Eberspächer, Jeong-Bo Shim, Jung-Wan Ryu, Susumu Shinohara, Martina Hentschel, and Henning Schomerus. Nonorthogonal pairs of copropagating optical modes in deformed microdisk cavities. *Physical Review A*, 84(2):023845, August 2011.
- [97] Minkyung Kim, Kyungmook Kwon, Jaeho Shim, Youngho Jung, and Kyoungsik Yu. Partially directional microdisk laser with two Rayleigh scatterers. *Optics Letters*, 39(8):2423–2426, April 2014.
- [98] M. Brandstetter, M. Liertzer, C. Deutsch, P. Klang, J. Schöberl, H. E. Türeci, G. Strasser, K. Unterrainer, and S. Rotter. Reversing the pump dependence of a laser at an exceptional point. *Nature Communications*, 5, June 2014.
- [99] Jerome Faist, Federico Capasso, Deborah L. Sivco, Carlo Sirtori, Albert L. Hutchinson, and Alfred Y. Cho. Quantum Cascade Laser. *Science*, 264(5158):553–556, April 1994.
- [100] B. Peng, Ş K. Özdemir, S. Rotter, H. Yilmaz, M. Liertzer, F. Monifi, C. M. Bender, F. Nori, and L. Yang. Loss-induced suppression and revival of lasing. *Science*, 346(6207):328–332, October 2014.

- [101] Hakan E. Türeci, Li Ge, Stefan Rotter, and A. Douglas Stone. Strong Interactions in Multimode Random Lasers. *Science*, 320(5876):643–646, May 2008.



# Matthias Liertzer

## Curriculum Vitae

Bäuerlegasse 9/37

1200 Vienna

Austria, Europe

+43 664 1121 346

+43 1 58801 13644

✉ [matthias.liertzer@tuwien.ac.at](mailto:matthias.liertzer@tuwien.ac.at)

## Education

- 2011–2015 **Doctoral studies**, *Vienna University of Technology*, PhD.  
Engineering Physics
- 06/2014–08/2014 **Visiting student research collaborator**, *Princeton University*, Princeton, United States.
- 2004–2011 **Master studies**, *Vienna University of Technology*, Master of Science.  
Engineering Physics
- 02/2010–08/2010 **Visiting student**, *ETH Zürich*, Switzerland.  
Scientific stay during the course of writing the master thesis
- 08/2007–06/2008 **Exchange student**, *KTH Stockholm*, Schweden.  
Exchange student
- 09/2003–04/2004 **Military service**.
- 1995–2003 **High School**, *BG/BRG Mödling Keimgasse*.  
Graduation with good success

## Working experience

- 04/2011– **Project assistant**, *Vienna University of Technology*, ITP.
- 10/2008–02/2010 **Teaching assistant**, *Vienna University of Technology*, ITP.  
Tutor for quantum mechanics 1/2
- 03/2007–06/2007 **Teaching assistant**, *Vienna University of Technology*, IAP.
- 05/2004–07/2007 **Freelancer**, *Indis Internetdienstleitungen*, Vienna.  
Network administration, Development of autonomous computer systems
- 02/2002–07/2003 **Freelancer**, *Checkpointmedia AG*, Vienna.  
Network administration, Webdesign, Development of autonomous computer systems
- 08/2001 **Internship**, *Checkpointmedia AG*, Wien.  
Webdesign

## Scholarships

- 2014 Scholarship for short-term scientific studies abroad
- 2010 Scholarship for short-term scientific studies abroad
- 2007/2008 Exchange scholarship of the state Lower Austria
- 2007/2008 ERASMUS scholarship
- 2005 Top-scholarship of the state Lower Austria
- 2006 Achievement scholarship of the Vienna University of Technology

---

## Publications

- 2015 Stephan Burkhardt, Matthias Liertzer, Dmitry O. Krimer, and Stefan Rotter, Steady-state ab initio laser theory for fully or nearly degenerate cavity modes, *Physical Review A*, 92(1):013847.
- 2014 B. Peng, Ş K. Özdemir, S. Rotter, H. Yilmaz, M. Liertzer, F. Monifi, C. M. Bender, F. Nori, and L. Yang, Loss-induced suppression and revival of lasing, *Science*, 346(6207):328–332.
- Dmitry O. Krimer, Matthias Liertzer, Stefan Rotter, and Hakan E. Türeci, Route from spontaneous decay to complex multimode dynamics in cavity QED, *Phys. Rev. A*, 89(3):033820.
- S. Esterhazy, D. Liu, M. Liertzer, A. Cerjan, L. Ge, K. G. Makris, A. D. Stone, J. M. Melenk, S. G. Johnson, and S. Rotter, Scalable numerical approach for the steady-state ab initio laser theory, *Physical Review A*, 90(2):023816.
- M. Brandstetter, M. Liertzer, C. Deutsch, P. Klang, J. Schöberl, H. E. Türeci, G. Strasser, K. Unterrainer, and S. Rotter, Reversing the pump dependence of a laser at an exceptional point, *Nature Communications*, 5.
- 2013 Matthias Liertzer and Stefan Rotter, Domesticating random lasers, *SPIE Newsroom*.
- Thomas Hisch, Matthias Liertzer, Dionyz Pogany, Florian Mintert, and Stefan Rotter, Pump-controlled directional light emission from random lasers, *Phys. Rev. Lett.*, 111(2):023902.
- Luca Argenti, Renate Pazourek, Johannes Feist, Stefan Nagele, Matthias Liertzer, Emil Persson, Joachim Burgdörfer, and Eva Lindroth, Photoionization of helium by attosecond pulses: Extraction of spectra from correlated wave functions, *Phys. Rev. A*, 87(5):053405.
- 2012 M. Liertzer, Li Ge, A. Cerjan, A. D. Stone, H. E. Türeci, and S. Rotter, Pump-induced exceptional points in lasers, *Phys. Rev. Lett.*, 108(17):173901.
- M. Liertzer, J. Feist, S. Nagele, and J. Burgdörfer, Multielectron transitions induced by neutron impact on helium, *Phys. Rev. Lett.*, 109(1):013201.

---

## Invited Talks

1. **New solution strategies for the steady-state ab-initio laser theory and applications to random lasers**  
*M. Liertzer, T. Hisch, S. Esterhazy, F. Mintert, D. Pogany, J. Melenk, S. Rotter*  
MASOMO Workshop, WIAS Berlin, 2013
2. **Introduction to the steady-state ab-initio laser theory and its applications**  
*M. Liertzer, L. Ge, A. Cerjan, A.D. Stone, H.E. Türeci, S. Rotter*  
Seminar Laserdynamik, WIAS Berlin, 11.9.2012

---

## Talks

1. **Exceptional points in lasers**  
*M. Liertzer*  
Seminar talk, June 2015, Princeton University, Princeton, US
2. **Exceptional points in resonant structures with gain and loss**  
*M. Liertzer, P. Ambichl, M. Brandstetter, K. Makris, T. Hisch, L. Ge, Y. Chong, A.D. Stone, H.E. Türeci, C. Deutsch, K. Unterrainer*  
IARD/PT Meeting 2014, Storrs, Connecticut, USA

3. **Solving the steady-state ab-initio laser theory with FEM**  
*S. Esterhazy, M. Liertzer, J. Melenk, S. Rotter*  
Mafelap 2013, Brunel University London, 2013
4. **Pump-induced exceptional points in lasers**  
*M. Liertzer, L. Ge, A. Cerjan, A.D. Stone, H.E. Türeci, S. Rotter*  
Workshop on Nonlinear Dynamics in Semiconductor lasers, Berlin, 2012
5. **Pump-induced exceptional points in lasers**  
*M. Liertzer, L. Ge, A. Cerjan, A.D. Stone, H.E. Türeci, S. Rotter*  
International Quantum Cascade Lasers School and Workshop Baden, 2012
6. **Pump-controlled directional emission from a random laser**  
*T. Hirsch, M. Liertzer, F. Mintert, S. Rotter*  
8th International Workshop on Disordered Systems, Benasque, Spain, 2012
7. **Pump-induced Exceptional Points in Lasers**  
*M. Liertzer, L. Ge, A. Cerjan, A.D. Stone, H.E. Türeci, S. Rotter*  
MIRTHE-IRON-SensorCAT Virtual Conference, 2012
8. **Scattering and lasing in coupled systems with gain and loss**  
*M. Liertzer, K. Makris, P. Ambichl, S. Rotter, L. Ge, H.E. Türeci*  
Analytic and algebraic methods in physics IX, Prague, 2011
9. **Exceptional points above lasing threshold**  
*M. Liertzer, L. Ge, K. Makris, H.E. Türeci, S. Rotter*  
X. Billiard Workshop, Riezlern, 2011
10. **Nonlinear interactions in coupled microlasers**  
*M. Liertzer, L. Ge, K. Makris, H.E. Türeci, S. Rotter*  
IR-On meeting, University of Technology Vienna, 7.6.2011
11. **Collective multi-mode effects in quantum optics**  
*B. Skerlak, M. Liertzer, S. Rotter, H.E. Türeci*  
DPG spring meeting, Dresden, 2011